Carnegie Mellon University

CARNEGIE INSTITUTE OF TECHNOLOGY

THESIS

SUBMITTED IN PARTIAL FULFILLMENT OF THE REQUIREMENTS
FOR THE DEGREE OF DOCTOR OF PHILOSOPHY

TITLE

Thermal Conductivity of Cryoprotective Agents with Applications to Cryopreservation by Vitrification

PRESENTED BY

Lili E. Ehrlich

ACCEPTED BY THE DEPARTMENT OF MECHANICAL ENGINEERING

ADVISOR, MAJOR PROFESSOR	DATE
ADVISOR, MAJOR PROFESSOR	DATE
DEPARTMENT HEAD	DATE

APPROVED BY THE COLLEGE COUNCIL

DEAN	DATE

Thermal Conductivity of Cryoprotective Agents with Applications to Cryopreservation by Vitrification

Submitted in partial fulfillment of the requirements for

the degree of

Doctor of Philosophy

in

Mechanical Engineering

Lili Ehrlich

B.E., Mechanical Engineering, Cooper Union

M.S., Mechanical Engineering, Carnegie Mellon University

Carnegie Mellon University
Pittsburgh, PA

February, 2017

Acknowledgements

I would like to thank my advisors, Professor Yoed Rabin, and Professor Jonathan Malen, for years of guidance, learning, and collaboration. I would also like to thank my committee members, Professor Michael Taylor and Professor Sheng Shen.

This work has been supported in part by Award Number R21RR026210 from the National Center for Research Resources (NCRR), Award Number R21GM103407 from the National Institute of General Medical Sciences (NIGMS), and Award Number R01HL127618 from the National Heart Lung and Blood Institute. This work has also been funded in part by the Dowd Fellowship from the College of Engineering at Carnegie Mellon University. The authors would like to thank Philip and Marsha Dowd for their financial support and encouragement.

I would like to also thank my colleagues past and present who were helpful and wise: Dr. David Eisenberg, Prem Solanki, Kevin Parrish, Ye Han, Tristan Greiner, Purva Joshi, Dr. Justin Freedman, Dr. WeeLiat Ong, Dr. Scott Schiffres, Dr. Keith Regner, and Dr. Shubhaditya Majumdar. I would especially like to thank Dr. Justin Feig for his exceptional help and encouragement throughout the years.

Finally, I would like to thank my parents and my sister, Paula and Stephen Ehrlich, and Dayna Greenspan, for giving me the opportunities to pursue my education.

Abstract

Cryopreservation is the preservation of biomaterials at extremely low temperatures. It is the only alternative for long-term storage of high quality biomaterials, with applications to biobanking and transplant medicine. Cryopreservation success revolves around the control of ice formation, which is known to be harmful. Ice formation is a path-dependent phenomenon, affected by the thermal history and presence of nucleation promotors. Cryoprotective agents (CPAs) are commonly added to the biomaterial to be preserved, in order to suppress ice formation and inhibit its growth during the cryopreservation protocol. Ice-free cryopreservation can be achieved in large-size systems when the biomaterial is loaded with a high CPA concentration solution and cooled rapidly, in a process that is known as *vitrification* (*vitreous* means *glassy* in Latin). During vitrification, the CPA viscosity increases exponentially with decreasing temperature, while the material is cooled to deep cryogenic temperatures faster than the typical time scale for crystallization. The material can potentially be stored indefinitely at such low temperatures.

Large-size vitrification is associated with three competing needs on the CPA concentration. Since the cooling rate at the center of the specimen decreases with the increasing specimen size due to the scaling conductive resistance, higher CPA concentrations may be required to suppress crystallization in larger specimens. Higher CPA concentration generally requires lower cooling rates to avoid ice crystallization. On the other hand, since CPAs are potentially toxic, the lowest possible CPA concentration is required to maintain viability and facilitate functional recovery. The decrease in CPA concentration combined with an increase in cooling rates may intensify thermo-mechanical stress due to non-uniform thermal contraction to the point of structural destruction. Essentially, successful cryopreservation represents the outcome of an optimization problem on the composition and concentration of the CPA cocktail.

The work presented in this thesis combines an experimental study on the thermal conductivity of relevant materials, and a theoretical study to identify the effects of the measured values on cryopreservation protocols. The unique contributions presented as the initial stage of the experimental study are: (i) the modification of the cryomacroscope and creation of an experimental program to make thermal conductivity measurements of CPA based on the existing transient hot wire technique, (ii) to develop a protocol for making thermal conductivity measurements during rewarming portion of the cryoprotocol, and (iii), to begin generating a data bank of thermal conductivity of CPA and materials used in cryopreservation. Thermal conductivity measurements

are presented for the CPA Dimethyl Sulfoxide (DMSO), over a concentration range of 2M to 10M, in a temperature range of -180°C to 25°C. Samples of 2M to 6M DMSO were found to crystallize at quasi-steady cooling rates, while samples of 7.05 to 10M were found to vitrify. Thermal conductivities of the crystallized and vitrified material reach a tenfold difference at -180°C. The quality of measurements using the presented technique has been verified theoretically by means of finite element analysis (FEA) using the commercial code ANSYS.

This experimental study is expanded to the study of thermal conductivity of the CPA cocktail DP6--a mixture of 3M DMSO and 3M propylene glycol, which has drawn significant attention in the cryobiology community in recent times. The unique contributions are the first thermal conductivity measurements reported in literature of the combined effect of DP6 with synthetic ice modulators (SIMs), including 6% 1,3Cyclohexanediol, 6% 2,3Butanediol, and 12% PEG400. Results of this study demonstrate that the thermal conductivity may vary by three fold between the amorphous and crystalline phases of DP6 below the glass transition temperature. Results of this study further demonstrate the ability of SIMs to decrease the extent of crystallization in DP6, even at subcritical cooling and rewarming rates.

The accompanying theoretical investigation focuses on cryopreservation in a kidney model, in effort to explore how the thermal history is affected by variations in the measured thermal conductivity. This analysis is based on FEA using the commercial code ANSYS. In particular, the unique contributions of this study are: (i) thermal analysis of a vitrifying rabbit kidney based on an established rabbit-kidney cryopreservation protocol, and (ii), exploring scale-up thermal effects to a human-size organ. This represents a 21-fold increase in organ size. Results indicate that even in the case of the human kidney, cooling rates remain high enough in all parts of the kidney to prevent ice formation at temperatures above -100^{o}C.

Table of Contents

Acknowledgements i

Abstract ii

Table of Contents iv

List of Figures vii

List of Tables xii

List of Acronyms xiv

Chapter 1 Introduction

1.1 The Unmet Need for Organ Preservation and Banking 1

1.2 Cryopreservation 2

1.3 Thermal Conductivity of Vitrified CPA 3

1.4 Synthetic Ice Modulators 5

1.5 Effect of Thermal Conductivity on Cooling Rates Predicted in Computational Cryopreservation 6

Chapter 2 Large Thermal Conductivity Differences between the Crystalline and Vitrified States of DMSO with Applications to Cryopreservation

2.1 Objective 7

2.2 Experimental Setup 7

2.3 Materials and Methods 10

2.4 Results and Discussion 17

2.4.1 Reference Experiments 19

2.4.2 DMSO Experiments 21

2.4.3 Uncertainty Analysis 23

2.4.4 Crystallized DMSO 24

2.4.5 Vitrified DMSO 29

2.5 Conclusions 31

Chapter 3 Thermal Conductivity of the Cryoprotective Cocktail DP6 in Cryogenic Temperatures, in the Presence and Absence of Synthetic Ice Modulators

3.1 Objective 32

3.2 Materials and Methods 32

3.2.1 Thermal Protocol 33

3.2.2 Materials Tested 36

3.3 Results and Discussion 36

3.3.1 Rewarming Phase Crystallization 40

3.3.2 Vehicle Solution Effects on DP6 Vitrification in Absence of SIMs 41

3.3.3 The Effects of SIMs on DP6 Vitrification 42

3.4 Conclusions 44

Chapter 4 Finite Elements Evaluation of Error in Thermal Conductivity Measurements by the Transient Hot Wire Technique due to Non-Uniform Temperature Field in Sample

4.1 Objective 45

4.2 System Limitations 45

4.3 Mathematical Formulation 46

4.3.1 Modification to Hot Wire Geometry for Cryomacroscopy 47

4.3.2 Modification to Hot Wire Measurements Made During Rewarming 48

4.3.3 Heat Transfer Problem 49

4.3.4 FEA Simulation 52

4.4 Results and Discussion 53

4.5 Conclusions 55

Chapter 5 Thermal Analyses of a Human Kidney and a Rabbit Kidney During Cryopreservation by Vitrification

5.1 Objective 57

5.2 Materials and Methods 57

5.2.1 Physical Model 57

5.2.2 Thermal History 60

5.2.3 Heat Transfer Model 62

5.2.4 Thermal Properties 62

5.2.5 Ice Formation Tendency in Dilutions of M22 63

5.2.6 Numerical Solution 64

5.3 Results and Discussion 65

5.4 Conclusions 72

Chapter 6 Conclusions and Future Work

6.1 Conclusions 73

6.2 Future Work 76

6.2.1 Finite Elements Evaluation of Error in Transient Hot-Wire: Probing the Limitations of the Technique 76

6.2.2 Thermal Conductivity of Vitrifying Kidney Tissue in CPA 77

6.2.3 Thermal Analyses of a Human Kidney and a Rabbit Kidney during Cryopreservation with Possibility of Phase Change 77

List of Publications 79

References 81

List of Figures

Figure	Title	Page
1.1	Temperature-Dependent Thermal Conductivity Measurements of Silicon Dioxide in the crystalline state (α-quartz) and *amorphous* state (vitreous silica) reproduced from [8].	4
2.1	Schematic illustration of the scanning cryomacroscope setup and peripheral instrumentation [31]; the modified experimentation stage for thermal conductivity measurements is displayed with more detail in Fig. 2.2	8
2.2	Schematic illustration of (a) the cryomacroscope experimentation stage (the red arrow represents the direction of view; see Fig. 2.5 for example), and (b) the hot wire sensor setup in the cuvette (sample container).	9
2.3	Typical thermal history during thermal conductivity measurements of 7.05M DMSO, where TC1 measures the chamber temperature, TC2 measures the wall inner surface at the center of one of the faces, and TC3 measures the temperature of the outer surface of the wall.	12
2.4	Temperature measurements during thermal conductivity experiments: (a) temperature results of three consecutive thermal experiments, where the change in the bulk sample temperature is best-fitted with a 2^{nd} order polynomial; (b) a higher magnification of an experimental dataset; and (c) a temperature dataset used to calculate the thermal conductivity after the subtraction of the bulk sample rewarming curve, where the slope of the best-fitted curve on a semi-log plot is used to calculate the thermal conductivity (shown as a solid line in figure).	15

2.5 Cryomacroscope images of samples in various states: (a) a vitrified 7.05M DMSO sample at a temperature of -147°C; (b) a 2M DMSO sample undergoing crystallization in the form of dendrites at temperature of -10°C; (c) a partially crystallized 6M DMSO sample at a temperature of -58°C; and (d) a completely crystallized 6M DMSO solution at a temperature of -65°C. 18

2.6 Thermal conductivity measurements of pure water ice and glycerol in the current study, compared with literature data, where the curve by Rabin (2000) [57] represents compilation of earlier literature data. 20

2.7 Thermal conductivity measurements of DMSO and pure water ice. The Cahill-Pohl model for thermal conductivity of amorphous solids is calculated with Eq. (2.8) for 10 M DMSO. Based on cryomacroscope observations, DMSO concentrations of 6M or less underwent crystallization while concentrations of 7.05M and above vitrified. 21

2.8 Solid fraction during solidification of a water-DMSO mixture, extracted from a phase diagram [61]. 26

2.9 Thermal conductivity as a function of solid fraction for DMSO at various concentrations, where the Bruggeman model is calculated with Eq. (2.7) for 6M DMSO. 28

3.1 Schematic illustration of the transient hot-wire sensor setup; the dashed line represents the direction of visualization by the scanning cryomacroscope [14]. 33

3.2 Representative thermal histories during thermal conductivity measurements of DP6 mixed with PEG400, where temperature data were measured at the center 34

of the cuvette inner wall surface. For all experiments the following rates were kept constant: H_2 = -2 °C/min, H_3 = 1.7 °C/min (average passive rewarming), and H_4 = 3 °C/min.

3.3 Measured thermal conductivity of DP6 in the presence and absence of SIMs and EC; 6 M DMSO is also shown for reference [14]. At the applicable cooling rate, the glass transition temperature for 6 M DMSO is -132 °C, and -119 °C for DP6 [2,40]. The eutectic temperature for DMSO is -63 °C at a concentration of 6 M [61]. 37

3.4 Thermal conductivity measurements of DP6 in the presence of SIMs, where the glass transition temperature of DP6 is -119 °C at the applicable cooling rates [60]. 38

3.5 Average difference in thermal conductivity measurements between a cooling rate of 5 °C/min and 50 °C/min at -121 °C, two degrees below the glass transition temperature of -119 °C [60]. 42

4.1 Schematic illustration of: (a) the CPA, cuvette, and cuvette cap, shown with cutting plane used to simplify finite elements analysis and description of section views, (b) its finite elements (ANSYS) representation; (c) front view of the cuvette cap, the mounted hot wire probe and the path mapped from ❶ to ❷ for the below analysis; (d) the heat transfer processes within the model, where T_∞ is the free stream temperature in the cooling chamber recorded during experiments and is imposed as the free stream temperature in the model, $\dot{q}(t)$ is the time-dependent volumetric heat generation in the wire, and U is the convection coefficient from the outer surfaces of the cuvette and cuvette cap to the surroundings 48

4.2 Temperature versus time during master simulation (top) and during heating cycle simulations A, C, E (shown left to right). Heating cycles investigated are labeled A, B, C, D, E, F and are further discussed in text. Temperatures of interest include the temperature range of the CPA domain, hot wire maximum, minimum, and average. Also shown are τ (period of time between heating end time, t_{end} and heating start time, t_0) and temperature change of the wire over τ, ΔT_τ 50

4.3 Plots of heating cycle E: a) temperature along wire length from ❶ to ❷, where temperature and average temperature are shown at the start of heating ($t=t_0$) and at the end of heating ($t=t_{end}$), and b) change in temperature during heating along wire length from ❶ to ❷, where ΔT_τ is T_{wire}, $t=t_{end}$ minus T_{wire}, $t=t_0$, and standard deviation of ΔT_τ is 0.03°C 54

5.1 Illustrations of system analyzed in this study: (a) a kidney in a cylindrical container filled with CPA; (b) schematic view of the four subdomains of the system, each characterized by unique thermal properties; heat transfer processes and material properties of the constituents; (c) a cross section of the system showing the FEA mesh and virtual thermal sensors. 58

5.2 Thermal history in the kidney model for (a) a vitrified system with CPA properties, (b) the same system at the early stage of cooling, and (c) a vitrified system but with ice properties; where S_o is the outer surface of the cortex, S_i is the medulla-cortex interface, T_c is the temperature of the cooling chamber, and T_0 is the temperature at the center of the kidney (Fig. 5.1c). 61

5.3 Cooling rate history in the vitrified kidney model, where S_o is the outer surface of the cortex S_i is the medulla-cortex interface (Fig. 1c), and CCR_{med} is the critical cooling rate for 87% M22 in the medulla (1 ºC/min). 67

5.4 Thermal history of Sensor 9 (the closest point in the medulla to center of system) for the cases of a vitrified human kidney and a vitrified rabbit kidney. The colored areas refer to the human kidney simulation, where green corresponds to the time range in which the sensor indicates temperatures below T_m and the cooling rate is above the CCR of 87% M22, while red corresponds to the time range in which the sensor indicates temperatures above T_g and the cooling rate is below CCR of 87% M22; colored areas interface at -103ºC. 69

5.5 Temperature fields when the Sensor 9 indicates (a) -30°C, (b) -60°C, (c) -90°C, and (d) -120°C. 71

List of Tables

Table	Title	Page
2.1	Best-fit polynomial approximation data for the thermal conductivity curves displayed in Fig. 2.7.	22
2.2	Typical data used to estimate the overall uncertainty in a thermal conductivity measurement, based on the hot wire measurement technique and a sample of 7.05M DMSO.	24
2.3	The temperature of melting completion based on experimental results, T_m, observed during thermal conductivity measurements in comparison with the liquidus temperature, T_l, from a water-DMSO phase diagram [61].	27
2.4	The liquidus temperature, T_l, and the solidus temperature, T_s, of solution concentrations observed to vitrify in this study, from a water-DMSO phase diagram [61].	29
3.1	Summary of thermal history parameters used in Chapter 3, where all protocols included H_2= -2°C/min and H_3= 3°C/min as illustrated in Fig. 3.2.	35
3.2	Best-fit polynomial approximation for thermal conductivity curves displayed in Figs 3.3 and 3.5; average values are given in cases where (i) the span of the polynomial approximation of thermal conductivity is smaller than two standard deviations of the experimental data over the relevant temperature range (denoted by †), or (ii), where extensive RPC effects over a given data set are observed (denoted by ‡).	39

4.1 Material properties used for ANSYS thermal transient analysis in Chapter 4 (temperature is in °C) 51

5.1 Material properties used in Chapter 5, where temperature-dependent properties are presented in °C within the range of -22°C to -135°C 59

List of Abbreviations

ABS Acrylonitrile butadiene styrene: A plastic material used in 3-D printing of certain cryomacroscope and transient hot wire components.

BD: Butanediol- A chemical where an isomer is used as a SIM.

CHD: Cyclohexanediol- A chemical where an isomer is used as a SIM.

CPA: Cryoprotective agent- a solvent used to control or suppress ice formation during cryopreservation

DMSO: Dimethyl sulfoxide- A chemical used in aqueous solutions as a CPA, or combined in cocktails with other CPAs.

DP6: A CPA cocktail composed of 234.4 g/L DMSO (3 M), 228.3 g/L propylene glycol (3 M), and 2.4 g/L HEPES.

DSC: Differential scanning calorimetry- An experimental technique where the amount of heat required to change the temperature of a substance is measured as a function of temperature.

EC: Euro Collins- A vehicle solution used in CPAs which maintains ionic and hydraulic balance in cells at cold temperatures.

FEA: Finite Element Analysis- a computational technique for solving complex boundary value problems for partial differential equations.

PEG: Polyethylene glycol- A chemical where an isomer is used as a SIM.

RPC: an inclusive term combining crystal growth from nuclei already developed during cooling (also known as recrystallization) and crystal formation during rewarming (also known as devitrification)

SIM: Synthetic ice modulator- A chemical additive to CPA cocktails to inhibit the growth of ice nuclei.

THW: Transient Hot Wire- a technique used to measure thermal conductivity, where a revolves around use of a submerged electrical resistor which, after step-like activation

in current, generates Joule heating while simultaneously measuring its own thermal response. The thermal conductivity of the enveloping medium is extracted from the slope of the measured thermal response of the wire with respect to the natural log of time.

TC: Thermocouple- Temperature sensor

Chapter 1

Introduction

1.1 The Unmet Need for Organ Preservation and Banking

Currently, more than 18,000 kidneys are transplanted every year in the United States, 20,000 in the European Union, and nearly 80,000 worldwide [13], but the World Health Organization estimates that in general organ transplants are meeting less than 10% of the actual need [49]. To date, only hypothermic storage (i.e., short-term storage at above-freezing temperatures) is used to extend the shelf life of a kidney to a maximum of 24-48 hours depending on the quality of the donated kidney. This storage technique extends the life of many other organs by only 3-12 hours. Moreover, the transportation time required to move the organ from donor to recipient has been shown to be a significant limitation in organ transplantation [73]. An estimated one-fifth of donated kidneys are discarded, many of which when recipients cannot be found in this short time window [64]. Moving from hypothermic storage to cryopreservation by vitrification represents a quantum leap in organ preservation technology, potentially extending shelf life indefinitely. The advantages of extended tissue storage are quite dramatic as it can: (i) facilitate better donor-recipient matching, which is currently quite limited, (ii) allow time for organ reconditioning, (iii) create the appropriate conditions for biobanking of engineered tissue constructs, and (iv) facilitate more favorable and less urgent conditions for transplantation surgeries.

In the case of donor-recipient matching, in current techniques, the hematopoietic cells from bone marrow are transplanted from the donor to recipient in advance of the kidney transplant in order to induce immune tolerance. Successful implementation of this practice would drastically impact success of organ transplantation. Currently, without the immune tolerance that would result from such matching, recipients undergo immunosuppressive therapy to prevent organ rejection. Immunosuppression therapy is both costly and complicated, with infection and cancer as major risks [66]. In addition, when the chronic organ shortage is solved by the development of laboratory-derived renal replacements (e.g., tissue-engineered organs) [48], the ability to inventory these constructs will become critical [28]. Note that substantial times (possibly weeks) will be required

to grow engineered organs, which must be transplanted or cryopreserved at the point of mature development, much like an ordinary donated organ.

1.2 Cryopreservation

Cryopreservation is the preservation of biomaterials at low temperatures through suspension of molecular motion. Cryopreservation success revolves around the control of the kinetics of ice crystallization—the cornerstone of cryoinjury. Ice formation is a path-dependent phenomenon, with the thermal history and availability of nucleators as dominating factors. Controlling the formation of ice is achieved by introducing cryoprotective agents (CPAs) into the specimen and controlling its thermal history. *Classical cryopreservation*—the preservation of a specimen using low CPA concentration—essentially aims at limiting ice formation to the extracellular space and has shown successful results with small samples, such as stem cells, sperm, and embryos [51], typically in the range of μm to mm. Unfortunately, the extracellular ice formation inherent to classical cryopreservation techniques cannot be tolerated by organized, complex, multicellular systems, which necessitates alternative means for scaling up cryopreservation to bulky tissues and organs [70,72].

Vitrification is an alternative approach to classical cryopreservation, where the specimen is permeated with a high-concentration CPA cocktail and cooled rapidly in an effort to completely avoid ice crystallization (*vitreous* means *glassy* in Latin). While vitrification in biological systems was initially investigated by Luyet in 1937, it remained largely unexplored until the 1980's [25,72]. Vitrification is based on the temperature dependency of the CPA viscosity, which increases exponentially with decreasing temperature [53]. If the material is cooled fast enough, such that the typical time scale for crystallization is longer than the typical time scale for cooling, the viscosity gets to such extremely high values that the material is trapped in an amorphous state and behaves as a solid for all practical purposes. The temperature threshold below which the vitrified material is considered solid is commonly known as the glass transition temperature, T_g. The glass transition temperature may be defined in different ways: calorimetrically, T_g is the temperature corresponding to the heat capacity that falls halfway between the transition from liquid heat capacity to glass heat capacity measured with differential scanning calorimetry (DSC), but can also be defined mechanically as the temperature at which the liquid viscosity exceeds 10^{13} Poise (or 10^{12} Pa-s)[78].

Successful large-size vitrification brings about three competing needs: (i) to increase the CPA concentration in order to compensate for the decreasing cooling rate at the center of a large specimen[1]; (ii) to decrease the CPA concentration in order to minimize its toxicity effects [21,24]; and, (iii) to decrease the cooling rate within the glassy state in order to reduce thermo-mechanical stress, which may lead to structural damage [69]. Note that the cooling rate is only one among several factors that may elevate thermo-mechanical stresses to hazardous levels [69]. The above competing needs outline an optimization problem, combining concepts from cryobiology, thermal design, and solid mechanics [72].

Optimizing the cryopreservation problem requires predictive tools, such as bioheat transfer simulations, to evaluate the likelihood of vitrification, ice nucleation, and crystal growth. The path-dependent process of cryopreservation can only be measured at discrete points, but the thermal history must be evaluated all across the specimen. Computer simulations of vitrification require knowledge on the thermophysical properties of the material, such as thermal conductivity and specific heat, which represents a relatively uncharted area of research [10,14]. These properties may be strongly dependent upon temperature, solution concentration, and the level of molecular order—dependencies that too often are neglected, resulting in gross miscalculations of the temperature field [57]. For example, Choi and Bischof [10] have reviewed key thermal properties measurements and demonstrated how they may affect the outcome of thermal analysis as the process increasingly deviates from equilibrium conditions. Despite the need for specific thermal properties and in the absence of specific data, all too often thermal analyses rely on the properties of pure water (liquid and solid) as substitutes to CPA properties. In particular, the glassy state of CPA is often modeled as pure water ice or isotonic saline [11,38,63], despite their compositional and structural differences.

1.3 Thermal Conductivity of Vitrified CPA

The temperature-dependence of thermal conductivity of biomaterials is a relatively new concern in the field of cryobiology, which has relied on heat transfer predictions and analyses for decades. Newer still to the cryobiology community is the distinction between amorphous and

[1] The cooling rate threshold to ensure vitrification decreases with the increasing concentration, and studies have focused on measuring the critical cooling and rewarming rates (i.e.- minimum rates for completely avoiding crystallization) in various CPAs [44,85].

crystalline states and the manner in which they can affect thermal conductivity of a material. A hitherto overlooked consideration is the appreciable difference in thermal conductivity between an amorphous (i.e., vitrified) material and an ordered crystalline material of the same molecular composition. This difference results from long-range atomic periodicity in crystalline materials that enables efficient energy transport by collective motion of molecules (i.e., phonons) [8]. In contrast, uncorrelated atomic vibrations in amorphous solids transmit energy poorly. For example, the thermal conductivity of crystalline SiO_2 (quartz) differs from amorphous SiO_2 (glass) by one order of magnitude at 25°C and by as much as four orders of magnitude at -263°C [8].

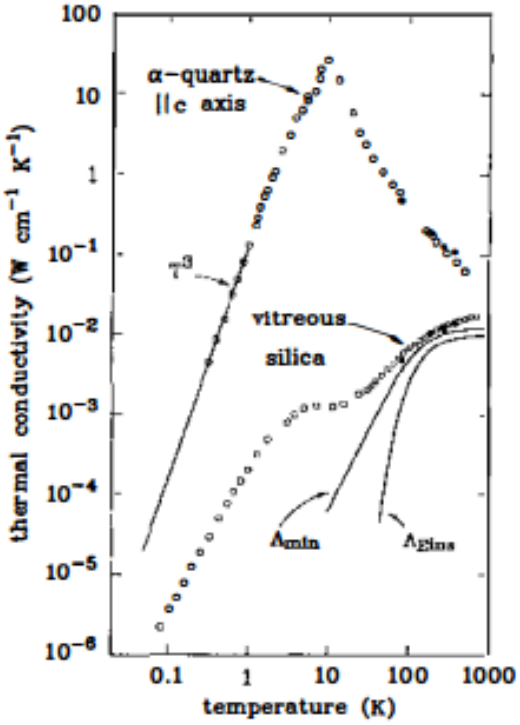

Figure 1.1: Temperature-Dependent Thermal Conductivity Measurements of Silicon Dioxide in the crystalline state (α-quartz) and amorphous state (vitreous silica) reproduced from *[8]*.

Measurements of thermal conductivity of vitrified and crystalline CPAs are described in Chapters 2 and 3. In Chapter 2, Dimethyl-Sulfoxide (DMSO) is chosen as a material of interest as it is a relatively well characterized CPA [1,3,44,50,61,82], which serves as a key ingredient in many CPA cocktails, and may be used as a model solution for CPA cocktails containing the same volumetric concentration of solutes. The thermal conductivity of DMSO has already been the focus of a related study [82] which utilized a transient hot probe (with spherical geometry) for measurements. However, it has been limited to temperatures of -20°C or higher, to high

concentrations of 7 M, 10.55 M, and 14 M (50%, 75%, and 100% by volume, respectively). At these temperatures, differentiation between the crystalline and the vitrified states obviously could not be made[2]. In the presented experimental setup in Chapters 2 and 3, a cryomacroscope [31] is employed as a means to correlate the state of a CPA with thermal history and thermal conductivity measurements. These are the first thermal conductivity measurements of macroscopic samples of DMSO that have been made below the crystallization temperature, where vitrification or crystallization could be confirmed visually. The unique contributions are (i) the modification of the cryomacroscope and creation of an experimental program to make thermal conductivity measurements of CPA based on the existing transient hot wire technique, (ii) to develop a protocol for making thermal conductivity measurements during rewarming portion of the cryoprotocol, and (iii), to begin generating a data bank of thermal conductivity of CPA and materials used in cryopreservation.

1.4 Synthetic Ice Modulators

Recently, a class of molecules has been designed and/or discovered to block ice growth or formation on a non-colligative basis, much like naturally occurring anti-freeze proteins in insects and polar fish [72]. In one case, 1,3-cyclohexane-diol (and similar molecules) were found by design specifically to bind to nucleators to stop growth [22]. In another case, polyvinyl alcohol appeared to inhibit heterogeneous nucleation [80]. Because their exact interaction with ice crystals may or may not be known, these materials can be referred to generally as synthetic ice modulators (SIMs). Small concentrations of SIMs, between 6-12% by volume, can cause a dramatic abatement of ice growth in a system when combined with CPA [72]. Thus, the addition of SIMs lessens the concentration of CPA required to vitrify, thereby reducing CPA toxicity. Chapter 3 focuses on investigating thermal conductivity of the CPA DP6 (3 M DMSO and 3 M Propylene Glycol in either water or a vehicle solution such as Euro Collins with HEPES) with the addition of SIMs in various conditions relevant to cryopreservation. These are the first published thermal conductivity measurements of CPA with SIMs.

[2] The melting temperature of 7 M DMSO is -53 °C. The glass transition temperature of 7 M DMSO is -130 °C [61].

1.5 Thermal Conductivity Effect on Heat Transfer Simulations of Cryopreservation

Studies have shown that the thermal conductivity selected in computation can have a large impact on internal cooling rates and temperature distributions in a bulky specimen, and may lead to considerable prediction errors. A study by Rabin in 2000 [57] sought to address the highly temperature-dependent thermal conductivity of ice that had been previously neglected or mistaken in bioheat transfer simulations. The study compared closed-form temperature solutions of one dimensional quasi steady systems (i.e.- low Stephan number) comprised of water or blood, with the thermal conductivity specifically isolated as the parameter of interest. This study found that approximating the thermal conductivity as temperature-independent overestimated the temperature distribution by up to 35 K for ice and 30 K for blood. Heat fluxes through the frozen region boundaries were found to be underestimated by a factor of two.

Another study by Choi and Bischof in 2010 numerically predicted thermal history of a one-dimensional slab of 50-, 5- and 0.5-mm thickness based on thermal properties of water ice versus thermal properties of phosphate-buffered saline (PBS) with 2 M glycerol [10]. Expectedly, they found that using thermal properties of water ice in place of real values for PBS+ 2M glycerol under-predicted total cooling time. They also found that errors due to incorrect thermal properties grow with increasing depth into the sample (away from cooling source). Thus, predictions for larger systems are more prone to errors caused by incorrect thermal properties.

The study presented in Chapter 5 investigates the thermal conditions associated with cryopreservation by vitrification in a kidney model, focusing on the cooling portion of the cryogenic protocol, from tissue loading with the CPA to cryogenic storage. This study is based on computer simulations using the finite element analysis (FEA) commercial code ANSYS and utilizes thermal properties of vitrified CPA measured with the novel technique presented in Chapter 2. The unique contributions presented here are: (i) thermal analysis of a vitrifying rabbit kidney adopted from a prior established experimental protocol of a rabbit kidney, where cryopreservation resulted in subsequent survival after transplantation, and (ii) exploring scale-up thermal effects on a 21-fold larger system containing a human kidney. Implications of the glassy state vs. crystalline state thermal conductivity on internal cooling rates are investigated.

Chapter 2

Large Thermal Conductivity Differences between the Crystalline and Vitrified States of DMSO with Applications to Cryopreservation

2.1 Objective

The objectives of the study presented in this chapter are: (1) to develop a thermal conductivity measurement system to be implemented on the experimentation stage of a scanning cryomacroscope apparatus—a visualization device that facilitate the correlation between measured data and physical events; (2) to demonstrate the applicability of the developed system on well characterized material, such as pure water ice and glycerol; and (3) to explore the thermal conductivity of DMSO in a concentration range of 2M and 10M and temperature range of -180°C and 25°C. The unique contribution in this study is three-fold: (i) in the development of a thermal conductivity measurement system based on a hot-wire method, which is suitable for cryogenic conditions in a cryomacroscopy environment; (ii) in the development of an experimentation protocol, which enables the application of hot-wire measurements in non-equilibrium conditions; and (iii) in the development of thermal conductivity databank with emphasis on DMSO, which is otherwise a relatively well characterized CPA [1,3,44,50,61,82] and which serves as a key ingredient in many CPA cocktails. In particular, it has been demonstrated in previous studies that high-concentration DMSO can be used as a model CPA for the analysis of thermo-mechanical stress in vitrification process [56].

2.2 Experimental Setup

The experimental setup is displayed in Fig. 2.1, based on a previously developed visualization device for physical events during cryopreservation—the scanning cryomacroscope [31].While the scanning cryomacroscope has been presented in detail previously, it is presented here in brief for the completeness of presentation. Herein the unique instrumentation contribution to scanning cryomacroscopy is the development of an alternative experimentation stage for thermal conductivity measurements, as schematically illustrated in Fig. 2.2. In general, the objective for cryomacroscopy is *in situ* investigation of the path-dependent process of cryopreservation. The scanning mechanism is integrated to enable the investigation of samples

larger than the field of view of the optical component—the borescope.

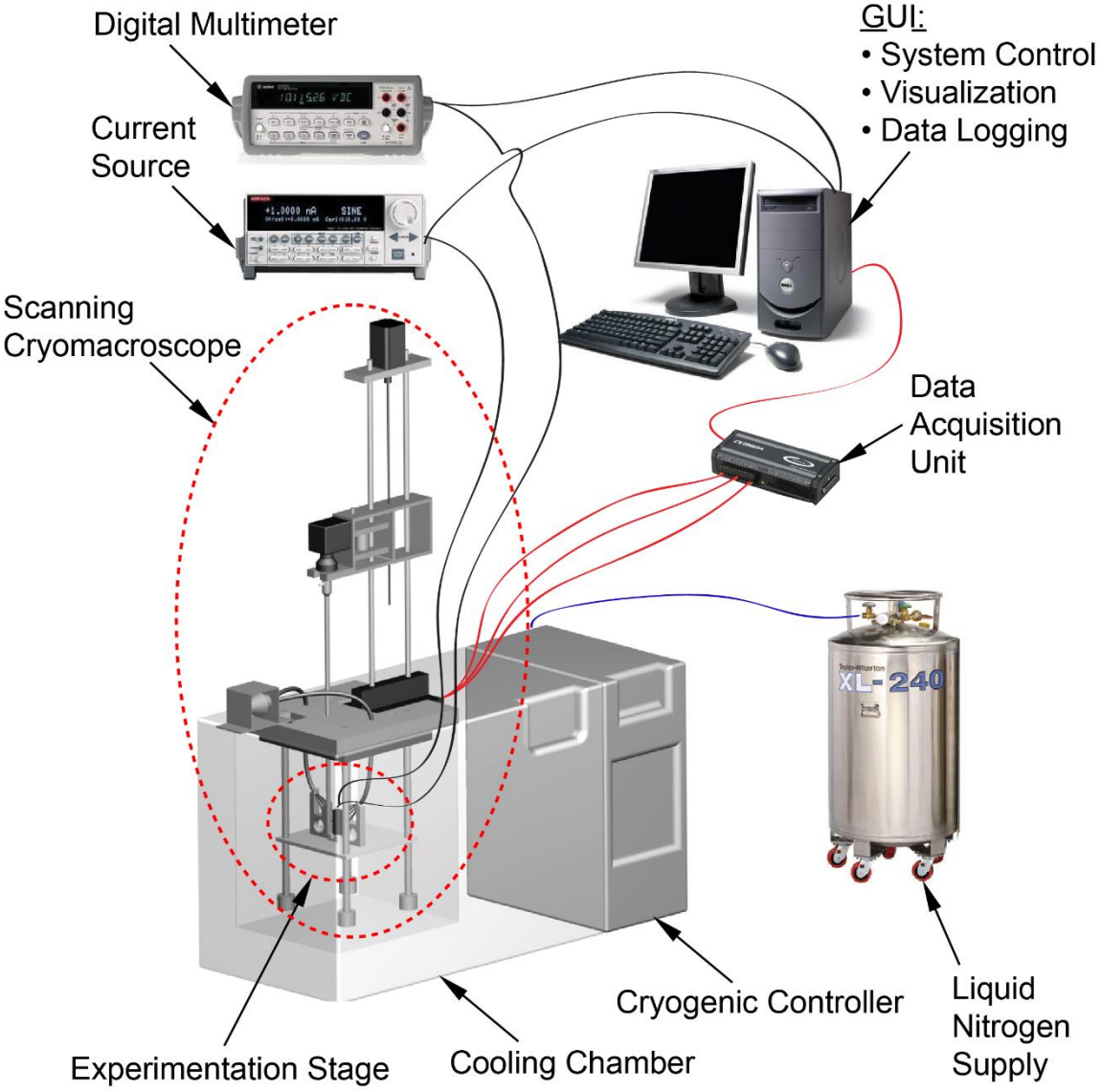

Figure 2.1: Schematic illustration of the scanning cryomacroscope setup and peripheral instrumentation *[31]*; the modified experimentation stage for thermal conductivity measurements is displayed with more detail in Fig. 2.2.

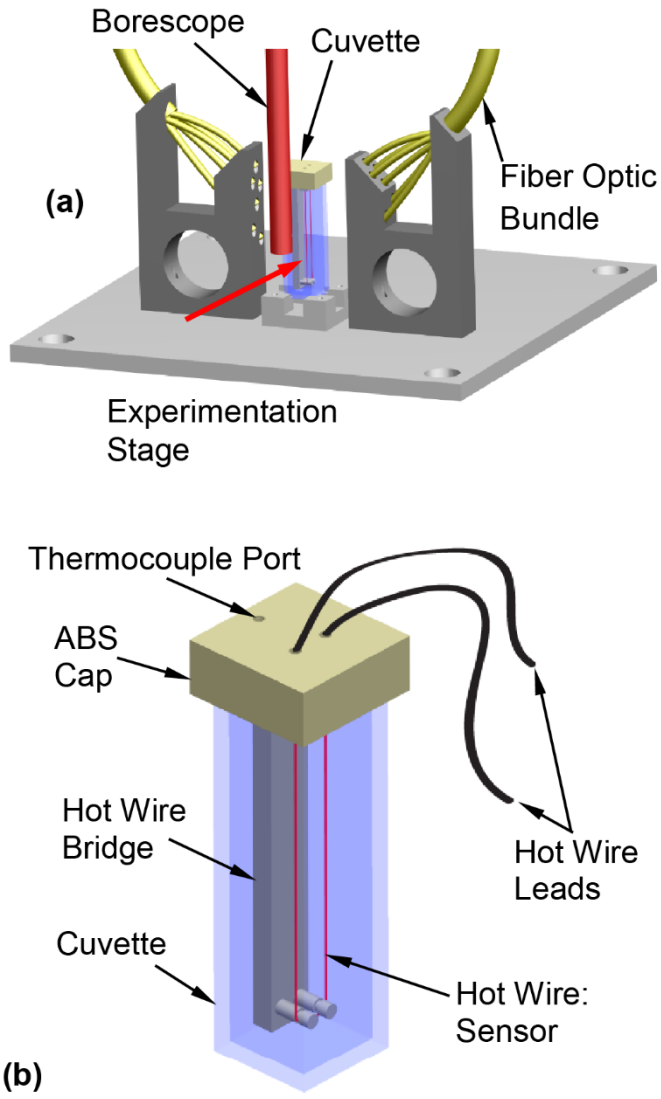

Figure 2.2: Schematic illustration of (a) the cryomacroscope experimentation stage (the red arrow represents the direction of view; see Fig. 2.5 for example), and (b) the hot wire sensor setup in the cuvette (sample container).

The experimentation stage of the cryomacroscope is placed inside the cooling chamber of a top-loaded cooler, Kryo 10-16, controlled by a dedicated controller, Kryo 10-20 (Planer Ltd., UK). The controller can be programmed to cool and rewarm the chamber at rates up to -50°C/min and +10°C/min, respectively, in a temperature range of -180°C and room temperature. Temperature control is achieved by release of liquid nitrogen vapors into a circulated stream of heated air. This is a dual parameter control process, targeting both the rate of nitrogen supply and

the power of the air heater.

The hot wire, which is the thermal conductivity sensor, is immersed in the sample during the entire cryogenic protocol, as displayed in Fig. 2.2(b). The hot wire is held in place by means of a cap and bridge in one unit, which is 3D printed from ABS. The specific wire configuration was selected to ensure electrical resistivity values compatible with the peripheral instrumentation used: a current source (Model 6221, Keithley Instruments, Inc., Ohio) and a digital multimeter (Model 34401A, Keysight Technologies, Inc., Santa Rosa, CA). Detailed design considerations for the hot wire setup are separately described below.

Two means of temperature measurements are integrated into the system: thermocouples and the hot wire sensor itself. Three T-type thermocouples are strategically placed: (1) on the inner surface of the cuvette at its geometric center; (2) on the outer surface of the cuvette, opposing the first thermocouple; and, (3) in the free stream of air/nitrogen vapor mixture circulating through the chamber. Uncertainty in thermocouple measurements is estimated as ±0.5°C. Uncertainty in hot wire temperature measurements is estimated to be linearly dependent upon temperature, ranging from ±2.8°C at -178°C to ±0.5°C at 17.7°C, where the uncertainty analysis is presented in Chapter 2.5.

2.3 Materials and Methods

The current study focuses on measuring thermal conductivity of DMSO solution in the concentration range of 2M and 10M. In addition, pure water ice and pure glycerol are measured for reference, where water ice data [34] defines the upper boundary of thermal conductivity for DMSO solutions, and glycerol is an alternative glass-forming CPA [4,6]. While thermal conductivity data for glycerol are available in the relevant cryogenic temperature range, thermophysical properties of CPAs in general are only sparsely available in the literature. Note that 7.05M DMSO has the same overall volumetric concentration of solutes as the CPA cocktail VS55, which has drawn significant attention in the cryobiology community in recent years. Both VS55 and 7.05M DMSO display similar mechanical behavior [56,62].

In general, the critical cooling rate to ensure vitrification decreases with the increasing concentration. With the achievable cooling rates in the cooling chamber of the current system, 2M DMSO will always crystallize, 10M DMSO will always vitrify, and intermediate concentrations may either crystallize or vitrify to a variable degree, depending upon the concentration and the

actual thermal history. Detailed analysis of the kinetics of crystallization in DMSO reveals a quite complex picture, which is beyond the scope of the current study. Being the first study of its kind and given the wide range of possibilities to design a thermal protocol in order to affect the path-dependent phenomenon of crystallization, a unified thermal protocol is selected for all experiments in the current study. The cooling rates in this thermal protocol are relevant to large-scale cryopreservation, which results in variable physical events along the cooling protocol for each DMSO concentration. Future studies are envisioned to study variable thermal protocols on specific DMSO concentrations, as well as expanding the base of knowledge to more complex CPA cocktails.

A typical thermal history for experimentation is displayed in Fig. 2.3, which is comprised of : (1) precooling the chamber to about 10°C before the cryomacroscope is loaded on top of the cooling chamber, in order to reduce condensation on the system components (not shown in Fig. 2.3); (2) cooling the sample at a rate of -5°C/min down to -130°C, then -2°C/min down to -180°C, with the reduced cooling rate below -130°C to avoid fracture formation as a result of thermo-mechanical stresses [17]; (3) passive rewarming up to -90°C, followed by a constant rewarming rate of +3°C/min back to room temperature. The passive rewarming phase at lower temperatures was required to eliminate temperature oscillations associated with cooling chamber control (inherent to the Kryo-16 and Kryo-20 systems).

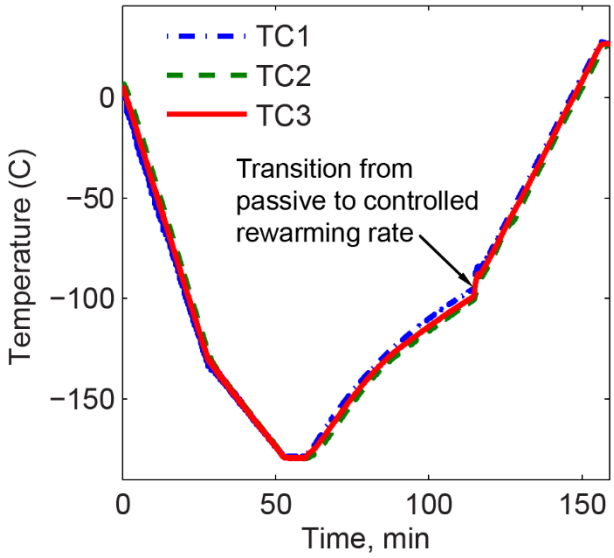

Figure 2.3: Typical thermal history during thermal conductivity measurements of 7.05M DMSO, where TC1 measures the chamber temperature, TC2 measures the wall inner surface at the center of one of the faces, and TC3 measures the temperature of the outer surface of the wall.

Hot-wire setup, design, and analysis

The transient hot-wire technique employs an immersed electrical resistor (a platinum wire) to simultaneously generate Joule heating and measure temperature (a resistance-based thermometer). In an ideal case, when the wire is immersed in an infinite domain (i.e., the CPA sample) and is subject to a step-like current activation, its transient thermal response can be best-fitted with experimental data to extract the thermal conductivity [39,52]. In practice, the parameters of the finite-volume sample, the sensor geometry, the electrical power generation, and peripheral sensing instrumentation must be carefully selected to closely approximate the ideal case, with the specific design considerations described below.

The hot-wire sensor in the current study is made from an approximately 70 mm-long platinum wire, 25.4 μm in diameter, having a 1.3 μm-thick isonel coating (A-M Systems, Sequim, WA, USA). A 4.5-mL polystyrene cuvette (Plastibrand) houses the sample fluid–sensor assembly as shown in Fig. 2. The sensor wire is held in a U-shape configuration by a 3D printed cap and bridge in one unit (ABS). The length of the wire in this configuration yields a resistance in the range of 16 to 16.8 Ω, which is selected for its compatibility with the expected thermal conductivity values. In practice, each hot wire sensor used is calibrated for its specific reference values. Joule

heating is generated by a constant current imposed for a period of 5 s, and is repeated in 35 s intervals during the entire rewarming phase of the thermal protocol (Fig. 2.3). Simultaneously, voltage changes across the wire are measured at a frequency of 60 Hz.

For data analysis, the temperature elevation of the wire is given by:

$$\Delta T = \frac{\Delta R}{\beta R_{ref}} \tag{2.1}$$

where β is the measured coefficient of thermal resistance (β=0.00411±0.00002°C^{-1}for the eight sensors fabricated in the current study), R_{ref} is a reference resistance selected at 21°C, and the change in resistance ΔR is calculated as the ratio of the voltage change ΔV as a result of the applied current I :

$$\Delta R = \frac{\Delta V}{I} \tag{2.2}$$

The multimeter leads and the current source leads are hooked in parallel to both ends of the sensor wire in a four-point configuration, to eliminate parasitic lead and reduced contact resistance.

The method for extracting the thermal conductivity from the heated wire measurements has been published previously [39,52] and is summarized here in brief for the completeness of presentation. By rearranging the analytical solution for the corresponding transient line-heating problem, the thermal conductivity of the surrounding sample can be expressed as:

$$k_{sample} = \frac{q/4\pi}{d(\Delta T)/d(\ln t)} \tag{2.3}$$

where ΔT is the temperature elevation in the wire, t is the elapsed time measured from the onset of heating, and q is the heat generation rate per unit length of wire:

$$q = \frac{I^2 R_0}{L} \tag{2.4}$$

where R_0 is the resistance of the wire at the onset of wire heating for the particular measurement, and L is the length of the platinum wire. Based on a detailed analysis of the solution provided by Nagasaka and Nagashima [52], the isonel coating does not influence the thermal conductivity measurements. This coating adds a constant shift to the transient temperature elevation, ΔT, while

the surrounding sample affects the slope of the same curve, which is essentially used to extract k_{sample}.

Since temperature measurements with the wire sensor always generate Joule heating, special measures are taken to distinguish between temperature measurements before and during heating experiments. The experimental protocol combines two steps: (i) low–current resistance measurements in the range of 2 to 4 mA, to establish the preheating wire temperature (measured for 1.58 s at 60 Hz); and, (ii) high-current measurements in the range of 40 to 105 mA, based on the expected thermal conductivity, which defines a hot-wire experiment and marked with t_i in Fig. 2.4 (duration of 0.5 s). Following the above analysis, the current applied during the low-current measurements is expected to elevate the wire temperature by the order of 10^{-4} °C, which is considered negligible for the current analysis.

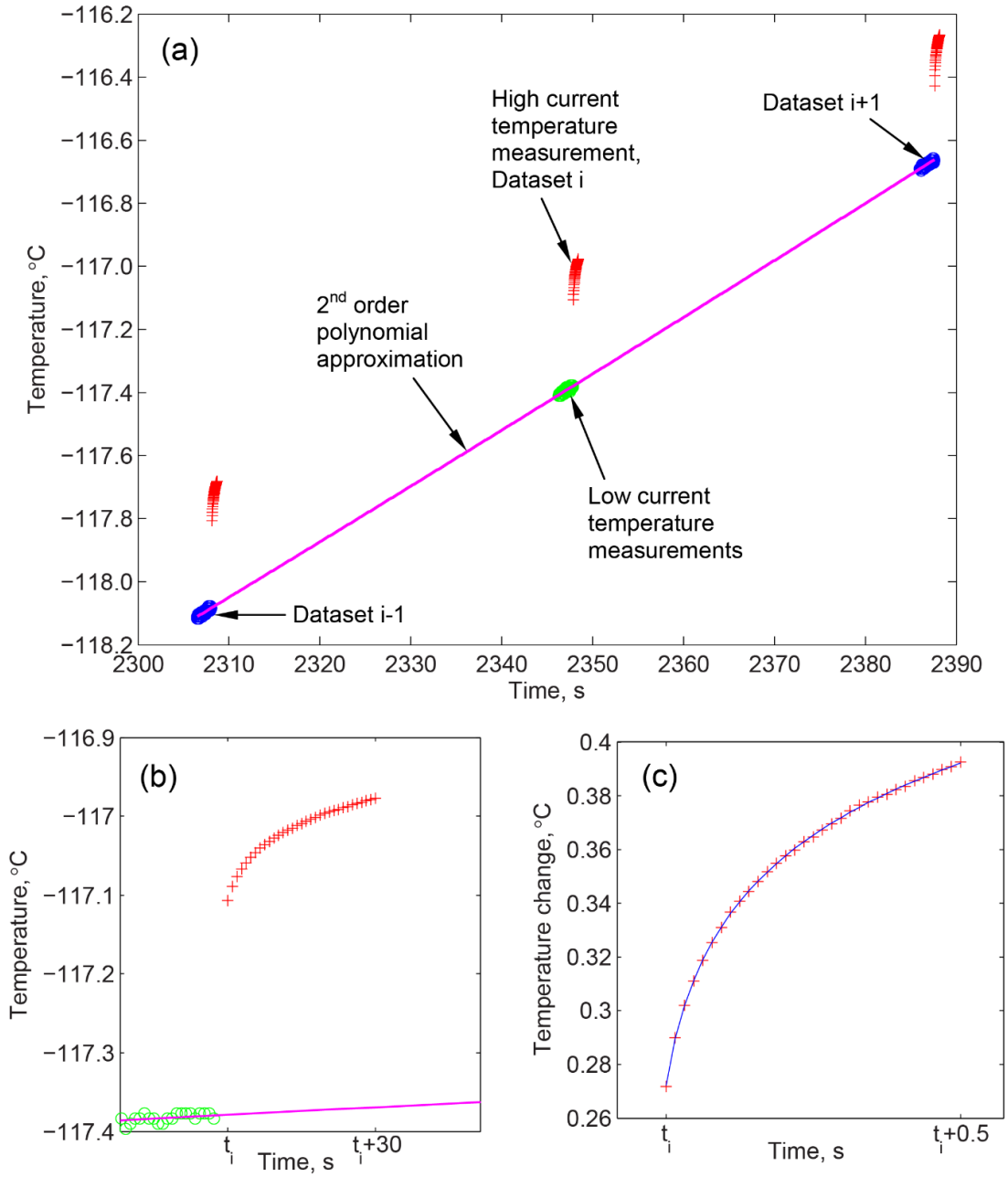

Figure 2.4: Temperature measurements during thermal conductivity experiments: (a) temperature results of three consecutive thermal experiments, where the change in the bulk sample temperature is best-fitted with a 2nd order polynomial; (b) a higher magnification of an experimental dataset; and (c) a temperature dataset used to calculate the thermal conductivity after the subtraction of the bulk sample rewarming curve, where the slope of the best-fitted curve on a semi-log plot is used to calculate the thermal conductivity (shown as a solid line in figure).

The solution presented in Eqs. (1)-(4) has been developed under the assumption of an infinite domain, initially at a uniform temperature. However, thermal conductivity measurements in the current study are taken continually, as the finite sample rewarms. Modeling the hot wire response in the current experimental setup with the above solution is justified for the following reasons (see also Fig. 2.4):

(i) the thermal penetration depth as a result of the step-like heat generation, x_{TP}, is conservatively estimated to be shorter than the distance between the hot wire and any adjacent object, as further discussed below in the context of Eq. (2.5);

(ii) the ideal model errors due to axial heat loss are negligible given the radius and length of the wire sensor, the ratio of k_{sample} to k_{wire}, and the ratio of $\rho_{sample}C_{p,sample}$ to $\rho_{wire}C_{p,wire}$ [37];

(iii) the time interval between consecutive heating events (35 s) is long enough for the wire to return to its surroundings temperature;

(iv) the heating rate of the wire during a single heating event (35°C/min on average), is an order of magnitude faster than the overall rewarming rate of the sample from cryogenic temperatures (about 3°C/min);

(v) the warming rate across the sample is uniform, causing the sample to rewarm as a thermally lumped system [57]; and,

(vi) the thermal mass of the wire is four orders of magnitude smaller than that of the heated region in the sample.

Thermal modeling of the hot wire response to step-like heating can be done with Eqs. (2.1)-(2.4) by decoupling it from the response of the bulk sample to cooling by the cooling chamber. These two processes can be decoupled since the heat diffusion equation is linear, which permits superposition of solutions [45]. The following procedure has been devised to capture the temperature of the bulk sample, as also illustrated in Fig. 2.4. A second-order polynomial is fit to the low-current measurements taken before each high-current dataset (t_{i-1}, t_i, and t_{i+1} in Fig. 2.4a). From each dataset, 95 consecutive measurements are used for the best-fit polynomial approximation, resulting in a total of 285 data points. Temperatures from the above polynomial approximation based on the low-current measurements are subtracted from the high-current measurements to evaluate ΔT as a result of the heating experiment. Finally, a linear curve is best-fitted for the rate of change of ΔT with respect to $\ln(t)$, which serves as the basis for the calculation of the thermal conductivity in Eq. (2.3). An example of this fit is shown in Fig. 2.4c.

In order to estimate the thermal penetration depth for the purpose of system design, a simplified solution for the temperature distribution in response to a sudden application of a constant heat flux is used [45]. This solution is given for a semi-infinite domain in a Cartesian geometry, while heat transfer around the heated wire is radial in nature. Hence, the solution from [45] serves as a conservative measure, where heat diffusion in a cylindrical system will make the actual penetration depth from the heated wire smaller and its decay faster. According to the above solution, the thermal penetration depth is given by:

$$x_{TP} = \sqrt{4\alpha t} \tag{2.5}$$

where α is the thermal diffusivity of the sample. In general, the thermal diffusivity increases with the decreasing DMSO concentration and with the decreasing temperature. For example, the thermal diffusivity of 2M DMSO at -180°C is 3.56×10^{-6} m^2/s, and a heating duration of less than 0.73 s is required since the wire is placed 3.2 mm away from the cuvette wall. In practice, all DMSO experiments were performed for a heating duration of 0.5 s. Reference experiments on pure water ice were all performed for a heating duration of less than 0.35 s for similar considerations.

2.4 Results and Discussion

Images of DMSO samples from the scanning cryomacroscope are shown in Fig. 2.5. Complete vitrification in 7.05M DMSO is displayed in Fig. 2.5(a) at an inner wall-surface temperature of -147°C, which is transparent in the glassy state. Also shown there is the wire sensor. Crystal growth in finger-like formation (also known as *dendrites*) is displayed in Fig. 2.5(b), for 2M DMSO at an inner wall-surface temperature of -10°C. Partial vitrification and complete crystallization in 6M DMSO are displayed in Figs. 2.5(c) and 2.5(d), respectively.

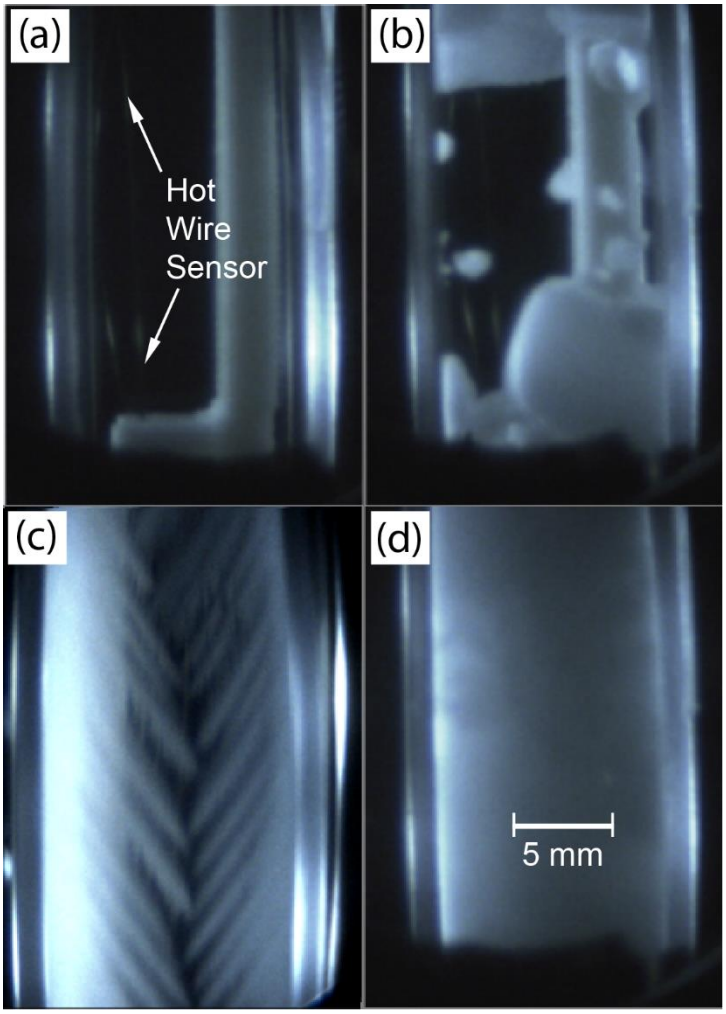

Figure 2.5: Cryomacroscope images of samples in various states: (a) a vitrified 7.05M DMSO sample at a temperature of -147°C; (b) a 2M DMSO sample undergoing crystallization in the form of dendrites at temperature of -10°C; (c) a partially crystallized 6M DMSO sample at a temperature of -58°C; and (d) a completely crystallized 6M DMSO solution at a temperature of -65°C.

Evidently, simultaneous observations of physical events during thermal conductivity measurements are essential for experimental data interpretation, where Fig. 2.5 displays only selected scenarios out of a virtually endless spectrum of possibilities. For example, localized DMSO boiling occurred during preliminary testing in the current study, which effectively resulted in measuring the thermal conductivity of DMSO vapors, although the surrounding material was maintained in cryogenic temperatures. That problem of boiling was created by overpowering the hot wire sensor. While this report focuses primarily on thermal conductivity data, it has been routinely compared against simultaneous video recording of each experiment.

2.4.1 Reference Experiments

The experimental apparatus and analysis technique were first evaluated against available data from the literature for relevant materials: pure water ice [57,65] and glycerol [4,6]. While glycerol is a known cryoprotective agent at various concentrations, comparable data in this temperature range is available only for pure glycerol [4,6].

Theoretical studies suggest that the thermal conductivity of water ice within the relevant portion of the cryogenic temperature range should have the following functional behavior (Fig. 2.6):

$$k = \frac{a}{T^b} \tag{2.6}$$

where *a* and *b* are constants and the temperature is measured in an absolute scale. For pure water ice, theoretical considerations suggest values of 546 W/m and 1 (dimensionless) for *a* and *b*, respectively [57]. Rabin compiled literature data and found that, while the theoretical behavior follows experimental findings, best-fitting this functional behavior with experimental data leads to *a* and *b* values of 2135 and -1.235, respectively [57]. Sakazume and Seki [65] suggested a more moderate increase of thermal conductivity with the decreasing temperature. It can be seen from Fig. 2.6 that the experimental data obtained in the current study follow closely the compilation by Rabin down to -100°C, Sakazume and Seki data down to -140°C, below which new the new experimental data lay in between those earlier publications.

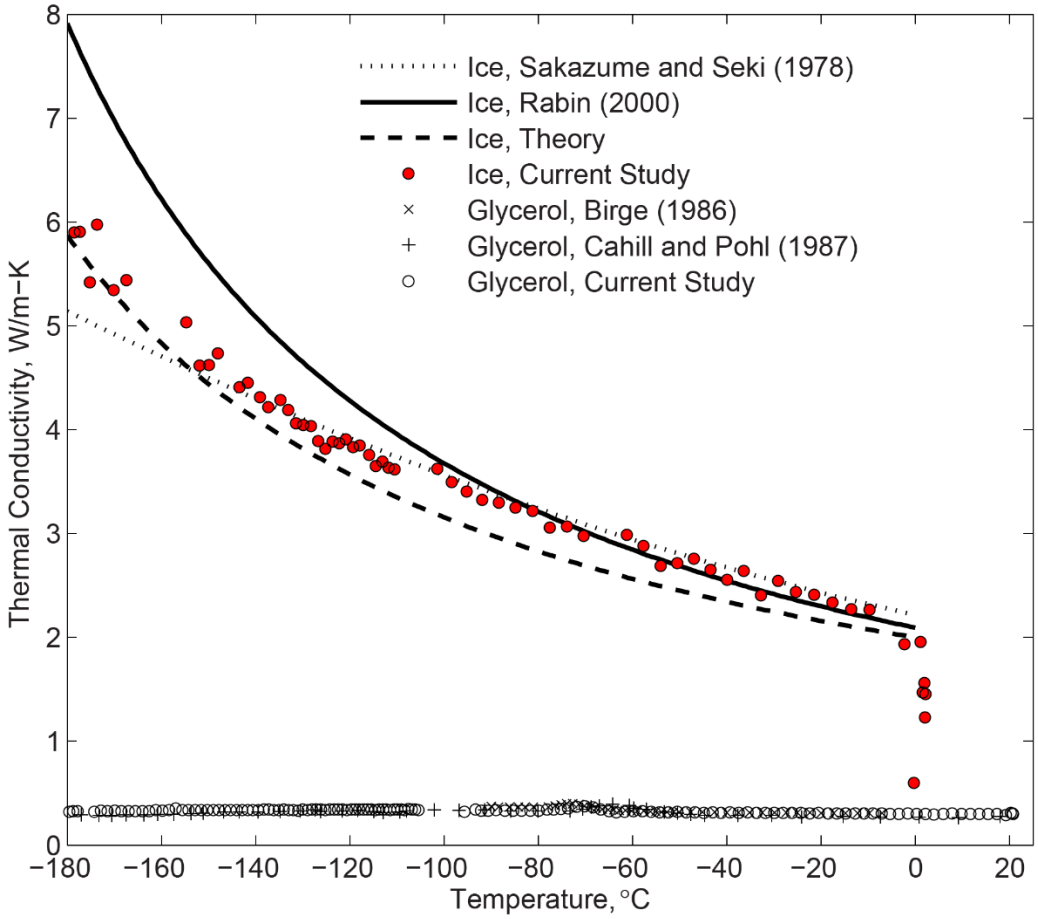

Figure 2.6: Thermal conductivity measurements of pure water ice and glycerol in the current study, compared with literature data, where the curve by Rabin (2000) *[57]* represents compilation of earlier literature data. Data is subject to uncertainty of ±0.03 W/m-°C, as discussed in Section 2.4.3, which is much smaller than the natural distribution of results around the average value.

In the amorphous state, the thermal conductivity of glycerol is expected to monotonically and moderately decrease with the decreasing temperature. It can be seen from Fig. 2.6 that the current experimental data agrees very well with the previously published data, where the differences are generally within the estimated uncertainty in thermal conductivity measurements, presented in section 2.4.3 to be less than or equal to 10% of the measured value. It is concluded that the experimental setup and analysis technique are valid for thermal conductivity measurements, and the discussion now turns to new findings on DMSO.

2.4.2 DMSO Experiments

Figure 2.7 displays experimental results for DMSO at various concentrations and for pure water ice for reference. A gap is present in each dataset around the time at which cooling chamber control is switched from passive to controlled heating. This change in control mode created temperature oscillations in the sample, which did not permit the data analysis technique discussed in conjunction with Fig. 2.4. Best-fit coefficients for all the experimental results shown in Fig. 2.7 are listed in Table 2.1 for the benefit of future cryobiology analyses.

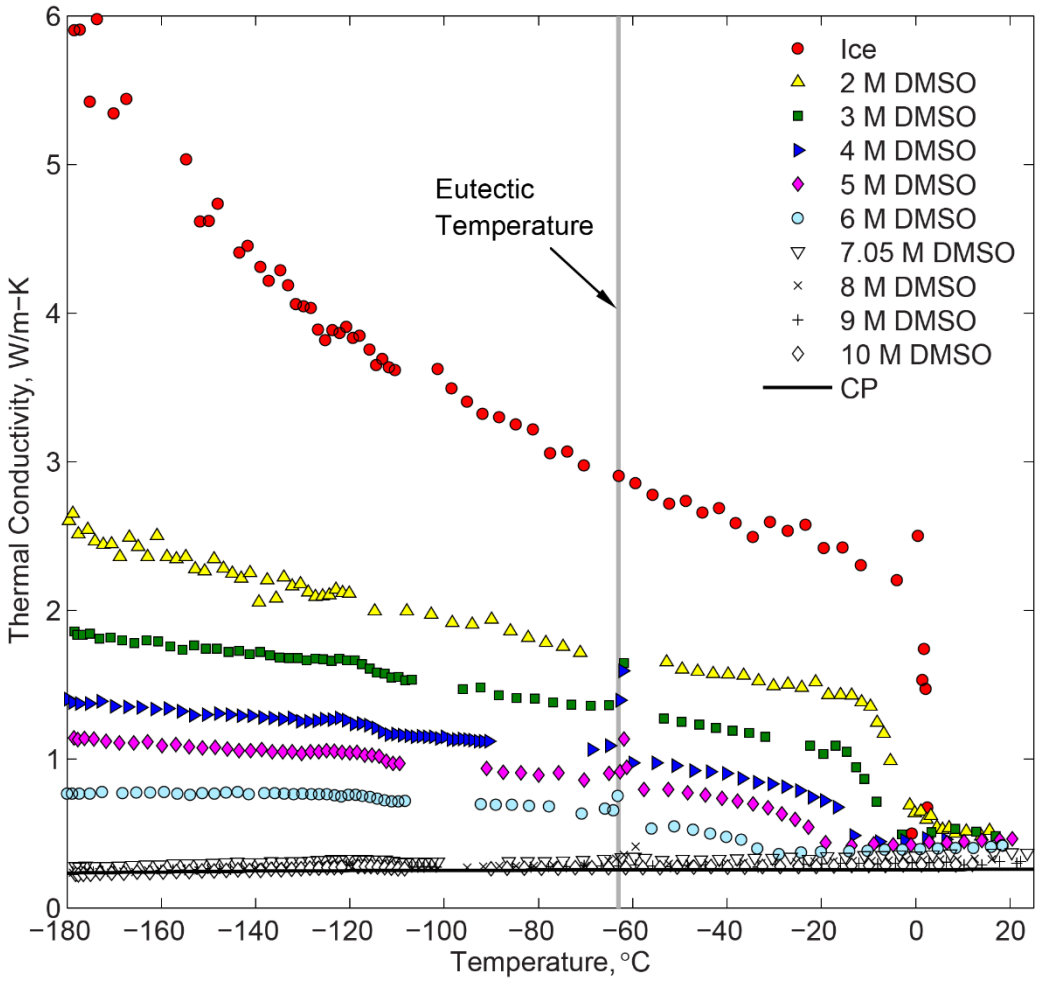

Figure 2.7: Thermal conductivity measurements of DMSO and pure water ice (subject to uncertainty of ±0.03 W/m-°C, as discussed in Section 2.4.3). The Cahill-Pohl model for thermal conductivity of amorphous solids is calculated with Eq. (2.8) for 10 M DMSO. Based on

cryomacroscope observations, DMSO concentrations of 6M or less underwent crystallization while concentrations of 7.05M and above vitrified.

Table 2.1. Best-fit polynomial approximation data for the thermal conductivity curves displayed in Fig. 2.7.

DMSO Concentration	Temperature Range	Polynomial Approximation, °C	R^2 value
2M	-180.0°C ... -9.4°C	$7.63\times10^{-10}\,T^4+1.60\times10^{-7}\,T^3+9.58\times10^{-6}\,T^2-6.01\times10^{-3}T+1.32$	0.981
	-9.4°C ...-0.2°C	$1.41\times10^{-3}\,T^2-6.86\times10^{-2}T+6.06\times10^{-1}$	0.991
3M	-180.0°C ... -17.5°C	$-1.55\times10^{-9}\,T^4-5.81\times10^{-7}\,T^3-8.01\times10^{-5}\,T^2-9.82\times10^{-3}T+9.00\times10^{-1}$	0.996
	-17.5 °C ... -11.5°C	$-3.97\times10^{-3}\,T^2-1.40\times10^{-1}T-1.84\times10^{-1}$	*
	-11.5°C ... -5.4°C	$-3.47\times10^{-3}\,T^2-1.25\times10^{-1}T-7.92\times10^{-2}$	*
	-5.4°C ... +18.2°C	$1.94\times10^{-3}\,T+5.04\times10^{-1}$	*
4M	-180.0° C ... -24.2°C	$-1.44\times10^{-9}\,T^4-6.42\times10^{-7}\,T^3-1.08\times10^{-4}\,T^2-1.16\times10^{-2}T+5.67\times10^{-1}$	0.997
	-24.2°C ... -17.3°C	$-2.11\times10^{-3}\,T^2-1.06\times10^{-1}\,T-5.35\times10^{-1}$	*
	-17.3°C ... -13.6°C	$-1.97\times10^{-4}\,T^3-1.51\times10^{-2}\,T^2-3.89\times10^{-1}T-2.56$	*
	-13.6°C ... +8.4°C	$-1.93\times10^{-3}\,T+4.58\times10^{-1}$	*
5M	-180.0° C ... -32.7°C	$-4.48\times10^{-10}\,T^4-2.76\times10^{-7}\,T^3-6.58\times10^{-5}\,T^2-1.16\times10^{-2}T+4.45\times10^{-1}$	0.997
	-32.7°C ... -19.2°C	$-9.77\times10^{-4}\,T^2-7.15\times10^{-2}T-6.00\times10^{-1}$	*
	-19.2°C ... +20.6°C	$1.23\times10^{-3}\,T+4.34\times10^{-1}$	0.916
6M	-180.0° C ... -47.3°C	$-6.65\times10^{-10}\,T^4-3.94\times10^{-7}\,T^3-1.01\times10^{-4}\,T^2-1.31\times10^{-2}T+9.31\times10^{-2}$	0.971
	-47.3°C ... -37.7°C	$-3.85\times10^{-4}\,T^2-3.97\times10^{-2}T-4.91\times10^{-1}$	*
	-37.7°C ... -32.0°C	$-6.27\times10^{-4}\,T^2-5.98\times10^{-2}T-9.06\times10^{-1}$	*
	-32.0°C ... +18.5°C	$9.25\times10^{-4}\,T+3.96\times10^{-1}$	0.932
7.05M	-180.0° C... +25.5°C	$-2.95\times10^{-10}\,T^4-6.87\times10^{-8}\,T^3-1.29\times10^{-6}T^2+7.42\times10^{-4}T+3.56\times10^{-1}$	0.982
8M	-180.0° C... +17.2°C	$-2.41\times10^{-10}\,T^4-5.76\times10^{-8}\,T^3-2.31\times10^{-6}T^2+5.57\times10^{-4}T+3.23\times10^{-1}$	0.989
9M	-180.0° C... +22.3°C	$-2.02\times10^{-10}\,T^4-4.57\times10^{-8}\,T^3-1.90\times10^{-6}T^2+3.25\times10^{-4}T+3.01\times10^{-1}$	0.948
10M	-180.0° C... +13.8°C	$-1.14\times10^{-10}\,T^4-1.50\times10^{-8}\,T^3+1.07\times10^{-6}T^2+3.74\times10^{-4}T+2.87\times10^{-1}$	0.987

* A dataset consisting of fewer than ten data points

It can be seen from Fig. 2.7 that the thermal conductivity of DMSO decreases with the increasing concentration. For DMSO concentration of 7.05M or higher, complete vitrification was observed while the thermal conductivity displayed a monotonic decrease in value with the decreasing temperature. In terms of thermal conductivity, the vitrified material appears to smoothly follow the trend from the liquid phase at higher temperatures. Crystallization was apparent in DMSO concentrations of 6M or less, which caused significant increase in the thermal conductivity as crystallization progressed. Thermal conductivity of DMSO follows opposing trends in the vitrified and crystallized phases, with the latter increasing with the decreased temperature.

2.4.3 Uncertainty Analysis

The uncertainty in thermal conductivity for a single measured value is estimated based on the uncertainty in the independent variables δx_j used for thermal conductivity calculations:

$$\delta k_{sample} = \sqrt{\sum_j \left(\frac{\partial k_{sample}}{\partial x_j} \delta x_j \right)^2} \tag{2.7}$$

where x_j stands for I, R_0, R_{ref}, β, and L. The thermal conductivity is expressed as:

$$k = \frac{I^2 V_i \beta R_0}{4\pi L C} \tag{2.8}$$

where C represents that derivative:

$$C = \frac{\partial(\Delta V)}{\partial(\ln t)} \tag{2.9}$$

Special consideration is given to the estimating of δC, by taking the maximum change in slope of the corresponding best-fit approximation, as discussion in the context of Fig. 2.4.

Table 2.2 lists the values for the key parameters affecting the uncertainty in thermal conductivity measurements, which yield an overall uncertainty of ±0.03 W/m-°C according to Eq. (2.7). From Fig. 2.8 it can be seen that the uncertainty in thermal conductivity measurements may be considered negligible for crystallized DMSO, but may get as high as 10% of the measured value

for vitrified DMSO at -180°C. From the right column in Table 2.2 it can be seen that the most significant contributor to the overall uncertainty is *C*. Even if all other sources of uncertainty could be eliminated, the uncertainty in measurement due to the best-fitting of *C* would yield ±0.029 W/m-°C. Note that in reality, the uncertainty in *C* belongs to a wide range of values, and only the worst-case scenario is considered in the current analysis. Finally, note that the above analysis aims at the uncertainty in thermal conductivity for a single measured value. Additional variations between experimental runs and also between specimens are not accounted for in this analysis.

Table 2.2: Typical data used to estimate the overall uncertainty in a thermal conductivity measurement, based on the hot wire measurement technique and a sample of 7.05M DMSO.

Parameter, x_j	Uncertainty, δx_j	$\left(\frac{\partial k_{sample}}{\partial x_j}\delta x_j\right)^2$
Current, I	0.09 mA	2.43×10^{-6}
Measurement voltage, V_i	6.96×10^{-6} … 2.75×10^{-4} V	2.08×10^{-8}
Coefficient of thermal resistance, β	5×10^{-5} °C^{-1}	2.14×10^{-5}
Reference resistance, R_0	5.7×10^{-3} Ω	1.38×10^{-8}
Wire length, L	1 mm	2.44×10^{-5}
Variation in the ratio C	1.76×10^{-7} … 1.72×10^{-5} V	5.89×10^{-7} … 8.57×10^{-4}

2.4.4 Crystallized DMSO

For samples that crystallized at lower temperatures, the thermal conductivity initially decreases with the decreasing temperature in the liquid phase, down to the onset of crystallization, and then dramatically increases as phase transition progresses. The temperature dependent behavior of thermal conductivity is consistent with other crystalline solids at temperatures above their peak in thermal conductivity. As crystals form in the sample, phonons become the dominant

heat carriers. As temperature decreases further, high energy phonons become deactivated and the reduced phonon population leads to decreased phonon-phonon scattering, while increasing the mean free paths of the remaining phonons. Thermal conductivity continues to increase with the decreasing temperature within the studied cryogenic range, as the phonon mean free paths continue to increase. At lower temperatures, which are typically beyond the scope of cryobiology applications, one would expect the thermal conductivity to peak and then decrease with decreasing temperature as deactivation of phonons ultimately outweighs increases in the mean free paths of residual low energy phonons.

Figure 2.8 displays the solid fraction in the water-DMSO mixture at equilibrium, extracted from a phase diagram [61]. Table 2.3 lists the liquidus temperature, T_l, above which the material is completely liquid, also shown in Fig. 2.8. Table 2.3 also lists the temperature at which melting completion is observed in the samples, T_m, based on thermal conductivity measurements. The temperature T_m is estimated as the intersection point of two best-fitted curves: (i) a first-order polynomial approximation for the liquid phase above T_l, and (ii) a second-order polynomial approximation for the closest five sampled points below T_l. Listed uncertainty values for T_l in Table 2.3 is attributed only to the quality of data harvesting from the phase diagram [61], while uncertainty in the compilation of the phase diagram remains unknown. While a good agreement is displayed between T_l and T_m in Table 2.3, it should be noted that T_l corresponds to equilibrium conditions, while T_m corresponds to a process. Nevertheless, the close agreement between T_l and T_m suggests that the rewarming rate (Fig. 2.5) can be considered very slow, and that the process can be first-order approximated as a quasi-steady.

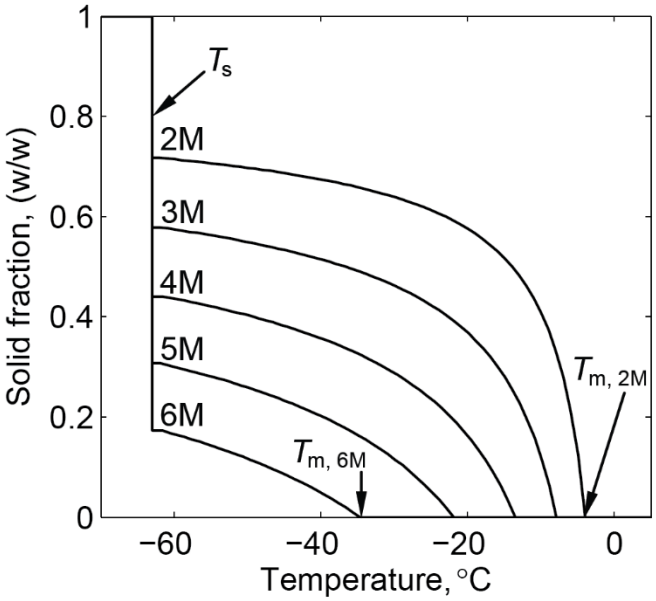

Figure 2.8: Solid fraction during solidification of a water-DMSO mixture, extracted from a phase diagram *[61]*.

Table 2.3. The temperature of melting completion based on experimental results, T_m, observed during thermal conductivity measurements in comparison with the liquidus temperature, T_l, from a water-DMSO phase diagram [61].

DMSO Concentration	T_l, °C ‡	T_m, °C †
2M	-3.9 ± 0.9	*
3M	-7.9 ± 0.9	-5.4 ± 0.5
4M	-13.5 ± 1.1	-13.6 ± 0.5
5M	-21.9 ± 1.3	-19.2 ± 0.5
6M	-34.6 ± 1.4	-32.0 ± 0.5

* No definite observation could be made

‡ Uncertainty only due to extraction of data from the phase diagram in [9]

† Uncertainty only due to temperature measurements in the current study

The solidus temperature, T_s, below which the material is completely solid, is -63±0.9°C for DMSO concentrations below 8M at equilibrium conditions (equal to the eutectic temperature found for 7.4M) [61]. Higher than expected thermal conductivity values were found around this temperature for DMSO concentration lower than 8M (highlighted with a gray line in Fig. 2.8), which are non-physical artifacts, resulting from latent effects and the method of thermal conductivity interpretation (illustrated in Fig. 2.4). In practice, experimental data suggests the onset of melting around the predicted value of -63°C with peak value between -62.3° and -60.1°C, for lower concentrations than 8M.

Within the temperature range one may assume lower concentration DMSO solutions as composed of water ice crystals suspended in molten and concentrated DMSO. A simple way of estimating the effective thermal conductivity of a randomly distributed two-component medium is proposed by the Bruggeman model [76]:

$$v_1 \frac{\kappa_1 - \kappa_e}{\kappa_1 + \kappa k_e} + (1 - v_1) \frac{\kappa_2 - \kappa_e}{\kappa_2 + 2\kappa_e} = 0 \qquad (2.10)$$

where is the volume fraction, κ is the thermal conductivity of the components, the indices 1 and 2

refer to different medium components, and the index κ_e is the effective thermal conductivity of the medium.

Figure 2.9 displays an estimate of the effective thermal conductivity of DMSO based on the Bruggeman model, using the following assumptions: (i) component 1 is ice with thermal conductivity value of 2.5 W/m-°C, which is its actual value at -60°C; (ii) component 2 is 6M DMSO at the liquid state, with a thermal conductivity value of 0.43 W/m-°C, which is its actual value at -35°C; and, (iii) the thermal conductivity of each component is temperature independent. The above simplifying assumptions follow the observation that the thermal conductivity difference between pure water ice and liquid 6M DMSO within the range of interest is expected to be much more significant than the temperature dependency of each of those components individually over the same temperature range. Furthermore, while the results are more suitable to investigate phase transition in the 6M DMSO solution, the comparison with other solution concentrations is also insightful.

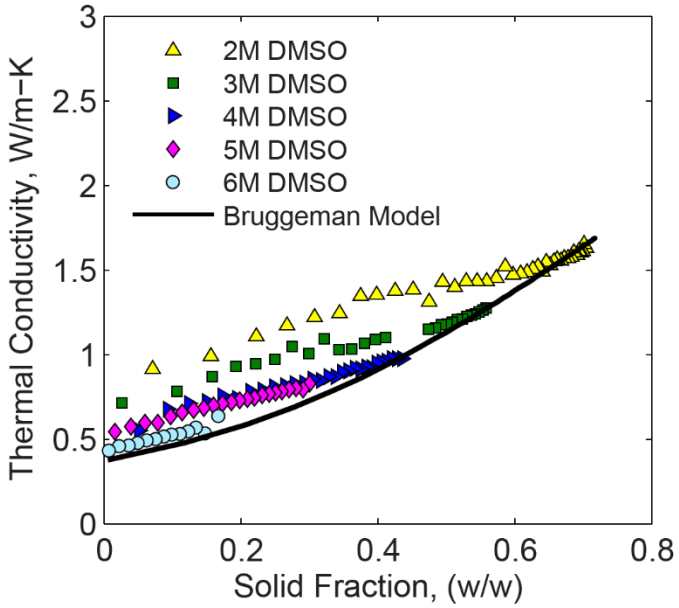

Figure 2.9: Thermal conductivity as a function of solid fraction for DMSO at various concentrations, where the Bruggeman model is calculated with Eq. (2.10) for 6M DMSO.

It can be seen from Fig. 2.9 that the effective thermal conductivity increases with the increasing solid fraction, following a similar trend for the different concentrations. The maximum solid fraction for each concentration dataset is at the solidus temperature. The prediction of the

Bruggeman model suggests that CPA undergoing phase transition may be first-order modeled as uniformly suspended crystals in a molten solution. The simplified model based on a 6M DMSO concentration and pure water ice properties appears to represent the same trend for other solution concentrations at higher solid fractions.

2.4.5 Vitrified DMSO

No crystal formation was observed with the scanning cryomacroscope for DMSO concentrations of 7.05M or higher. For reference, Table 2.4 lists the liquidus and solidus temperatures for those higher-concentrations solutions extracted from a phase diagram [61], which reflects near-equilibrium conditions. Thermal conductivity for these concentrations monotonically decreases with decreasing temperature, which is typical of amorphous solids such as SiO_2 and Poly(methyl-methacrylate) (PMMA). This behavior is attributed to the lack of long-range order typical of crystalline materials [8]. Similarly to crystalline DMSO, the thermal conductivity increases in value with the decreasing DMSO concentration, but with a much weaker dependency on concentration. A previously published thermal conductivity value of 0.32 W/m-°C for 7M DMSO at -20°C [82] is found to be in close agreement with a value of 0.34 ± 0.01 W/m-°C at -20.7 ± 0.8°C found in the current study.

Table 2.4: The liquidus temperature, T_l, and the solidus temperature, T_s, of solution concentrations observed to vitrify in this study, from a water-DMSO phase diagram [61].

DMSO concentration	T_l, °C	T_s, °C
7.05M	-54.2	-63.0
8M	-61.5	-63.0
9M	-67.3	-70.2
10M	-56.5	-72.8

Careful examination of the thermal conductivity data displayed in Fig. 2.7 suggests minor latent heat effects for the 7.05M and 8M concentrations near the solidus temperature, which is associated with rewarming-phase crystallization (RPC). In general, RPC can either be the effect of devitrification—crystal formation during rewarming, or recrystallization—crystal growth from nuclei already formed during cooling. Either way, comparing the thermal conductivity trend and values below and above the solidus temperature suggests only minor crystallization effects.

To rationalize the observed temperature-dependent data for vitrified DMSO, it is compared with the Cahill-Pohl (C-P) model for thermal conductivity of amorphous solids [8]. The model is based on a scenario of an amorphous solid, where phonon-like collective vibrations of the atoms exist but scatter with very short mean free paths, equal to half of their wavelength. In contrast, the phonon mean free paths in crystals are hundreds to thousands of times their wavelength, leading to larger thermal conductivities as observed for lower molarity DMSO solutions. The C-P model has been validated against numerous amorphous materials including polymers and glasses. The C-P expression for thermal conductivity is:

$$k_{\min} = \left(\frac{\pi}{6}\right)^{1/3} k_B n^{2/3} \sum_i v_i \left(\frac{T}{\theta_i}\right)^2 \int_0^{\theta_i/T} \frac{x^3 e^x}{\left(e^x - 1\right)^2} dx; \quad \theta_i = v_i \left(\hbar / k_B\right)\left(6\pi^2 n\right)^{1/3} \tag{2.11}$$

where *i* refers to the polarization (e.g., transverse) of the phonon, $\hbar$ is the reduced Planck's constant, k_B is Boltzmann's constant, and the model inputs v_i and n are the speed of sound and the number density of oscillators (typically one atom is an oscillator, but in some solids stiff bonds make clusters of atoms into oscillators), respectively.

Figure 2.7 displays the minimum thermal conductivity prediction for 10M DMSO based on the C-P model, using the following parameters: (i) the speed of sound is 1703 m/s for 10.12 M DMSO (used for all three polarizations) [1], and (ii) the number density of oscillators in 10M DMSO is $2.78\times10^{28}/m^3$, based on the number density of DMSO and H_2O molecules, and the number of oscillators per molecule where stiff bonds are assumed between C-H and S=O in DMSO (each DMSO is three oscillators), and O-H in H_2O (each H_2O is one oscillator) in the temperature range of interest [6]. It can be seen from Fig. 2.7 that the C-P model can be a useful tool in estimating the thermal conductivity in vitrified DMSO.

2.5 Conclusions

In this chapter, the significance of the dependency of thermal conductivity on temperature and cooling rate has been established as an important consideration for heat transfer analyses of large systems undergoing cryopreservation [57]. This study is aimed at quantifying this dependency in DMSO solutions, while taking into account two physical processes that affect the outcome of cryopreservation: crystallization and vitrification. This study utilizes the established hot-wire measurement technique, which is integrated for the first time into a recently developed device to visualize physical events during cryopreservation, termed the scanning cryomacroscope. The role of cryomacroscopy in this study is to verify the phase of state in the sample, while its thermal conductivity is continually measured along the thermal protocol. Also included in this chapter are reference measurements of thermal conductivity for pure water ice and glycerol, with comparable data available from the literature.

It is shown in this chapter that the thermal conductivity of the crystallized material varies significantly with the concentration, where samples in the concentration range of 2M and 6M DMSO where found to crystallize in the experimented thermal protocol. The thermal conductivity of the crystallized material is found to increase with the decreasing temperature, in the temperature range applicable to cryobiology (above -180°C in the study described in Chapter 2). This behavior is expected to change at near-absolute zero temperatures. In contrast, the thermal conductivity of vitrified DMSO solutions is not observed to be significantly dependent on concentration. The dependency of the thermal conductivity upon temperature of the vitrified solution appears to follow the same trend from the liquid phase, which is to gradually decrease in thermal conductivity with the decreasing temperature. These opposing trends between the crystallized and vitrified material reach a tenfold difference at -180°C, which defines the lower boundary of the current experimental investigation. Such dramatic differences can drastically impact heat transfer during cryopreservation and their quantification is therefore critical to cryobiology

Chapter 3

Thermal Conductivity of the Cryoprotective Cocktail DP6 in Cryogenic Temperatures, in the Presence and Absence of Synthetic Ice Modulators

3.1 Objective

The objective of the study presented chapter is to investigate the thermal conductivity of the cryoprotectant cocktail DP6 in combination with synthetic ice modulators (SIMs). This objective is met by using the measurement device and technique presented in Chapter 2. DP6 is a mixture of 3 M dimethyl sulfoxide (DMSO) and 3 M propylene glycol, which has received significant attention in the cryobiology community in recent years and which has been investigated intensively at the Biothermal Technology Laboratory. Tested SIMs include 6% 1,3Cyclohexanediol, 6% 2,3Butanediol, and 12% PEG400 (percentage by volume). Effects of variable cooling rate and Euro-Collins vehicle solution on thermal conductivity are also explored. The unique contribution in this study is in the development and first publication of thermal conductivity data for CPA+SIMs cocktails.

3.2 Materials and Methods

The experimental setup used in this chapter has been presented in the previous chapter, and consists of: (i) the scanning cryomacroscope [31], which enables visualization of vitrification, and (ii) a transient hot-wire set-up for simultaneously measuring thermal conductivity [39,52]. With reference to Fig. 3.1, a hot-wire sensor is immersed in the CPA cocktail, contained in a cuvette, and placed on the experimental stage of the cryomacroscope. During experiments, the cryomacroscope is loaded on top of a controlled-rate cooling chamber (Kryo 10-16 chamber with a Kryo 10-20 controller, Planer Ltd., UK). Refer to Chapter 2.1 regarding more specific details about the experimental setup, measurements, and uncertainty analysis.

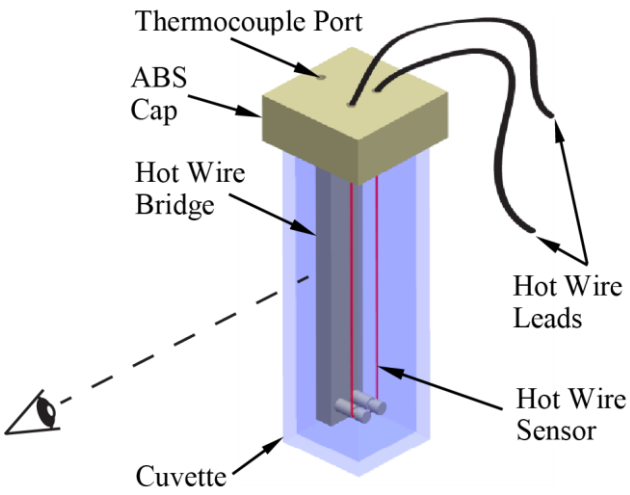

Figure 3.1: Schematic illustration of the transient hot-wire sensor setup; the dashed line represents the direction of visualization by the scanning cryomacroscope [31].

3.2.1 Thermal Protocol

Consistent with previous studies [2,14,30,31,68], the thermal protocol comprises six phases: (i) precooling to approximately 12 °C, to reduce condensation on the cryomacroscope optics; (ii) rapid cooling at a rate H_1 to temperature T_1 (typically 20 °C above T_g); (iii) slow cooling at a rate H_2 down to storage temperature T_s; (iv) hold time t_s until the specimen reaches thermal equilibrium at the storage temperature; (v) passive rewarming at a rate H_3 up to -100 °C; and, (vi) controlled-rate rewarming at a rate of H_4 back to room temperature. The passive cooling below -100 °C was selected to eliminate temperature oscillations inherent to the controlled-rate cooling chamber in very low temperatures (see hardware specification in Chapter 2). Furthermore, since significant crystallization is only expected to occur well above that temperature threshold, the uncontrolled cooling is not expected to affect thermal conductivity measurements. Fig. 3.2 displays representative thermal histories as measured from a temperature sensor (T-type thermocouple) attached to the inner surface of the cuvette. Table 3.1 lists the specific thermal history values used in the current study for the various compounds measured.

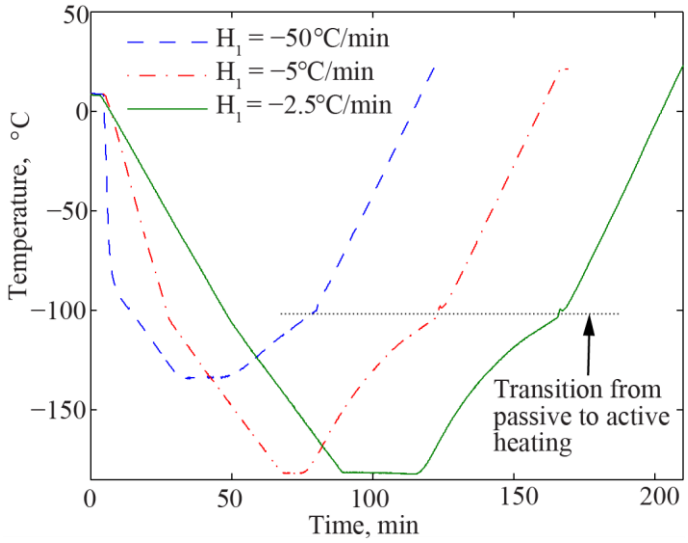

Figure 3.2: Representative thermal histories during thermal conductivity measurements of DP6 mixed with PEG400, where temperature data were measured at the center of the cuvette inner wall surface. For all experiments the following rates were kept constant: H_2 = -2 °C/min, H_3 = 1.7 °C/min (average passive rewarming), and H_4 = 3 °C/min.

Table 3.1: Summary of thermal history parameters used in this study, where all protocols included H_2= -2°C/min and H_3= 3°C/min as illustrated in Fig. 3.2.

CPA	Vehicle Solution	H_1, °C/min	T_1, °C	$T_{storage}$, °C
DP6 + 6% 1,3CHD	None	-2.5	-100	-180
		-5	-100	-180
		-50	-80	-130
	Euro-Collins	-2.5	-100	-180
		-5	-100	-180
		-50	-80	-130
DP6 + 6% 2,3BD	None	-2.5	-100	-180
		-5	-100	-180
		-50	-80	-130
	Euro-Collins	-2.5	-100	-180
		-5	-100	-180
		-50	-80	-130
DP6 + 12% PEG400	None	-2.5	-100	-180
		-5	-100	-180
		-50	-80	-130
	Euro-Collins	-2.5	-100	-180
		-5	-100	-180
		-50	-80	-130
DP6	None	-2.5	-100	-180
		-5	-100	-180
		-50	-80	-130
	Euro-Collins	-2.5	-100	-180
		-5	-100	-180
		-50	-80	-130

In particular three representative initial cooling rates were selected (H_1) to investigate the thermal conductivity within the temperature range most prone to crystallization (investigated rates of 1 °C/min to 50 °C/min). At lower temperatures, slow cooling and rewarming rates (H_2 and H_3, respectively) were selected to prevent fracturing and possibly damaging the hot-wire (-2 °C/min for cooling and an average of 1.7 °C/min during passive rewarming). In some experiments the sample was cooled to the lower limit of the cooling chamber, -180 °C, while in other experiments a temperature of -130 °C was selected, which decreased the likelihood of fracturing in the glassy state [31]. Note that T_g for DP6 is -119 °C [30].

3.2.2 Materials tested

This study is focused on DP6 in the absence and presence of SIMs. DP6 is a mixture of 3 M DMSO and 3 M propylene glycol. Consistent with previous studies [18], this study uses Euro-Collins (EC) as a vehicle solution for DP6 but selected experiments were also conducted in the absence of Euro-Collins for reference (i.e, DP6 in pure water). Consistent with a recent study [18], DP6 experiments were conducted with one of the following SIMs: 6% 1,3 Cyclohexanediol (1,3CHD); 6% 2,3 Butanediol (2,3BD), and 12% PEG400 (percentage by volume). All solutions were frozen and thawed three times prior to experimentation to remove dissolved gases, which might affect the readings.

3.3 Results and Discussion

Fig. 3.3 displays experimental results for DP6, DP6+SIMs, and previously published data for 6 M DMSO for reference. Due to the close range of thermal conductivity data for all the SIM-based cocktails tested, the corresponding results are displayed as a range only in Fig. 3.3, while the specific distribution for the cocktails is presented in Fig. 3.4. Table 3.2 lists least-square-error, best-fit polynomial coefficients for the data displayed in Fig. 3.3 and Fig. 3.4, as a service for future analyses of thermal effects during SIM-based cryopreservation by vitrification (coefficient values were determined by the Matlab function polyfit, while the polynomial order was defined by the authors).

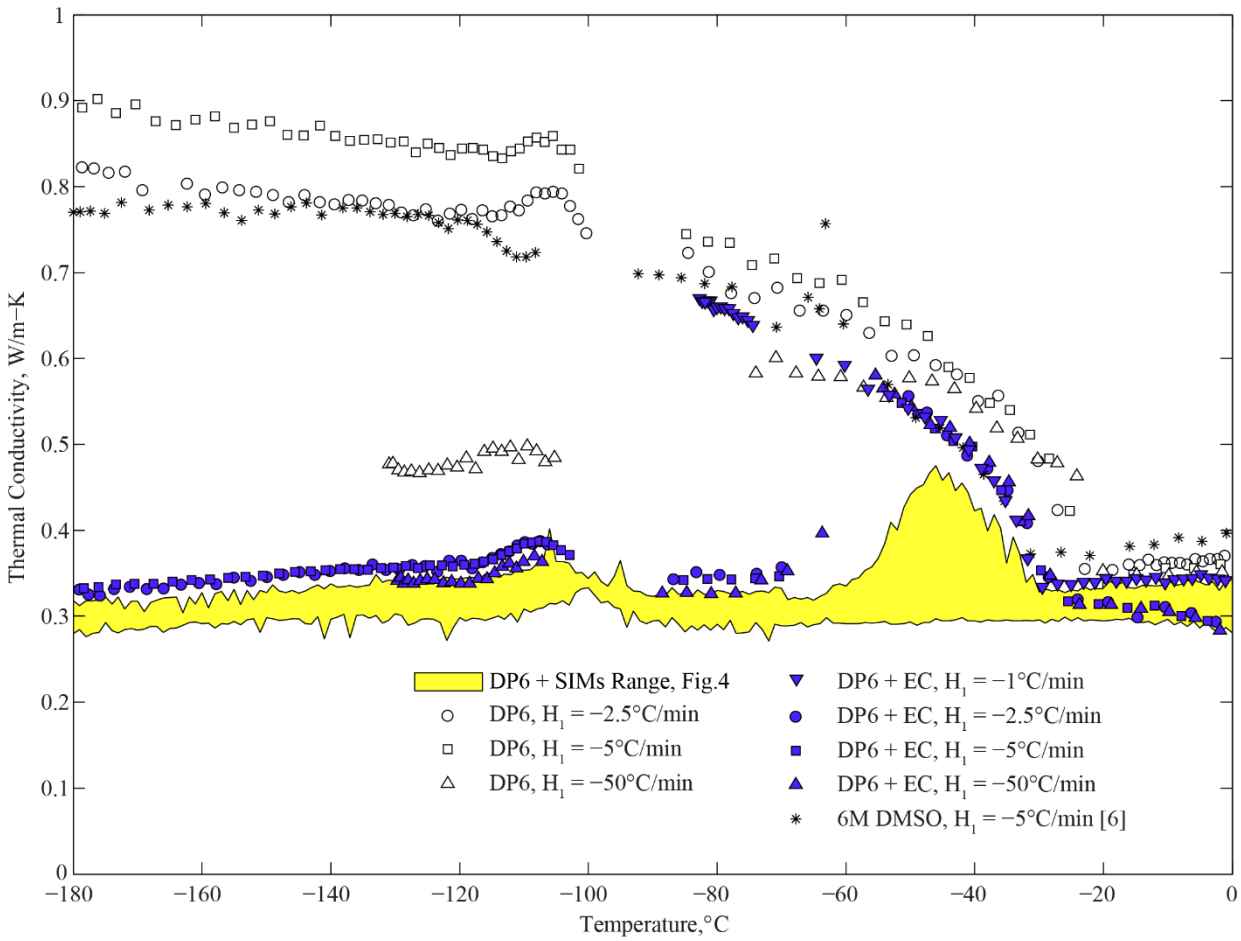

Figure 3.3: Measured thermal conductivity of DP6 in the presence and absence of SIMs and EC; 6M DMSO is also shown for reference *[14]*. At the applicable cooling rate, the glass transition temperature for 6 M DMSO is -132 °C, and -119 °C for DP6 *[30,40]*. The eutectic temperature for DMSO is -63 °C at a concentration of 6 M *[61]*. Estimated uncertainty of ±0.03 W/m-°C, as discussed in Section 2.4.3.

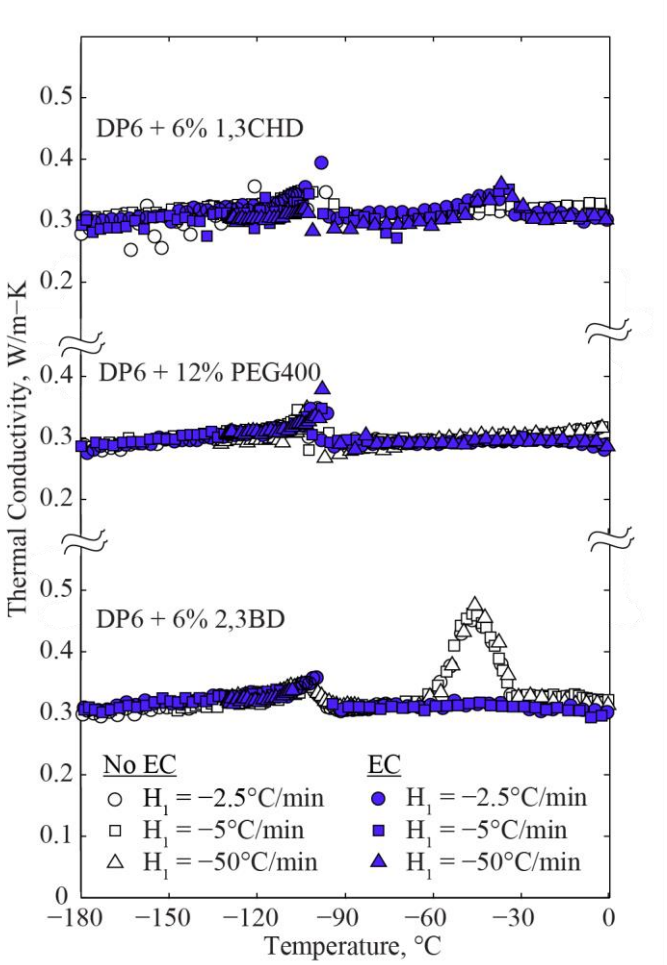

Figure 3.4: Thermal conductivity measurements of DP6 in the presence of SIMs, where the glass transition temperature of DP6 is −119 °C at the applicable cooling rates *[30]*.

Table 3.2: Best-fit polynomial approximation for thermal conductivity curves displayed in Figs 3.3 and 3.5; average values are given in cases where (i) the span of the polynomial approximation of thermal conductivity is smaller than two standard deviations of the experimental data over the relevant temperature range (denoted by †), or (ii), where extensive RPC effects over a given data set are observed (denoted by ‡).

CPA-SIM Cocktail	Vehicle Solution	H_1	Temperature Range, °C	Polynomial Approximation, °C	R^2
DP6 + 6% 1,3CHD	None	-2.5	-180.0 … -112.7	$4.86\times10^{-4}T+3.85\times10^{-1}$	0.930
			-89.9 … 0.0	$5.69\times10^{-10}T^4+1.25\times10^{-7}T^3+1.10\times10^{-5}T^2+6.59\times10^{-4}T+3.32\times10^{-1}$	0.919
		-5	-180.0 … -113.2	$3.97\times10^{-4}T+3.75\times10^{-1}$	0.912
			-85.8 … 0.0	$6.66\times10^{-10}T^4+1.09\times10^{-7}T^3+8.21\times10^{-6}T^2+5.69\times10^{-4}T+3.30\times10^{-1}$	0.969
		-50	-129.3 … -108.6	0.31†	-
	EC	-2.5	-180.0 … -116.7	$4.16\times10^{-4}T+3.74\times10^{-1}$	0.904
			-89.1 … 0.0	$-1.95\times10^{-9}T^4-3.40\times10^{-7}T^3-2.39\times10^{-5}T^2-8.65\times10^{-4}T+3.02\times10^{-1}$	0.570
		-5	-180.0 … -109.7	$3.98\times10^{-4}T+3.60\times10^{-1}$	0.912
			-87.0 … 0.0	0.31‡	-
		-50	-129.0 … -112.1	0.30†	-
			-79.8 … 0.0	0.30‡	-
DP6 + 6% 2,3BD	None	-2.5	-180.0 … -119.9	$4.73\times10^{-4}T+4.00\times10^{-1}$	0.884
			-93.3 … 0.0	0.33‡	-
		-5	-180.0 … -112.8	$3.39\times10^{-4}T+3.59\times10^{-1}$	0.723
			-84.2 … 0.0	0.32‡	-
		-50	-129.7 … -108.8	0.31†	-
DP6 + 12% PEG400	None	-2.5	-180.0 … -113.3	$4.69\times10^{-4}T+3.66\times10^{-1}$	0.928
			-93.6 … 0.0	$-6.44\times10^{-10}T^4-6.74\times10^{-8}T^3+4.36\times10^{-6}T^2+7.53\times10^{-4}T+3.19\times10^{-1}$	0.968
		-5	-180.0 … -112.1	$4.43\times10^{-4}T+3.66\times10^{-1}$	0.940
			-90.7 … 0.0	$3.11\times10^{-10}T^4+8.67\times10^{-8}T^3+1.15\times10^{-5}T^2+7.84\times10^{-4}T+3.18\times10^{-1}$	0.961
		-50	-131.7 … -112.6	0.30†	-
			-90.7 … 0.0	$-1.21\times10^{-10}T^5-2.01\times10^{-8}T^4-8.59\times10^{-7}T^3+3.58\times10^{-6}T^2+9.54\times10^{-4}T+3.21\times10^{-1}$	0.985
	EC	-2.5	-180.0 … -109.8	$4.17\times10^{-4}T+3.59\times10^{-1}$	0.919
			-93.7 … 0.0	$-5.16\times10^{-10}T^4-2.23\times10^{-7}T^3-2.67\times10^{-5}T^2-1.08\times10^{-3}T+2.82\times10^{-1}$	0.970
		-5	-180.0 … -110.7	$4.25\times10^{-4}T+3.63\times10^{-1}$	0.913
			-91.1 … 0.0	$4.08\times10^{-10}T^4-3.94\times10^{-8}T^3-1.19\times10^{-5}T^2-5.10\times10^{-4}T+2.91\times10^{-1}$	0.803
		-50	-129.5 … -108.7	0.31†	-
			-84.7 … 0.0	$-4.10\times10^{-14}T^5+2.12\times10^{-9}T^4+1.77\times10^{-7}T^3-4.32\times10^{-6}T^2-4.65\times10^{-4}T+2.90\times10^{-1}$	0.839
DP6	None	-2.5	-180.0 … -40.7	$1.20\times10^{-9}T^4+4.10\times10^{-7}T^3+3.11\times10^{-5}T^2-2.91\times10^{-3}T+4.29\times10^{-1}$	0.990
			-40.7 … -22.9	$-3.58\times10^{-4}T^2-3.52\times10^{-2}T-2.65\times10^{-1}$	0.983
			-22.9… 0.0	$7.03\times10^{-4}T+3.70\times10^{-1}$	0.887
		-5	-180.0 … -35.5	$3.52\times10^{-10}T^4+4.45\times10^{-8}T^3-2.96\times10^{-5}T^2-8.06\times10^{-3}T+3.01\times10^{-1}$	0.994
			-35.5 … -20.9	$-4.41\times10^{-4}T^2-3.90\times10^{-2}T-2.79\times10^{-1}$	0.988
			-20.9 … 0.0	$9.07\times10^{-4}T+3.61\times10^{-1}$	0.898
		-50	-131.2 … -117.5	0.47†	-
	EC	-1	-82.8 … -29.8	$-1.44\times10^{-7}T^4-3.68\times10^{-5}T^3-3.46\times10^{-3}T^2-1.46\times10^{-1}T-1.81$	0.998
			-29.8 … 0.0	$-1.23\times10^{-5}T^2-1.47\times10^{-4}T+3.43\times10^{-1}$	0.483
		-2.5	-180.0 … -118.9	$5.85\times10^{-4}T+4.32\times10^{-1}$	0.909
			-86.7 … -67.8	$7.29\times10^{-4}T+4.07\times10^{-1}$	0.714
			-50.2 … -27.6	$-1.86\times10^{-6}T^4-3.23\times10^{-4}T^3-2.08\times10^{-2}T^2-5.99\times10^{-1}T-6.06$	0.998
			-27.6 … 0.0	$-6.17\times10^{-6}T^2-1.20\times10^{-3}T+2.95\times10^{-1}$	0.763
		-5	-180.0 … -117.7	$4.74\times10^{-4}T+4.19\times10^{-1}$	0.979
			-85.3 … -70.3	0.3440†	-
			-52.3 … -26.6	$1.24\times10^{-6}T^4+1.83\times10^{-4}T^3+9.50\times10^{-3}T^2+1.94\times10^{-1}T+1.57$	0.989
			-26.6 … 0.0	$-7.22\times10^{-5}T^2-2.97\times10^{-3}T+2.83\times10^{-1}$	0.970
		-50	-129.8 … -117.1	0.34†	-
			-88.6 … -75.2	0.33†	-
			-54.2 … -27.3	$-1.33\times10^{-7}T^4-3.92\times10^{-5}T^3-3.73\times10^{-3}T^2-1.51\times10^{-1}T-1.72$	0.996
			-26.7 … 0.0	$-6.77\times10^{-5}T^2-3.06\times10^{-3}T+2.81\times10^{-1}$	0.986

Note in Fig. 3.3 a data gap around -100 °C to -80 °C, which is associated with transitioning from passive to active rewarming during experimentation [14]. Due to overshooting of the temperature control system of the cooling chamber, the certainty in thermal conductivity measurements within this range is unknown and the corresponding data are omitted. In several experiments at the higher cooling rates (H_1 = 50 °C/min) the hot-wire sensor was damaged above -100 °C due to residual stress formed during cooling. Hence, data are missing from those experiments in Figs. 3.3 and 3.4, and Table 3.2 at higher temperatures. Based on cryomacroscopy video analysis, vitrification occurred in all experiments where a SIM was added to the DP6, regardless of the SIM type; the vitrified material appears transparent while the crystalline material appears opaque [14]. This observation is consistent with the relatively low thermal conductivity characteristic of amorphous materials that is shown in Fig. 3.3. By contrast, in the absence of SIMs, DP6 in pure water crystallized at cooling rates below the critical value for vitrification, which is 40 °C/min for DP6 [30]. This observation is consistent with the relatively high thermal conductivity displayed in Fig. 3.3, which is characteristic of crystalline solids. It can further be seen from Fig. 3.3 that, in general, the thermal conductivity of the vitrified material decreases with the decreasing temperature, while the thermal conductivity of the crystalline material increases with the decreasing temperature. At much lower temperatures, the trend for crystalline materials is expected to reverse due to the decreasing population of energy carriers (i.e., phonons), but this is out of the range for current cryobiology applications. Disordered materials, such as a vitrified CPA, tend to have thermal conductivity values that are orders of magnitude lower than their crystalline counterparts, with dramatic effects on heat transfer analyses [57]. This difference is associated with the long-range order present in crystalline materials, which enables efficient thermal transport by phonons that arise from cooperative vibration of the molecules in the lattice. By comparison, disordered materials are poor transmitters of thermal energy due to the resulting uncorrelated vibrations [7,8].

3.3.1 Rewarming Phase Crystallization (RPC)

Cryomacroscope video recording and analysis of experimental data can help in identifying crystallization events, but cannot be used to quantify the extent of crystallization. For example, when DP6 is cooled at 50 °C/min, it shows a lower thermal conductivity than when it is cooled at 5 °C/min (Fig. 3.3), which suggests a reduced portion of crystals, or reduced grain sizes, in the

domain with the increased cooling rate. However, Fig. 3.3 also shows up to 10% higher thermal conductivity for DP6 cooled at 5 °C/min than 2.5 °C/min, which is counter-intuitive and represents the exception when compared with other solutions tested. The reason for this inverted difference is unknown but it can be the result of more favorable conditions to crystallization unrelated to the thermal history, such as dissolved gases or other nucleators. Either way, this is an indirect indication of the statistical nature of the onset and progression of crystallization in those non-equilibrium conditions. Note that the critical cooling rate reported in the literature is based on differential scanning calorimetric (DSC) studies, which use microliter-size samples, while the current data is generated for milliliter-size samples, and it is possible that the tendency to crystallize also increases with the sample size [3], [40] and [81].

In particular for DP6 in the absence of SIMs subject to a cooling rate of 50 °C/min, it can be seen from Fig. 3.3 that the thermal conductivity gradually increases with temperature between −100 °C and about −70 °C, but then exhibits a rapid increase up to about −55 °C, followed by decreasing thermal conductivity representative of a crystalline material. This effect is associated with the phenomenon of RPC, which is an inclusive term combining crystal growth from nuclei already developed during cooling (also known as recrystallization) and crystal formation during rewarming (also known as devitrification). In general, RPC occurs when the viscosity of the material decreases with increasing temperature, while the material is still unstable below its heterogeneous nucleation temperature (about −35 °C for DMSO at a similar concentration for reference [61]; not fully characterized for DP6) [30]. Given the much lower thermal conductivity values of DP6 when mixed with SIMs and cooled at 50 °C/min, it is concluded that DP6 in the absence of SIMs already contains a significant portion of crystals from the cooling phase of the cryogenic protocol, and the related observed effect during rewarming is recrystallization.

3.3.2 Vehicle Solution Effects on DP6 Vitrification in the Absence of SIMs

It can be seen from Fig. 3.3 that DP6+EC behaves differently than DP6 in pure water for the same cooling rates in terms of the effect of RPC on thermal conductivity. For example, DP6+EC cooled at 2.5 °C/min displays thermal conductivity of a vitrified material at the early stage of rewarming, up to about −65 °C, and then it displays the effect of RPC.

The EC solution is designed to maintain ionic and hydraulic balance in cells at cold temperatures [71]. In particular, EC incorporates 0.194 M glucose which is a known glass promoting agent but in a very low concentration compared with the overall 6 M concentration of DP6. This observation is of significance in the design of cryopreservation solutions, as the effects of vehicle solutions on the likelihood of vitrification may be overlooked.

Fig. 3.5 displays the combined effects of cooling rate and the presence of EC on thermal conductivity at a temperature of −121 °C (2 °C below the glass transition temperature for DP6). For DP6 in the absence of EC and SIMs, the thermal conductivity decreases by 56% when the cooling rate is increased from 5 °C/min to 50 °C/min. For the case of DP6 with EC, thermal conductivity only decreases by 6% between the same cooling rates. Also note that the absolute value of thermal conductivity of DP6+EC is almost the same as that of DP6+SIMs, Fig. 3.3. Clearly, EC plays a significant role in glass promotion and its effect on thermal conductivity.

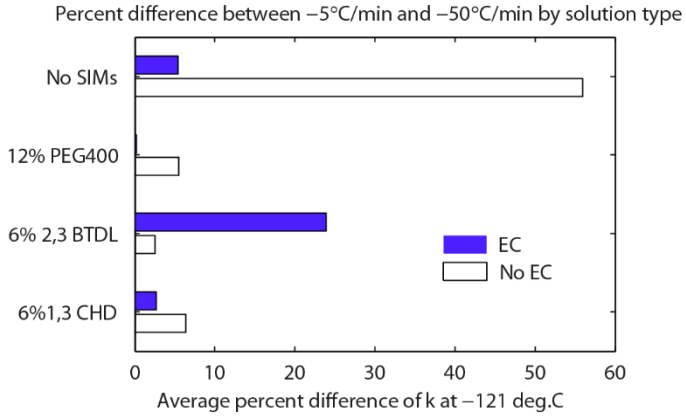

Figure 3.5: Average difference in thermal conductivity measurements between a cooling rate of 5 °C/min and 50 °C/min at −121 °C, two degrees below the glass transition temperature of −119 °C *[30]*.

3.3.3 The Effects of SIMs on DP6 Vitrification

The monotonic decrease in thermal conductivity with the decreasing temperature, highlighted as a gray band in Fig. 3.3, is a hallmark of amorphous materials (e.g., PMMA, glycerol). Although all DP6 solutions with SIM components have vitrified, resulting in a narrow range of thermal conductivity values over the temperature range studied, the thermal history for each cocktail can provide further insight on the process, as displayed in Fig. 3.4.

Note that solute precipitation from DP6+SIMs in EC has been reported recently [59], which affected opacity of the vitrified material, but did not affect the likelihood of crystallization or fracturing. The current study suggests that the thermal conductivity is not affected by solute precipitation at cryogenic temperatures as well. However, a very moderate effect of EC on thermal conductivity has been observed above the heterogeneous nucleation temperature (above about −35 °C), which may be related to molecular mobility when the viscosity of the material is relatively low. At 0 °C for example, an average lower thermal conductivity of 11% and 7% was measured for DP6+PEG400+EC and DP6+13CHD+EC, when compared with the same cocktails in the absence of EC.

For DP6+23BD, Fig. 3.4, a noticeable effect in thermal conductivity can be observed in the temperature range between −62 °C and −31 °C, with a maximum value at −45 °C. This increase in thermal conductivity is likely to be the result of RPC and the apparent increase in thermal conductivity value may be a computational artifact using Eq. (2.3) within the same temperature range, rather than being an intrinsic property of the material. Note that once crystallization initiates, the thermal history in the specimen may be altered by the energy required for crystal nucleation and growth, which increases the uncertainty in applying the solution presented by Eq. (2.3). For example, heat is absorbed by the phase change process at a constant temperature and as a result the hot-wire interpretation is enhanced thermal conductivity. Even a very mild RPC would be picked up by the sensitive experimental system for thermal conductivity measurements used in this study. As pointed out above, the extent of vitrification can be measured with DSC, which is the subject matter of a parallel study. For DP6+23BD+EC, such RPC artifacts are not observed. This suggests that EC has played a part in suppression of RPC.

It can be concluded from the results presented in Fig. 3.4 that DP6+PEG400 is the best glass promoting cocktail and DP6+23BD is the worst out of the selection tested, except when used with EC. While RPC could have been avoided by increasing the rewarming rates, the corresponding values are above the range of the testing capabilities of the current system. For future thermal analyses, given the functional behavior of thermal conductivity with temperature, one can linearly interpolate the thermal conductivity within the RPC range by using its boundary values.

A very moderate effect of the cooling rate of DP6+SIM on its thermal conductivity can be observed from Fig. 3.5, within the tested range, measured in only a few percent. This difference

suggests that each cocktail is mostly vitrified, which may greatly simplify future computational cryobiology studies. It is also a reminder that the SIMs are not necessarily added to prevent ice nucleation but to further suppress ice growth.

3.4 Conclusions

In this chapter, the thermal conductivity of DP6 in combination with SIMs and EC has been measured, using a transient hot-wire method and the new experimental setup presented in Chapter 2. Results of this study demonstrate that the thermal conductivity may vary by three fold between the amorphous and crystalline phases of DP6 below the glass transition temperature. However, the current experimental setup does not permit the quantification of the extent of crystallization in terms of volume ratio. Results of this study further demonstrate the ability of SIMs to decrease the extent of crystallization in DP6, even at subcritical cooling and rewarming rates. Finally, results of this study demonstrate an additional ice suppression capability of EC, which may be disproportionate to its volume ratio in the cocktail.

The implications of the observed thermal conductivity differences between the amorphous and crystalline phases of the same CPA cocktail on cryopreservation simulations is significant. In broad terms, the lower thermal conductivity in the amorphous state creates less favorable conditions to maintain the high cooling and rewarming rates at the center of large specimens, which are essential to ensure vitrification. In turn, when partial crystallization occurs within the specimen, the structural integrity of the material may be compromised due to differential thermal expansion between the crystallized and the amorphous regions. Hence, thermal conductivity data is not only critical for the prediction of the likelihood of vitrification, but also for the prediction of structural damage in cryopreservation protocols.

When SIMs are successfully applied, the thermal conductivity of the CPA+SIM cocktail is essentially the same as that of the vitrified CPA. The benefit for large-size cryopreservation is that the addition of SIMs lowers the critical cooling rates required for successful vitrification. Unfortunately, given the kinetics of ice crystallization and also the path-dependent nature of the cryopreservation process, it is difficult to predict a priori when significant crystallization will occur for a particular combination of CPA, SIMs, vehicle solution, and specific thermal history. Hence, characterization of thermal conductivity is most applicable if performed by mimicking the specific thermal history expected within a large specimen with the specific set compounds.

Chapter 4

Finite Elements Evaluation of Error in Thermal Conductivity Measurements by the Transient Hot-Wire Technique Due to Non-Uniform Temperature Field in Sample

4.1 Objective

The objective in this study is to investigate the limits of the device and method proposed for thermal conductivity measurements, which is described in Chapter 2 and demonstrated on selected cocktails in Chapter 2. This limitations are originated from non-uniform temperature distribution within the sample, perturbation in the cryomacroscope cooling chamber temperature, and limits of the electronic setup in cryogenic temperatures. This investigation is based on finite elements analysis (FEA).

4.2 System Limitations

The hot-wire technique revolves around the use of an immersed electrical resistor (platinum in the described experimental setup) which is used simultaneously as a heater and a sensor. A step-like activation in current generates Joule heating in the wire. Concurrently, measurements of its electrical resistance are used to extract its temperature, via the dependency of electrical resistance upon temperature. The thermal conductivity of the surrounding medium defines the wire's response. It is extracted from the slope of the measured thermal response of the wire with respect to the natural log of time (see eqn. 4.2). Two modifications to the traditional transient hot wire measurement have been made for specialized study of CPA during cryopreservation, which invalidate underlying assumptions in its mathematical formulation. They specifically invalidate the boundary condition that the sample domain in which the wire is submerged is initially at uniform temperature.

First, the scanning cryomacroscope is used in order to visually study effects of vitrification and crystallization occurring in the CPA medium during cryopreservation. The use of the cryomacroscope constrains the hot wire sensor and the CPA medium to a 12.5 mm by 12.5 mm by 45 mm cuvette, chosen for optical clarity. Thus, the straight shape of the wire is changed to a 75 mm long "U" shape, to conform to the constraints posed by the cuvette. This also allows the wire sensor to be sufficiently long so as to eliminate axial heat loss error. Second, thermal conductivity

measurements are made during systematic rewarming of the contents of the cooling chamber. The chamber includes the cuvette, the cuvette cap on which the hot wire sensor is mounted, the hot wire sensor itself, and the CPA domain. An adjustment is made to the slope of the measured thermal response of the wire during a thermal conductivity measurement by subtracting from it the slope of the average temperature rise of the system from rewarming.

The concern associated with these two modifications is that the temperature along the wire may vary significantly during measurements due to the placement and distribution of the wire in the cuvette in space. A non-uniform temperature field is formed in the sample solution while rewarming. This may add a significant uncertainty to measurements by skewing the ΔT versus ln t curve from which thermal conductivity is extracted (see Chapter 2). The transient temperature change, or resistance change, is measured along the entire wire and represents an average value, which may or may not encompass a large temperature non-uniformity along the wire. It is not possible to measure such a temperature non-uniformity experimentally. The consequences of these modifications to experiments are studied herein with the use of a finite elements analysis (FEA) model. My aim is to model the heat transfer processes in the cuvette, CPA, and along the heated wire to quantify how large the temperature variation is along the wire during experiments, and to determine whether or not the variation will distort the thermal conductivity measurements significantly. The unique contributions presented here are (i) verification of the functionality of the transient hot wire technique under non-isothermal conditions, and (ii) investigation of the limits of the transient hot wire technique in cryomacroscopy for non-isothermal conditions (to be completed in the future).

4.3 Mathematical Formulation

In the original transient hot-wire technique, a long thin platinum wire is submerged in a material for which thermal conductivity is to be characterized. At time $t = t_0$, a Heaviside function is generated by a current source attached to the leads of the wire and causes Joule heating in the platinum until the current source is switched off at time $t = t_{end}$, where the total time of heating $\tau = t_{end} - t_0$. Simultaneously, a digital multimeter measures the changing resistance of the wire ΔR. The resistance signal ΔR is linearly related to the temperature rise of the wire due to self-heating:

$$\Delta T = \frac{\Delta R}{\beta R_{ref}} \tag{4.1}$$

where β is the coefficient of thermal resistance, and R_{ref} is the wire's resistance taken at the temperature at which β is referenced. The thermal conductivity of the surrounding medium can be found by fitting the temperature response data with a simplified solution to the heat diffusion equation of an ideal line heater submerged in an infinite medium, yielding:

$$k_{sample} = \frac{q/4\pi}{d(\Delta T)/d(\ln t)} \tag{4.2}$$

where q is the heat generation rate per unit length of wire and t is heating time. Although the quantity measured in experiments is $\Delta R_{\tau, avg}$, the following discussion will be concerned with $\Delta T_{\tau, avg}$ where $\Delta T_{\tau, avg}$ is related to $\Delta R_{\tau, avg}$ as expressed by equation 4.1. Due to the linear relationship between $\Delta R_{\tau, avg}$ and $\Delta T_{\tau, avg}$, the same analyses extend to $\Delta R_{\tau, avg}$.

4.3.1 Modification to Hot Wire Geometry for Cryomacroscopy

The scanning cryomacroscope device used in the present thermal conductivity measurements has been designed to visually study macroscopic effects in cryopreserved materials in-situ. The cryomacroscope and sample are contained in the cooler, Kryo 10-16, which is controlled by Kryo-10-20 (Planer Ltd., UK). Temperature control is maintained by the controlled release of liquid nitrogen vapors into a stream of heated air. The efficacy of the cryomacroscope is maximized when samples are contained in a 4.5 mL cuvette, chosen for optical clarity. The specific dimensions of the cuvette are 12.5 mm by 12.5 mm by 45 mm, in which the sample and the sensor are contained, shown in Fig.4.1a.

In the ideal transient hot wire problem the solution specified is for an infinitely long heater embedded in an unbounded medium. The axial heat loss error associated with a finite heater is inversely dependent on the ratio of the wire's length to its diameter [37]. Due to the geometric constraint posed by the cuvette, a straight hot wire sensor placed in this container could not be longer than 40 mm, which is not long enough to keep the axial heat loss error within a few percent [37], based on the thermophysical properties of the CPA and platinum. This error is reduced by mounting the hot wire sensor in a "U" shape on the ABS printed cap shown in Fig. 4.1a, with a nearly doubled length of 70 mm.

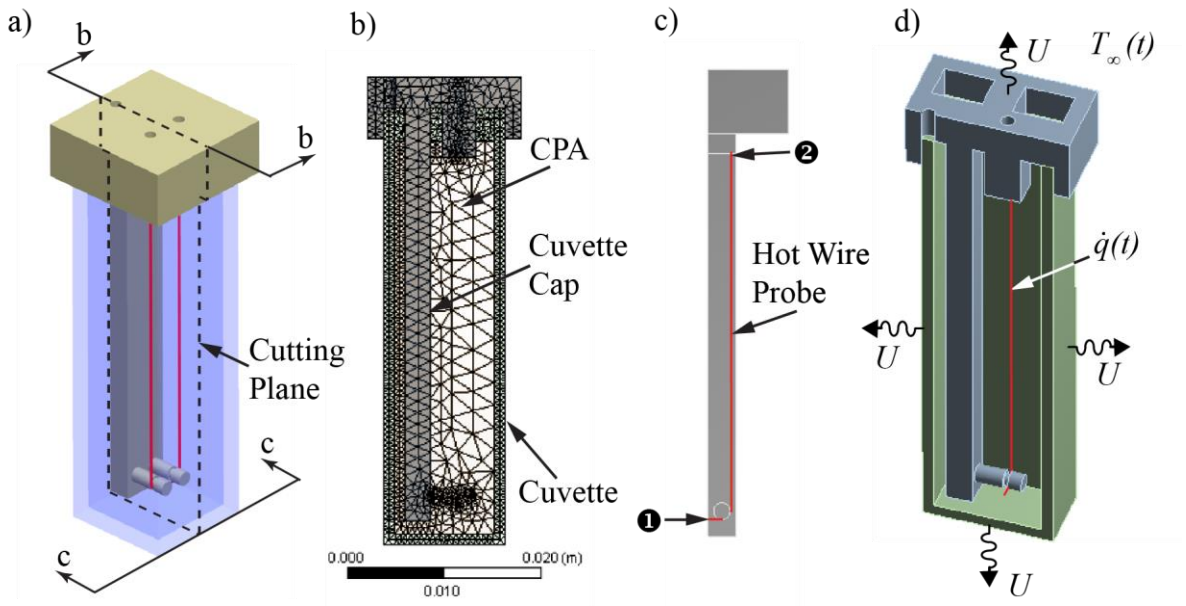

Figure 4.1: Schematic illustration of: (a) the CPA, cuvette, and cuvette cap, shown with cutting plane used to simplify finite elements analysis and description of section views, (b) its finite elements (ANSYS) representation; (c) front view of the cuvette cap, the mounted hot wire probe and the path mapped from ❶ to ❷ for the below analysis; (d) the heat transfer processes within the model, where T_∞ is the free stream temperature in the cooling chamber recorded during experiments and is imposed as the free stream temperature in the model, $\dot{q}(t)$ is the time-dependent volumetric heat generation in the wire, and U is the convection coefficient from the outer surfaces of the cuvette and cuvette cap to the surroundings

4.3.2 Modification to Hot Wire Measurements Made During Rewarming

Thermal conductivity measurements are made every 35 seconds in the sample during slow (3°C/min) rewarming of the entire system from -180°C to 20°C. The benefit of making measurements continuously throughout the rewarming process is that a large amount of thermal conductivity data can be acquired over the temperature range without the slow requirement of reaching thermal equilibrium throughout the sample before every measurement. In this analysis, the temperature change occurring as a result of rewarming is subtracted from the temperature change associated with the heating of the wire, which shifts the slope of ΔT vs ln t to yield the correct thermal conductivity. More details, as well as benchmark measurements supporting this modification, are presented in Chapter 2.

4.3.3 Heat Transfer Problem

The problem to be modeled using finite element analysis in ANSYS is of a CPA contained in a cuvette which is heated by forced convection on all external surfaces and by natural convection on the top internal surface of the CPA. A hot wire probe is submerged in the CPA and generates heat volumetrically for a period of time, τ, starting at t_0 and ending at t_{end}. Conduction heat transfer in the CPA, cuvette, cuvette cap, and wire probe can be modeled by the transient heat diffusion equation in 3-D:

$$\rho_i c_{p,i} \frac{\partial T_i}{\partial t} = \nabla(k_i \nabla T_i) + \dot{q}_i(t) \tag{4.3}$$

where ρ is the temperature-dependent density, c_p is the temperature-dependent specific heat, T is temperature, t is time, k is the temperature-dependent thermal conductivity (except in the case of ABS where all properties are assumed to be constant with T), and $\dot{q}$ is volumetric heat generation in subdomain i, where i stands for either CPA, cuvette, cuvette cap, or wire probe.

The internal boundary conditions between all contacting bodies are assumed to be continuous in temperature and heat flux, with no contact resistance. Contacting pairs include the hot wire probe and the CPA, the hot wire probe and the cuvette cap, the cuvette cap and the CPA, the CPA and the cuvette, as shown in Fig. 4.1a-d. The geometric model was cut in half before performing the transient thermal analysis because it is bilaterally symmetric about the cutting plane shown in Fig. 4.1a. An adiabatic boundary condition is imposed on all surfaces along the cutting plane. The heat transfer at all external boundaries of the cuvette and cuvette cap can be described as:

$$-k_i \frac{\partial T_i}{\partial \hat{n}} = U(T_i - T_\infty) \tag{4.4}$$

where $\hat{n}$ is the direction normal to the outer wall, T_∞ is the time-dependent temperature of the cooling chamber input from experimental measurements (shown in Fig. 4.2), and U is overall convection coefficient, which encompasses all heat transfer effects including latent heat effects from boiling liquid nitrogen. Feig et. al. performed a parametric estimation of the overall convection coefficient in the cooling chamber used in the experimental apparatus and found it was $U = 346 \pm 24 \frac{W}{m^2 - °C}$ [32]. The free convection coefficient on the top internal surface of the CPA

is assumed to be $10\frac{W}{m^2-°C}$ [32,42]. A schematic of the heat transfer process is shown in Fig. 4.1d.

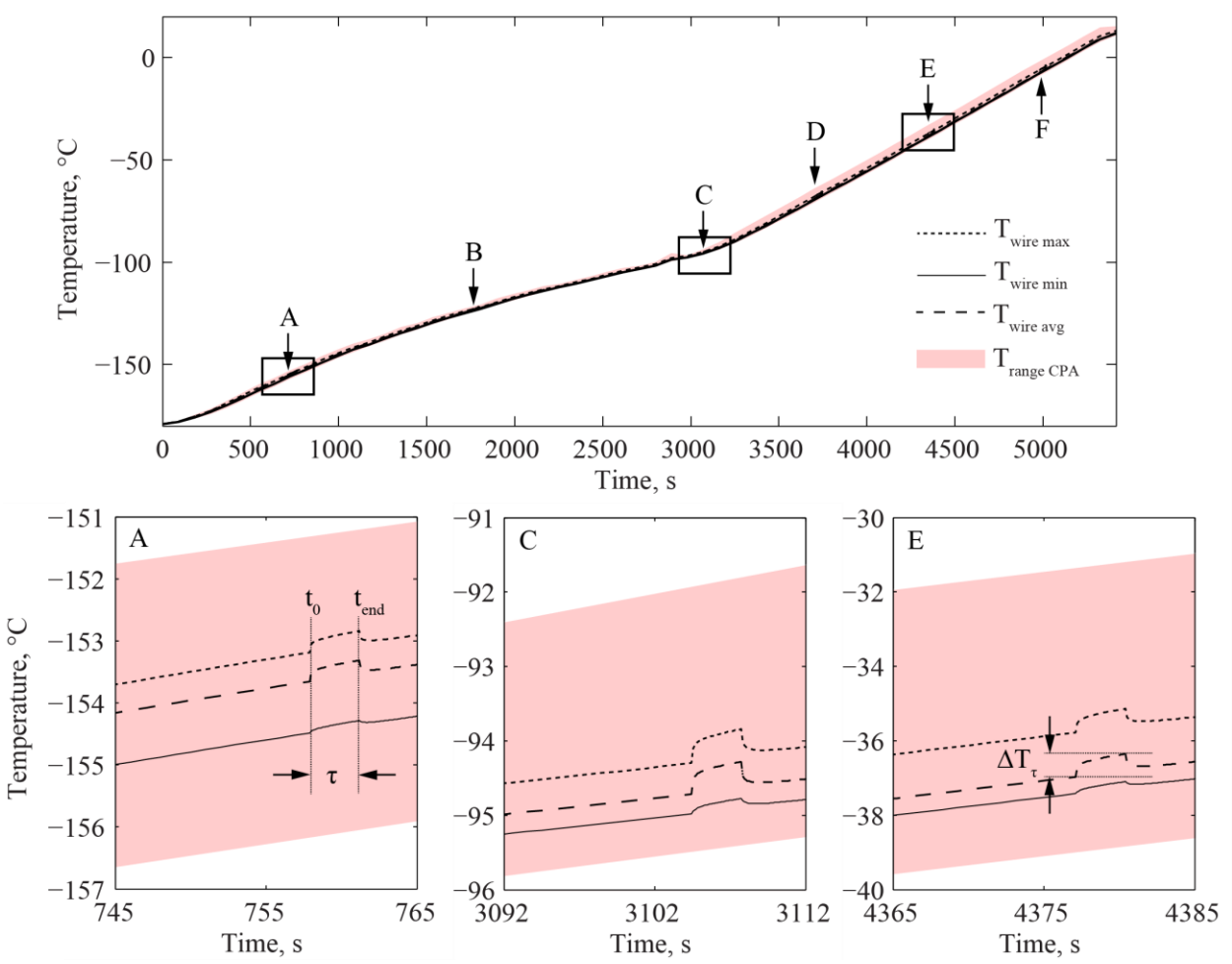

Figure 4.2: Temperature versus time during master simulation (top) and during transient hot wire heating cycle simulations A, C, E (shown left to right). Heating cycles investigated are labeled A, B, C, D, E, F and are further discussed in text. Temperatures of interest include the temperature range of the CPA domain, hot wire maximum, minimum, and average. Also shown are τ (period of time between heating end time, t_{end} and heating start time, t_0) and temperature change of the wire over τ, ΔT_τ

Volumetric heat generation in the wire, $\dot{q}_{wire\ probe}$, increases during each heating period as a result of the increasing resistance of the wire as it heats up. Although this increase is by less than 0.3%, it is still accounted for in the model. Volumetric heat generation ranges from 2.32×10^8 W/m^3 at the beginning of cycle A (referring to Fig. 4.2, about -150°C) to 6.58×10^8 W/m^3 at the end of

cycle F (referring to Fig. 2, about 0°C*).* Properties ρ, c_p, and *k* are shown in table 4.1 for each respective domain, where linear interpolation between points is done automatically by ANSYS. All quantities were previously measured and reported in literature [14,32,33,35,36,47,54,55,62,67,74,83] with the exception of specific heat capacity of 7.05 M DMSO, which was extrapolated from the literature by Feig et. al [32].

Table 4.1: Material properties used for ANSYS thermal transient analysis (temperature is in °C)

Material	Property	Value
7.05 M DMSO	ρ, Density, kg/m^3	$1058-0.41T$ [62]
	c_p, Specific Heat, $\mathrm{J}/\mathrm{kg}-°\mathrm{C}$	$2804+4.205T-0.054T^2-4.902\times10^{-5}T^3$ [32]
	k, Thermal Conductivity, $\mathrm{W}/\mathrm{m}-°\mathrm{C}$	$3.56\times10^{-1}+7.42\times10^{-4}T-1.29\times10^{-6}T^2-6.87\times10^{-8}T^3-2.95\times10^{-10}T^4$ [14]
Polystyrene Cuvette	ρ, Density, kg/m^3	$1055-0.26T$ [55]
	c_p, Specific Heat, $\mathrm{J}/\mathrm{kg}-°\mathrm{C}$	$1121+3.94T$ [36]
	k, Thermal Conductivity, $\mathrm{W}/\mathrm{m}-°\mathrm{C}$	$0.14+1.3\times10^{-4}T$ [83]
ABS Cuvette Cap	ρ, Density, kg/m^3	1045 [47]
	c_p, Specific Heat, $\mathrm{J}/\mathrm{kg}-°\mathrm{C}$	1470 [54]
	k, Thermal Conductivity, $\mathrm{W}/\mathrm{m}-°\mathrm{C}$	0.17 [74]
Platinum Wire	ρ, Density, kg/m^3	21370 [33]
	c_p, Specific Heat, $\mathrm{J}/\mathrm{kg}-°\mathrm{C}$	$c_p=\begin{cases}100.22 & T=-173.15\\117.18 & T=-123.15\\125.08 & T=-73.15\\129.74 & T=-23.15\\131.38 & T=0\end{cases}$ [35]

4.3.4 FEA Simulation

The heat transfer process described above was simulated using the FEA software ANSYS transient-thermal solver. The geometry of the cuvette body was measured using a digital caliper and drawn in Solidworks. The Solidworks drawing used to 3-D print the cuvette cap was integrated with the cuvette body. The cross-section of the wire probe was made to be a square instead of a circle to simplify meshing but the cross-sectional area, and thus volume, was retained.

Figure 4.1b shows the ANSYS mesh rendering of the CPA, cuvette, and cuvette cap. The wire probe is not shown in this rendering, but its geometry can be more clearly seen in Figs. 4.1c and 4.1d. Tetrahedral elements were used to mesh the CPA, cuvette, and cuvette cap due to their complex geometries, and hexahedral elements were used to mesh the wire probe. Program controlled inflation was used in generating the mesh in the CPA surrounding the wire probe to get a finer resolution of the temperature field. The elements totaled 174,772, which satisfied a mesh convergence analysis for the thermal solution.

The heat transfer process in the CPA without internal heat generation in the wire probe was simulated during the entire rewarming period from -179°C to 15°C, about 5415 seconds, with a time step size of 90 s. The system is not expected to increase in temperature by more than 5°C in a 90 second time period based on T_∞. This master simulation was used to find the temperature field in the system at specific times during rewarming so that individual THW measurements could be investigated, but since THW effects were not present in this simulation, the temperature changes in the CPA and wire due to the transient hot wire measurements ($\Delta T_{CPA\text{-}THW}$) were equal to zero. The temperature changes in the CPA and wire due to chamber rewarming ($\Delta T_{CPA\text{-}CR}$) were not equal to zero. Six transient hot wire measurements A, B, C, D, E, and F were chosen as representative cases from evenly spaced temperature intervals along the rewarming curve, as shown in Fig.4.2. Each of these measurements was run as a separate simulation, with $\dot{q}_{wire\ probe}$ taken from experimental values and the initial temperature fields imported from the master simulation at the appropriate times ($\Delta T_{CPA\text{-}THW} \neq 0$, $\Delta T_{CPA\text{-}CR} \neq 0$). Six companion simulations A_2, B_2, C_2, D_2, E_2, and F_2 were run as a supplement to each of the simulations A-F, where the initial temperatures of the systems were uniform (-150°C, -120°C, -90°C, -60°C, -30°C, and 0°C) and no convection boundary conditions were imposed ($\Delta T_{CPA\text{-}THW} \neq 0$, $\Delta T_{CPA\text{-}CR} = 0$). These companion simulations represent the transient hot wire experiment without the modifications that prompted this investigation, and they served as a basis of comparison for analysis, as discussed below.

For heating cycles A-F, the simulations start 35 seconds before t_0 with a time step size of $\delta t_0 = 1$ s. Starting at t_0, the time step size decreases to $\delta t_1 = 0.1$ s. To test for convergence, δt_1 was decreased to 0.05 s and again to 0.025 s. The temperature rise of the wire at t_{end}, ΔT_τ, when averaged over the length of the wire, changed by 0.5% between $\delta t_1 = 0.1$s and $\delta t_1 = 0.05$s and by 0.016% between $\delta t_1 = 0.05$s and $\delta t_1 = 0.025$s. Hence $\delta t_1 = 0.1$s is a satisfactory time step size.

4.4 Results and Discussion

Maximum, minimum, and average temperature vs. time curves for the wire probe over the course of rewarming are shown in Fig. 4.2, where Cycles A (approximately -150°C), C (approximately -90°C), and E (approximately -30°C) are shown in detail. The temperature range of the CPA domain is also shown as the shaded region. In the case of cycle E, the temperature ranges over 6.1°C in the CPA during heating, and the temperature ranges over 1.4°C in the wire before heating. This difference is significantly greater than $\Delta T_{\tau, avg}$, justifying the need for further analysis.

Fig. 4.3a shows the temperature distribution along the wire path for the representative case of cycle E before heating at $t = t_0$ (blue) and after heating at $t = t_{end}$ (red). The maximum temperature is located just past point ❶, at the place where the wire is in contact with the ABS peg, which has a lower thermal conductivity than the CPA. Before heating, the average temperature is -36.5°C with a maximum temperature difference of 1.4°C and a standard deviation of 0.38°C. After heating, the average temperature is -35.9°C with a maximum temperature difference of 1.4°C and a standard deviation of 0.39°C. A visual inspection of Fig. 4.3a suggests that the temperature profiles are similar, with an offset in temperature. Fig. 4.3b shows their difference, ΔT_τ, which has an average value of 0.6°C and a standard deviation of 0.03°C (5%). Similar results were observed for the cases of cycles of A, B, C, D, and F, where $\Delta T_{\tau, avg}$ ranged from 0.3 to 0.7°C and the standard deviation of ΔT_τ comprised 4.8% of it on average. These results suggest that the non-uniform temperature profile along the wire retains a consistent shape during the measurement and that $\Delta T_{\tau, avg}$, the measured quantity, is representative of relative changes in T at most points along the wire during heating.

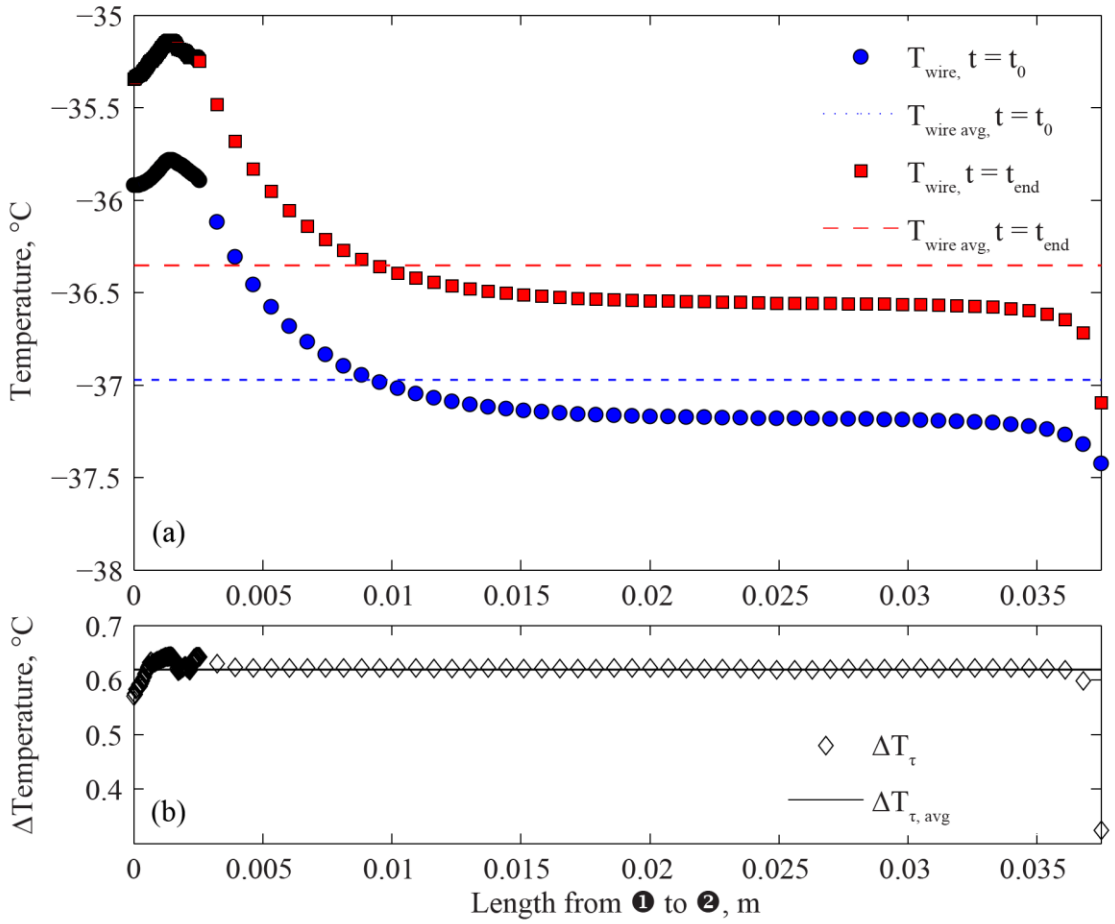

Figure 4.3: Plots of heating cycle E: a) temperature along wire length from ❶ to ❷ (referring to Fig. 4.1.c), where temperature and average temperature are shown at the start of heating ($t=t_0$) and at the end of heating ($t=t_{end}$), and b) change in temperature during heating along wire length from ❶ to ❷, where ΔT_τ is T_{wire}, $t=t_{end}$ minus T_{wire}, $t=t_0$, and standard deviation of ΔT_τ is 0.03°C

In experiments, as described in Chapter 2, a line is fit to T_{avg} in the time before t_0 to predict rewarming rate during measurements and the temperature rise associated with this rewarming rate is subtracted out of the temperature rise due to wire heating (see fig. 2.4 for clarification). The same can be done for cycle E, which yields a temperature rise of 0.61°C before and 0.46°C after this subtraction. The companion simulation of cycle E, cycle E_2, a simulation without convective boundary conditions and with uniform initial temperature of -30°C, requiring no adjustment to

temperature during wire heating (ΔT_{CPA}-CR = 0, ΔT_{CPA}-THW ≠ 0), yielded an average temperature rise of 0.44°C which represents a 4% difference compared to the original cycle E simulation.

Thermal conductivity was extracted from the slope of a line of best fit of T_{avg} curves as is done in experiments, and then compared to the thermal conductivity assigned to the CPA in the simulation for proof of accuracy. Thermal conductivity was found to be 0.322 W/m-K for cycle E and 0.326 W/m-K for cycle E_2. The value used in the simulation was 0.335 W/m-K, a 4% difference from the value extrapolated from the cycle E simulation. It is probable that the measured thermal conductivity in both cases is systematically lower than the actual value due to the presence and influence of the low thermal conductivity ABS peg about which the wire contacts at the bottom of the "U". However, this difference falls within the experimental uncertainty. This shows that even if the hot wire has some temperature distribution along it, accuracy is not significantly compromised unless parts of it are changing temperatures at different rates during the time period τ. The certainty of the temperature to which the thermal conductivity measurement is associated may be affected in proportion to the magnitude of the temperature variation along the wire. As previously mentioned, the standard deviation about the average temperature for the wire in cycle E at time $t = t_0$ is 0.38°C and the maximum variation is 1.4°C, where experimental uncertainty in temperature is 0.5°C [14]. The uncertainty brought about by the non-uniform temperature along the wire is not expected to affect measurements of vitrified CPA, whose thermal conductivity does not vary significantly with temperature. The solutions most affected by the uncertainty are those with a large $\frac{dk}{dT}$, which are materials in their phase change region. For example, $\frac{dk}{dT}$ = -0.0951 W/m-K^2 for 2M DMSO at -9.4°C. Thus, the uncertainty in the thermal conductivity added to the measurement at this temperature may be as high as 0.07 W/m-K, which is 6.2% of the 1.12 W/m-K measurement. At -0.2°C, $\frac{dk}{dT}$ = -0.07 W/m-K^2, and uncertainty added to the measurement becomes 0.05 W/m-K, which is 8.1% of the 0.62 W/m-K measurement, the worst case scenario.

4.5 Conclusions

An FEA of the heat transfer process was performed with ANSYS to simulate the conditions of an experimental transient hot wire thermal conductivity measurement. In experiments, thermal conductivity measurements of CPAs are made with the transient hot wire technique in conjunction

with the scanning cryomacroscope. Measurements are made during rewarming, where a non-uniform temperature distribution exists in the CPA domain. This non-uniform temperature distribution invalidates a boundary condition in the mathematical formulation of the transient hot wire problem. A modification is made to the analysis to account for the changing temperature of the wire as the CPA domain warms up, but the temperature variation along the wire itself has the potential to be large. This can potentially skew the slope of the temperature response curve of the wire probe from which thermal conductivity is extracted, and is what prompted the FEA.

The temperature profile along the wire probe is found to span a range more than double the size of the $\Delta T_{\tau,\,avg}$ signal itself, where the maximum temperature variation along the wire is 1.4 °C and $\Delta T_{\tau,\,avg}$ = 0.6 °C. However, the temperature profile along the wire retains a consistent shape during the measurement, where the standard deviation of $\Delta T_{\tau,\,avg}$ is 5% of its value. This indicates that the temperature distribution along the wire is changing at a uniform rate, and $\Delta T_{\tau,\,avg}$ is representative of relative changes in T at most points along the wire during heating. The resulting thermal conductivity measurements differed by 4% from the assigned values and fell within experimental uncertainty of 10% under the conditions of the experiment.

Chapter 5

Thermal Analyses of a Human Kidney and a Rabbit Kidney During Cryopreservation by Vitrification

5.1 Objective

The objective for the current study is to investigate the thermal conditions leading to cryopreservation by vitrification in a kidney model. This study relies on thermal conductivity data presented in the previous chapters, and literature data for other relevant thermophysical properties. This study focuses of the cooling portion of the cryogenic protocol, from tissue loading with the CPA to cryogenic storage. Heat transfer simulations of vitrification are performed with the commercial FEA code ANSYS. The unique contributions presented here are (i) thermal analysis of a rabbit kidney undergoing cryopreservation by vitrification based on an established experimental protocol by Fahy et al [26], and (ii) investigating scale-up thermal effects on a 21-fold larger system containing a human kidney.

5.2 Materials and Methods

5.2.1 Physical Model

A geometrical model of a human kidney was downloaded from the NIH 3D Print Exchange [86]. This model is based on computed tomography (CT) imaging, which was further made water tight for FEA simulations in this study. The kidney model was scaled to have a volume of 209 ml, which is average for an adult human male [9].

Figure 5.1a displays a realistic illustration of a human kidney in a cylindrical CPA container. Figure 5.1b displays a schematic illustration of a cross section of the system, highlighting its four subdomains: renal medulla, renal cortex, contained CPA, and container. While the cylindrical container geometry allows simplicity in simulations, it is also advantageous for generating a relatively uniform volumetric heating effect at the rewarming stage by applying a radiofrequency (RF) electrical field [19]. The overall volume of the container was selected to be practical for the chosen kidney size. The physical properties of the cylindrical container were selected to be similar to those of commercial cryobags, as listed in Table 5.1. Specifically, a cylindrical container having the following dimensions can contain a human kidney: an inner diameter of 8.9 cm, a height of

16.3 cm, and wall thickness of 1.1 mm. These dimensions permit complete immersion of the kidney down to 2.1 cm below the CPA level, while the container wall extends 3.5 cm above the CPA level for handling purposes. The container is assumed to be uncovered during cooling, exposing the surface of the CPA to the same forced convection cooling conditions as the container walls and base. With this geometry, the container accommodates 581 ml of CPA in addition to the kidney volume. From thermal considerations, the portion of the wall extending above the CPA level bears negligibly on the analysis.

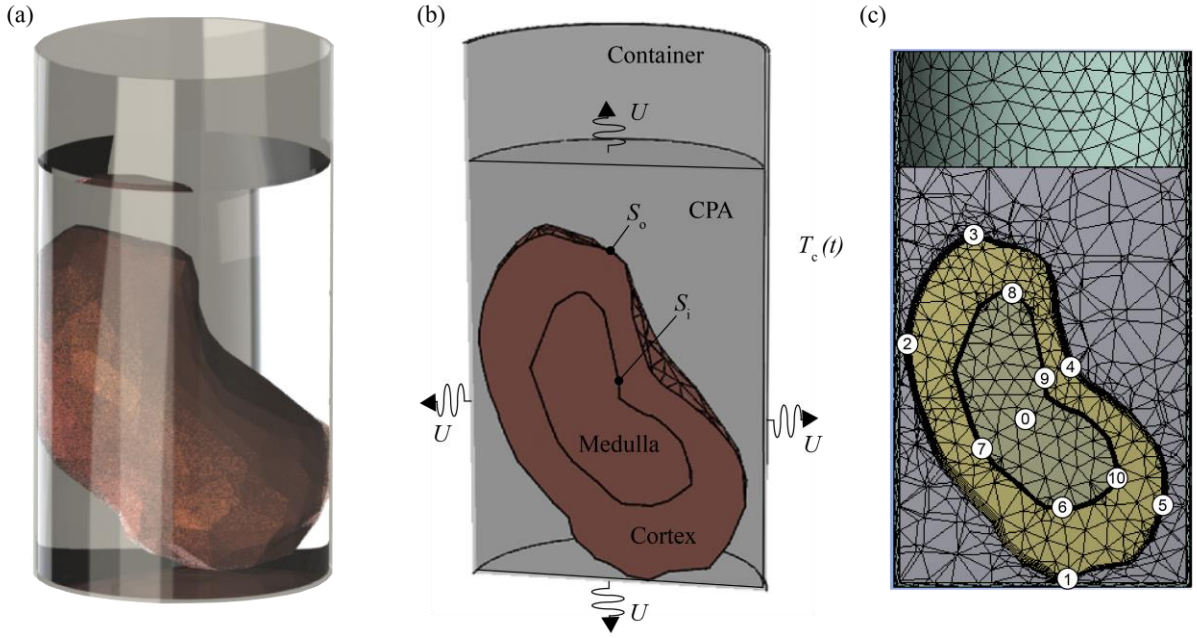

Figure 5.1: Illustrations of system analyzed in this study: (a) a kidney in a cylindrical container filled with CPA; (b) schematic view of the four subdomains of the system, each characterized by unique thermal properties; heat transfer processes and material properties of the constituents; (c) a cross section of the system showing the FEA mesh and virtual thermal sensors.

The geometrical model of the rabbit kidney is simply a scaled-down version of the human kidney to an overall volume of 9.8 ml, while maintaining geometric similarities with the human kidney. This target volume was selected to be compatible with a shortened Thermo Scientific Naglene 6250-9050 sample vial, used previously in unpublished rabbit kidney vitrification studies. The scaled-down container model had the following dimensions: an inner diameter of 3.2 cm, height of 5.9 cm, and a wall thickness of 0.4 mm. With this geometry, the container accommodates 27 ml of CPA in addition to the rabbit kidney volume.

Table 5.1: Material properties used in the current study, where temperature-dependent properties are presented in °C within the range of -22°C to -135°C

Material	Thermal Conductivity, k [W m^{-1} °C^{-1}]	Specific Heat, C_p [J kg^{-1} °C^{-1}]	Density, ρ [kg m^{-3}]
Fresh human kidney – cortex	0.503 [75]	3941 **	1049 [12]
Fresh human kidney – medulla	0.503 [75]	3908 **	1044 [12]
Fresh rabbit kidney – cortex	0.465 … 0.490 (76.6% … 79.8% water) [43]	3772 **, ***	--
Fresh rabbit kidney – medulla	0.502 … 0.544 (82.0% … 86.0% water) [43]	3772 **, ***	--
Dry human kidney material*	0.260	2732 *, **, ***	--
M22	$0.316+7.13\times10^{-5}T-1.26\times10^{-5}T^2-1.47\times10^{-7}T^3-4.75\times10^{-10}T^4$ [15]	-	1080
7.05M DMSO	$0.356+7.42\times10^{-4}T-1.29\times10^{-6}T^2-6.87\times10^{-8}T^3-2.95\times10^{-10}T^4$ [14]	$2804+4.205T-0.054T^2-4.902T^3$ [32]	$1058-0.41T$ [62]
Ice	$2.22-1.0\times10^{-2}T+3.45\times10^{-5}T^2$ [34]	$2066+6.9T$ [34]	$917-0.11T$ [34]
Water at 4.4°C	0.575 [41]	4208 [41]	999.8 [41]
Low-density polyethylene – container	$0.14-1.3\times10^{-4}T$ [83]	$1121+3.94T$ [36]	$1055-0.26T$ [55]

* Compiled based on the effective medium theory (EMT) [76] using 80% water and 20% dry material

** Compiled from thermal conductivity and thermal diffusivity data [75] assuming overall density of 1000 kg/m^3

*** Average property for the entire kidney

5.2.2 Thermal History

The thermal history in this theoretical study follows successful experimental investigations on rabbit kidneys using the CPA cocktail M22 [27]. In this past work, bare kidneys that had been loaded with M22 solution by perfusion ending at a temperature of -22°C were placed in a Linde BF1 biological freezer for cooling by fan-driven cold vapor from injected liquid nitrogen. The measured thermal history from that experimental study [6] is replicated in the present simulation study. Unlike past experimental work, the present analysis includes a container, which is necessary for RF rewarming and future clinical application.

The thermal history of a complete organ vitrification experiment as modelled here includes seven key stages: (i) precooling the container and contained CPA down to -50°C; (ii) precooling of the kidney down to -22°C during M22 perfusion; (iii) dropping the precooled kidney into the precooled CPA container; (iv) cooling the container at a rapid rate down to the storage temperature of -135°C; (v) holding the entire system at the storage temperature for as long as needed; (vi) rewarming the system by means of RF energy up to -22°C; and (vii) washing out the M22 by perfusion and recovering the organ. The current study focuses on the cooling and storage portion of the protocol (including stages (iii), (iv), and thermal equilibration in stage (v)), with the cooling chamber thermal history marked with a dashed line as T_c in Fig. 5.2.

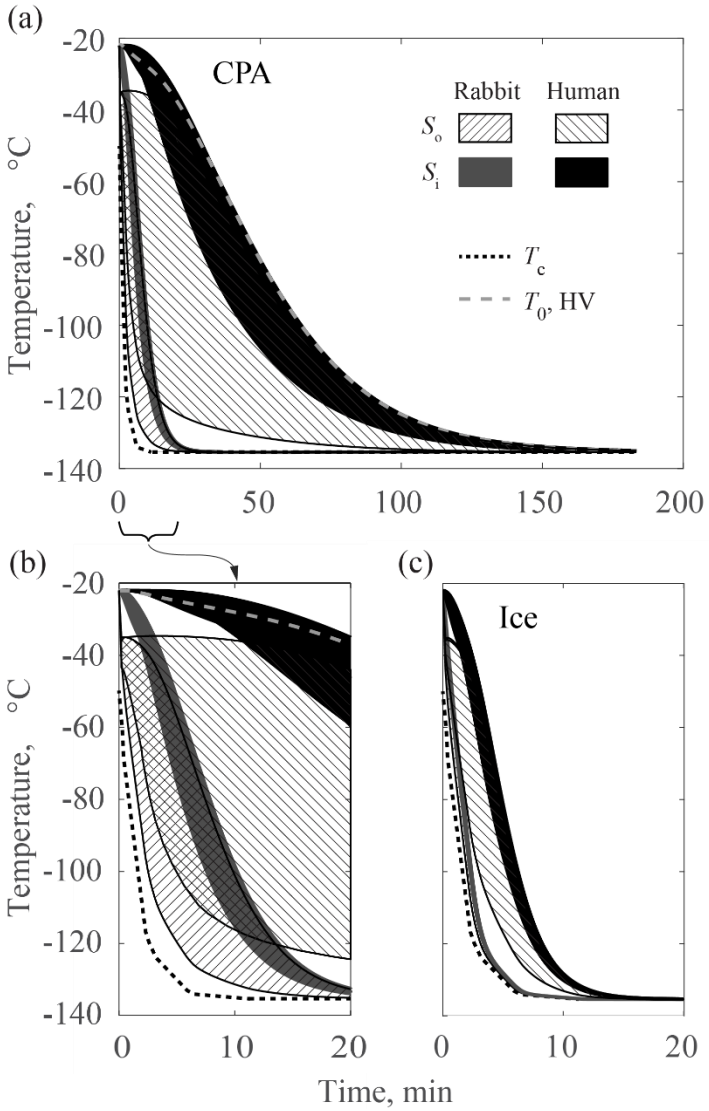

Figure 5.2: Thermal history in the kidney model for (a) a vitrified system with CPA properties, (b) the same system at the early stage of cooling, and (c) a vitrified system but with ice properties; where S_o is the outer surface of the cortex, S_i is the medulla-cortex interface, T_c is the temperature of the cooling chamber, and T_0 is the temperature at the center of the kidney (Fig. 5.1c).

During the cooling process, an overall heat transfer coefficient of 350 W/m^2-°C is assumed between the outer surfaces of the container and the cooling chamber temperature, as specified in Fig. 5.2. The same heat transfer coefficient is also assumed at the CPA air surface. Although measured in a different system, the above heat transfer coefficient value is assumed typical to a controlled-rate cooler, when the air inside the cooling chamber is well mixed [32].

5.2.3 Heat Transfer Model

Heat transfer within the organ-CPA-container system is assumed solely by conduction:

$$\rho_i C_{p,i} \frac{\partial T_i}{\partial t} = \nabla(k_i \nabla T_i) \tag{5.1}$$

where ρ is density, C_p is specific heat, T is temperature, t is time, k is thermal conductivity, and i is the subdomain index, standing for either the cortex, medulla, CPA, or container wall. Continuity in temperature and heat flux is assumed on all internal boundaries between the subdomains of the system. Heat convection in the CPA solution is assumed negligible in the current analysis due to the high viscosity of the solution at the starting temperature of -50°C [12].

The heat transfer between the external system boundaries and the mixed air within the cooling chamber is:

$$-k_i \frac{\partial T_i}{\partial \hat{n}} = U(T_i - T_c) \tag{5.2}$$

where $\hat{n}$ is the normal to the system's outer surface and U is overall heat transfer coefficient, combining effects of convection and thermal radiation.

5.2.4 Thermal Properties

The objective in the current study is two-fold: (i) to investigate whether a specific cryogenic cooling protocol ensures complete vitrification in a rabbit kidney model, and (ii) to investigate if the same protocol is expected to yield similar results in a human kidney model. The approach taken in this study is to investigate the envelope conditions, rather than to investigate a wide selection of special cases. The base case analyzed in this study is of a completely vitrified system, where latent heat effects are absent, and for which thermophysical properties are readily available (Table 5.1). In particular, thermal conductivity data on relevant vitrified CPA cocktails have been recently developed [15,16] and are included in the current study (Table 5.1).

An additional case is investigated where complete vitrification is also assumed, but for which water ice thermophysical properties are taken instead of the vitrified CPA properties. The rationale for this specific investigation is to explore the errors that such material properties selection might lead to—a repeated practice in theoretical studies in the absence of specific data. This special case is not simulative of partial crystallization as the latent heat effect is not included. A partially vitrified material will display mid-range thermophysical properties between the amorphous and

the ice-like state. Such properties could be first-order approximated using the effective medium theory (EMT), based on the constituent volume fractions and properties of the primitive ingredients [76].

Consistent with prior experimental studies [27,29], the properties of M22 are selected for the vitrified CPA. Four limiting cases are investigated in this study: a fully vitrified rabbit kidney model using CPA properties (RV) and water ice properties (RI), and a fully vitrified human kidney model using CPA properties (HV) and using water ice properties (HI).

The specific thermophysical properties used in this study are listed in Table 5.1, including low-density polyethylene (LDPE) as a container material for cryogenic temperatures. It can be seen from Table 5.1 that water occupies roughly 78% of the rabbit kidney cortex and 82% of the rabbit kidney medulla. During vitrification, the entire kidney is approximated as having the same thermal conductivity as the pure CPA solution for the following reasons: (i) the thermal conductivity of the non-aqueous components of the tissue differs by only 18% from that of M22 at 0°C as compiled by the EMT theory (0.31 W/m-°C for M22 and 0.26 W/m-°C for the non-aqueous material [75]); (ii) the thermal conductivity of vitrified M22 varies by only 10% over the temperature range of -135°C and 0°C (from 0.28 W/m-°C to 0.31 W/m-°C, respectively) [15]; and, (iii) data is unavailable to compile the thermal conductivity of the non-aqueous components of the tissue at cryogenic temperatures.

While the specific heat monotonically decreases with decreasing temperature, the sudden change in its rate at the glass transition temperature is neglected in this study for simplicity in calculations. The glass transition temperature, T_g, for M22 is -123°C, which is about 11°C above the storage temperature in this study, and has a minimal effect on energy removal during cooling.

A reference solution of 7.05M DMSO is also listed in Table 5.1, which has served well in previous studies of thermo-mechanical stresses in cryopreservation [58,62]. The difference in thermal conductivity between vitrified M22 and vitrified 7.05M DMSO is 5.2% at -22°C and 3.5% at -135°C, which is within the range of experimental uncertainties [14,15]. Due to the similarity in thermal conductivity characteristics and since the specific heat for M22 is unavailable, the specific heat of 7.05M DMSO is assumed to apply for the present vitrified system.

5.2.5 Ice Formation Tendency in Dilutions of M22

While the medulla and the cortex are approximated to have the same thermal properties due to their high CPA concentrations, a small deviation in actual concentration may affect significantly the CCR needed to ensure vitrification. While nearly 100% of the full concentration of M22 is expected to be reached in the renal cortex, conferring a CCR of 0.1°C/min and possibly even slower [79], we wanted to verify that a typical, previously reported medullary concentration of just 92.1% of the full concentration of M22 [27] would have a CCR slower than 1°C/min, as previously inferred [27]. Once verified, CCR of 1°C/min would be taken as an indication of vitrification success in the thermal analysis in this study.

We therefore undertook a differential scanning calorimetry (DSC) investigation to determine the threshold concertation that ensures vitrification at a cooling rate of at least 1°C/min. Dilutions of M22 in its standard carrier solution LM5 [10] were cooled at 1°C/min from -22°C down to -90°C, below which further ice growth is inhibited by high solution viscosity [23]. Samples were then warmed from -90°C back to -22°C at 160°C/min, while searching for the melting peak heat flux on the DSC output as an indication of any ice that formed. This rapid warming rate is beneficial for instrument sensitivity and avoidance of ice growth during warming.

In increments of 2.5% in concentration, this investigation revealed that, at a cooling rate of 1°C/min, 1.27% w/w ice formed in 85% M22 and 0.085% w/w ice formed in 87.5% M22. Using the Boutron convention of a 0.2% w/w ice threshold as the criterion for defining the CCR [5], the concentration of M22 that will remain vitreous at a cooling rate of 1°C/min is about 87% of full M22. This concentration threshold is lower by 5.1% than the 92.1%-of-full-M22 concentration previously reported to be achieved in the inner medulla of a rabbit kidney that survived indefinitely after vitrification, rewarming, and transplantation [6]. The critical cooling rate of 92.1% M22 is clearly <<1°C/min, and too slow to easily measure, which indicates that if cooling rates on the order of 1°C/min can be achieved in human kidneys, there is no question that they can be vitrified successfully.

5.2.6 Numerical Solution

The FEA commercial code ANSYS was used to simulate heat conduction in the system, with the element mesh displayed in Fig. 5.1c. Due to geometrical complexity, the CPA solution and the kidney were meshed using tetrahedral (SOLID87) and hexahedral (SOLID90) elements based on an ANSYS meshing algorithm. Program-controlled inflation was used during mesh generation,

with finer discretization at the interface between the medulla and the cortex, and at the outer surface of the cortex. In total 49,197 elements were used in the case of the human kidney and 26,231 elements were used in the case of the rabbit kidney, which satisfied a mesh convergence analysis for the thermal solution.

Eleven numeric labels are displayed in Fig. 5.1c, simulating strategically placed virtual temperature sensors for the purpose of thermal analysis. In general, one sensor is placed at the geometric center of the kidney, five sensors on the outer surface of the kidney (surface S_o), and five on the interface between the medulla and the cortex (surface S_i). The specific sensor locations are: (0) the geometric center of the kidney, (1) the point of contact between kidney cortex and the base of the container, (2) the point of contact between the kidney cortex and the container wall, (3) the highest point on S_o, (4) the closest point on S_o to the geometric center of the system (11.5 mm and 8.4 mm apart for the human case and rabbit case, respectively), (5) the farthest point on S_o from point 2 in the horizontal direction, (6) the lowest point on S_i, (7) the farthest point on S_i from the geometric center of the system, (8) the highest point on S_i, (9) the closest point on S_i to the geometric center of the system (5.4 mm and 4.8 mm apart for the human case and rabbit case, respectively), and (10) the closest point on S_i to point 5 in the horizontal direction. The thermal histories collected from those virtual sensors were used to determine the instantaneous variations in temperature and in cooling rate, as discussed below.

The numerical solution was executed from the time of kidney immersion in the precooled M22 and down to the storage temperature of -135°C. At the time of immersion, the initial temperature of the kidney was -22°C while the temperature of the precooled M22 in the container was -50°C. Thermal equilibrium at cryogenic storage was assumed after the slowest responding point in the kidney conformed to 99.5% of the overall change in kidney temperature, which equals -134.4°C (the kidney is cooled from -22°C to -135°C during the simulation). A time-step convergence study for the FEA yielded a time-step value of 12.5 s for numerical simulations.

5.3 Results and Discussion

Figure 5.2 displays the thermal history in the cooling chamber, T_c, the thermal history at the geometric center of the kidney, T_0, and the thermal history range on surfaces S_o and S_i, as compiled from the outputs of the virtual sensors presented in Fig. 5.1c. Close inspection of FEA results at all mesh nodes confirmed that, indeed, those sensors capture the temperature range along the

respective surfaces, although different sensors may display extreme values at different times. As can be expected, the temperature distribution within the kidney becomes less uniform with the increasing size of the system. The system containing the human kidney is 21 times larger than the system containing the rabbit kidney.

The sudden immersion of the kidney in a surrounding CPA solution at the onset of cooling leads to a step-like temperature change on the surface of the kidney, S_o (from -22°C to -50°C). The result of this sudden temperature drop is not fully captured graphically in the time scale relevant to Fig. 5.2, where almost instantaneously the surface temperatures drops to about -36°C—the average initial temperatures of the kidney and the surrounding CPA solution. The propagation of thermal information from that surface is measured in a much longer time scale, which is proportional to the thermal diffusivity (the ratio of thermal conductivity to the volumetric specific heat).

A significantly longer period of time is required for the vitrified systems to approach steady state (defined by 99.5% response; see Numerical Solution section for further discussion). For the cases presented in Fig. 5.2, the RV and HV cases required 25.8 min and 176.7 min to approach the steady state, respectively, while the RI and HI cases required only 9.8 and 15.4 min to approach a steady state, respectively. The significantly different results of the RV/HV cases from the RI/HI cases underscores the importance of using thermal properties of the specific CPA solution for vitrification simulations, rather than attempting to approximate them as similar to those of ice.

In general, the significant differences between an amorphous CPA system and a crystallized water system bound the range of thermal conductivity values for the case of a partially vitrified system [14]. Nonetheless, due to the high CPA concentration, partially vitrified solutions will exhibit properties closer to those of a completely vitrified system [16]. Furthermore, when a partially vitrified system is under consideration, one must bear in mind that crystallization may be spatially non-uniform and further dependent upon the local thermal history and the stochastic presence of local nucleation events and concentration fluctuations. This means that partial vitrification scenarios must be investigated on a case-by-case basis. Fortunately, due to the relatively low CCR of M22 and its relatively slow kinetics of crystallization [79], the outcome from any practical case of partial kidney vitrification will likely be much closer to the outcomes of the RV and HV cases.

It can be seen from Fig. 5.2 that the temperature distribution on the outer surface of the

kidney, S_o, is less uniform than the temperature distribution on S_i. Comparing the differences in temperature ranges between S_i and S_o with the temperature differences between T_0 and S_i indicates steeper temperature gradients across the cortex. More generally, the wide temperature ranges displayed in Fig. 5.2 highlight the difficulty in temperature measurements in experimental studies when only one or a few sensors are attached to the outer surface of the kidney. This difficulty intensifies with increased organ size. It follows that several strategically placed sensors are required to determine the thermal history in kidney experiments, where their strategic locations can be informed by numerical simulations.

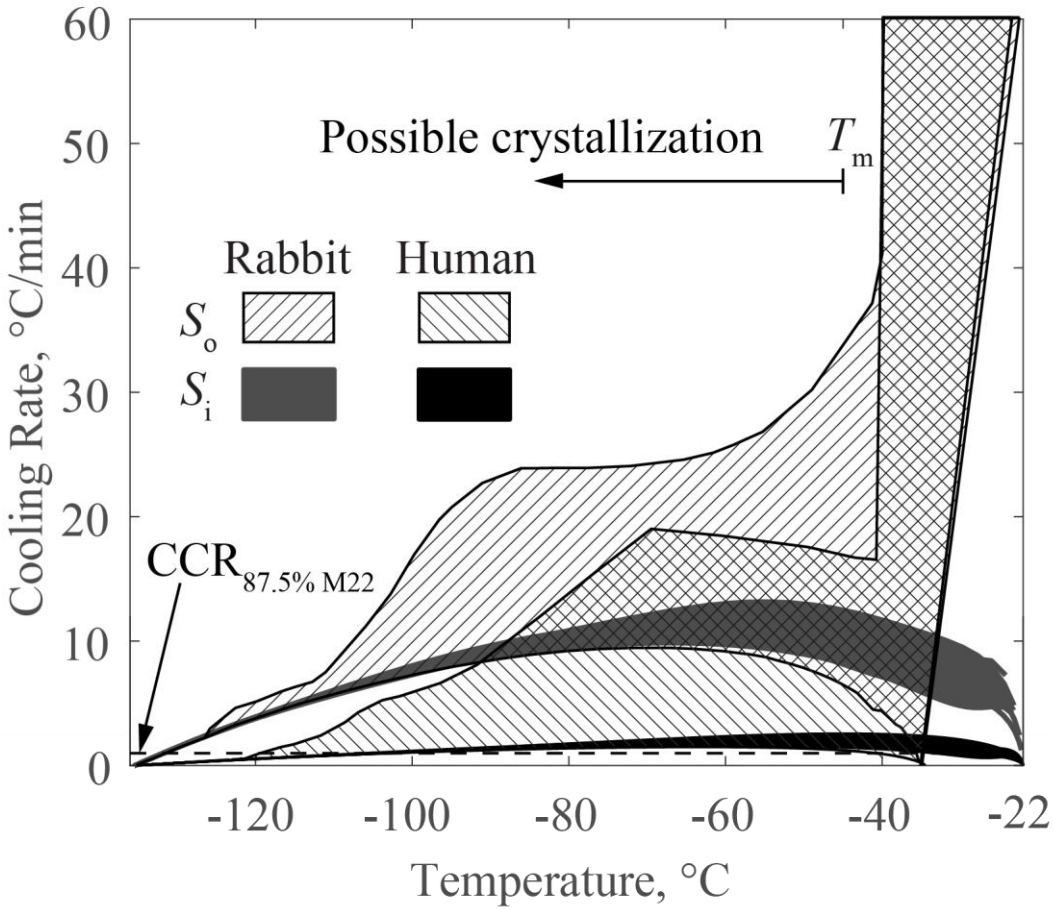

Figure 5.3: Cooling rate history in the vitrified kidney model, where S_o is the outer surface of the cortex S_i is the medulla-cortex interface (Fig. 1c), and CCR_{med} is the critical cooling rate for 87% M22 in the medulla (1 $^oC/min$).

Figure 5.3 displays the cooling-rate history at the center of the kidney and the respective cooling-rate ranges on surfaces S_o and S_i. Recall that the sudden immersion of the kidney (initially at -22ºC) in the surrounding CPA solution (initially at -50ºC) leads to a rapid kidney surface cooling immediately after immersion (Fig. 5.2). Consequently, it warms up the surrounding CPA solution above its initial temperature of -50ºC, while the temperature of the cooling chamber hosting the container continues to decrease according to its preset controlled thermal history. Shortly thereafter, the entire surrounding CPA solution is cooled again below -50ºC, eventually leading to thermal equilibrium at the storage temperature. This effect of initial warming of the surrounding CPA solution while the temperature of the cooling chamber keeps dropping leads to an adverse effect of diminished cooling rates close to the surface at the early stage of the process, when the kidney surface temperature is about -36ºC (recall, the initial temperature average of the precooled surrounding CPA and the perfused kidney).

Fortunately, the above sudden decrease in cooling rates take place above the melting temperature for 90% M22, which is -45ºC [77]. By the time that any local temperature in the kidney reaches -45ºC, its corresponding cooling rate is already above 1ºC/min, which is higher than the CCR for the solution concentrations under consideration (≥92.1%, see Materials and Methods). For reference, the minimum cooling rate anywhere in the human kidney at -45ºC, -75ºC, -100ºC, and -123ºC is 1.2 ºC/min, 1.5 ºC/min, 1.5 ºC/min, and 0.4 ºC/min, respectively.

Counterintuitively and quite seriously, if the initial temperature of the surrounding CPA were lower than -50ºC, it is possible that the local cooling rate at some portion of the kidney would drop below the CCR and some extent of harmful ice crystals may form at higher temperatures. For example, an initial surrounding CPA solution temperature of -70ºC would result in subcritical cooling rate near the surface of the kidney when it almost instantaneously reaches the average temperature of -46ºC. Note that maximum crystal growth rate is observed at temperatures closer to the melting temperature, while the maximum ice nucleation rate is found closer to the glass transition temperature [77]. The latter effect is not easy to infer from visualization of physical events in large specimens [30,32].

While the adverse effect of initial surrounding CPA solution rewarming can be reduced by a carful thermal design of the process and its specialized hardware, it signifies the need for computer simulations in the design of the cryopreservation protocol. Given the obtained cooling rates and

the dependency of the CCR on the CPA solution concentration, results of this study farther signify the critical need to design means for improved CPA solution substitution in the organ. The possibility of marginal cooling rates at some portion of the kidney also signifies the need for detailed modeling of the thermophysical properties. Measurement of physical properties during partial vitrification represents a relatively uncharted area of research [14,16,18,46,62].

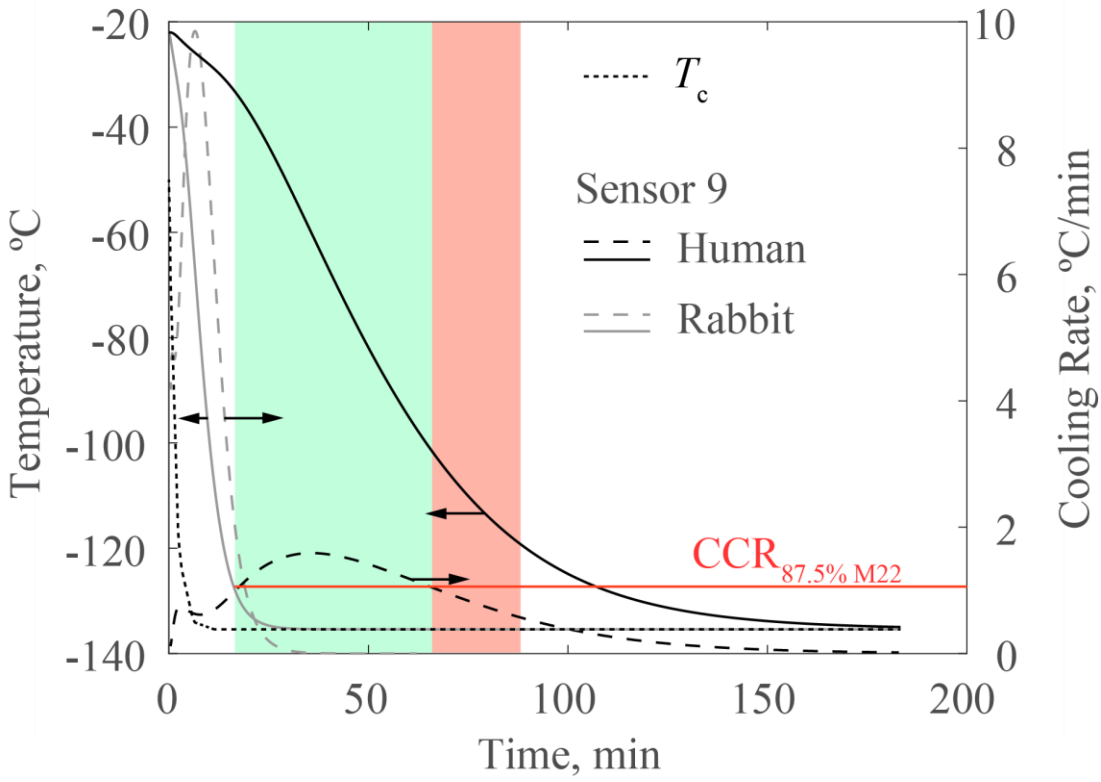

Figure 5.2: Thermal history of Sensor 9 (the closest point in the medulla to center of system) for the cases of a vitrified human kidney and a vitrified rabbit kidney. The colored areas refer to the human kidney simulation, where green corresponds to the time range in which the sensor indicates temperatures below T_m and the cooling rate is above the CCR of 87% M22, while red corresponds to the time range in which the sensor indicates temperatures above T_g and the cooling rate is below CCR of 87% M22; colored areas interface at -103ºC.

Figure 5.4 displays the thermal history at Sensor 9, which is the closest to the geometric center of the system (5.4 mm and 4.8 mm from the center for the human and rabbit kidney,

respectively). While the cooling rate for the rabbit kidney (RV) case exceeds the CCR within the relevant temperature range of T_m to T_g, the human kidney (HV) case shows subcritical cooling rates between -103ºC and T_g. Figure 5.5 displays the temperature fields in the cross section of the kidney for the HV case when the same sensor temperature indicates -30ºC, -60ºC, -90ºC, and -120ºC. The respective cooling rates at the same location at the corresponding points in time are 0.8ºC/min, 1.6ºC/min, 1.3ºC/min, and 0.5ºC/min.

It can be observed from Fig. 5.4 that the cooling rate at Sensor 9 falls below the CCR of 1ºC/min in the temperature range of -103ºC and T_g, where the nucleation rate is the highest. It can further be seen from Fig.5. 4 that the cooling rate at Sensor 9 is always below -1.6 ºC/min, which is in a relative close range to the CCR at the medulla.

The observations reported here could be taken to suggest that the vitrification of a human kidney could be marginal given that the CCR for 87% M22 is not always attained during all phases of cooling. However, the CCR for 92.1% M22 is considerably lower, and that concentration is known to be achievable at least in the rabbit kidney. Furthermore, although the CCR is defined without regard to the temperature dependence of the CCR, in fact, damaging ice formation is only possible at relatively high temperatures (>-90ºC) during cooling, so cooling rates that only fall below the nominal CCR at very low temperatures, when the CPA viscosity is high enough to inhibit ice growth, need not preclude successful vitrification during cooling. However, long cooling times between -100ºC and T_g promote nucleation of large numbers of new ice crystals on the nanoscale. Although stable and innocuous at low temperature, these ice nuclei complicate later recovery of the organ by requiring warming rates faster than the CCR to minimize their growth during passage through warmer temperatures favorable for ice growth. The difficulties of warming successfully are expected to worsen with increasing time spent between -100ºC and T_g, where the ice nucleation rate is maximum, although the magnitude of the effect has not been determined. As Mehl has pointed out, ice nuclei formed near T_g tend to all be the same size and to grow at the same rate upon warming, which means that a warming rate sufficient to limit a few ice crystals to innocuous sizes may be sufficient to limit many ice crystals to innocuous sizes.

Additional steps can be taken to reduce the likelihood of crystallization in the kidney on cooling. The most important of these is to maximize the concentration of M22 in the medulla, and recent innovations have made this possible [20,23]. From a thermal engineering point of view, another option is to reduce the overall volume of the container while tailoring it to the shape of the

kidney, which will decrease the overall heat capacity of the system (heat capacity being the product of specific heat and mass) and hence accelerate cooling. Since the kidney mass is only about ¼ of the entire system, the scope for improving the average cooling rate in this way is significant. By the same token, the CPA solution surrounding the kidney can slow down later rewarming, but this effect could also be reduced by using computer simulations to optimize the design of the cryopreservation equipment. However, RF rewarming may add additional constraints on the container shape, which are beyond the scope of the current study.

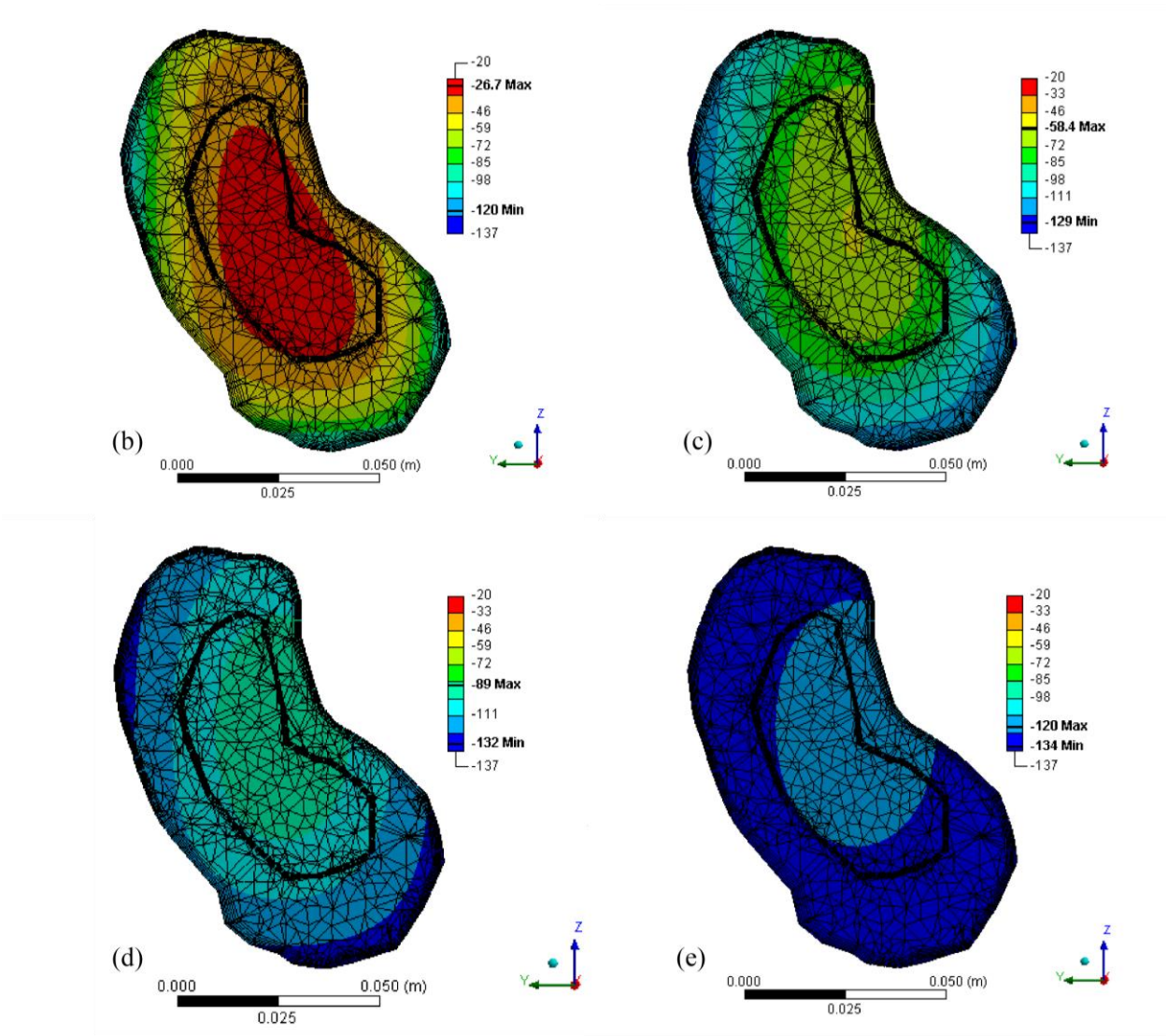

Figure 5.5: Temperature fields when the Sensor 9 indicates (a) -30°C, (b) -60°C, (c) -90°C, and (d) -120°C.

5.4 Conclusions

Thermal analyses of a rabbit kidney and a human kidney are presented in this study, subject to conditions that have proven successful in vitrification experiments on a rabbit model. This study is based on computer simulations using the FEA commercial code ANSYS. An adult human male kidney model is used in this study, analyzed in a cylindrical container suitable for radiofrequency rewarming. The rabbit kidney model is essentially a 21 fold scaled-down version of the human kidney, to meet previous experimental parameters [27]. This study integrates newly generated data on the CCR for M22 concentrations relevant to kidney cryopreservation, where M22 is a proprietary CPA cocktail successfully used in previous experiments, and criteria for vitrification success are obtained with at least 5% concentration margins.

Results of this study demonstrate that the temperature distribution within the kidney becomes significantly less uniform when the system is scaled up from a rabbit size to a human size. Consistently, the cooling rate distribution increases with the increasing size of the kidney, and yet even in the case of the human kidney, cooling rates remain high enough in all parts of the kidney to prevent ice formation at temperatures above -100^{o}C. This was observed despite the fact that the volume modelled in the case of human kidney was 21 fold larger than that modelled in the case of the rabbit kidney. Nevertheless, it would still be desirable to reduce the overall volume of the kidney container, particularly by tailoring it to the shape of the kidney. The thermal design of optimal kidney packaging is left for future studies.

In conclusion, this study demonstrates the value of thermal design and analysis of cryopreservation protocols using computer simulations. This study further highlights the unmet need for measuring the thermophysical properties of the CPA solutions in the relevant thermal histories. In particular, several strategically placed sensors may be required to determine the thermal outcome in kidney experiments due to variations in thermal history across the organ, to be informed by numerical simulations.

Chapter 6

Conclusions and Future Work

6.1 Conclusions

The work presented in this thesis combines an experimental study on the thermal conductivity of relevant materials, and a theoretical study to identify the effects of the measured values on cryopreservation protocols. These studies are meant to inform future cryopreservation protocols and to advance the possibility of organ preservation. The unique contributions presented in these studies are: (i) modification of the cryomacroscope device and creation of a setup for thermal conductivity measurements based on the existing transient hot wire technique, (ii) development of a protocol for thermal conductivity measurements during rewarming, (iii) generation of a data bank of temperature-dependent thermal conductivity of CPA, including 2-10 M DMSO, DP6, and DP6 with SIMs, (iv) verification of the functionality of the transient hot wire technique under non-isothermal conditions, (v) investigation of the limits of the transient hot wire technique in cryomacroscopy for non-isothermal conditions (to be completed in the future), (vi) thermal analysis of a vitrifying rabbit kidney based on an established rabbit kidney cryopreservation protocol, and (vii) exploring scale-up thermal effects to a human-size organ.

The significance of the dependency of thermal conductivity on temperature has been established as an important consideration for heat transfer analyses of large systems undergoing cryopreservation [57]. The experimental studies presented here are specifically aimed at quantifying this dependency in DMSO solutions and DP6 with SIMs, while taking into account two physical processes that affect the outcome of cryopreservation: crystallization and vitrification. The established transient hot-wire measurement technique is integrated for the first time into the scanning cryomacroscope, a device created to visualize physical events during cryopreservation.

It is shown in the DMSO solutions that the thermal conductivity of the crystallized material varies significantly with the concentration. In DMSO, samples in the concentration range of 2 M and 6 M DMSO were found to crystallize in the experimented thermal protocol. The thermal conductivity of the crystallized material is found to increase with the decreasing temperature, in the temperature range applicable to cryobiology (above -180°C). This behavior is expected to

change at near-absolute zero temperatures. In contrast the thermal conductivity of vitrified DMSO solutions in the range of 7.05 M to 10 M is not observed to be significantly dependent on concentration. The dependency of the thermal conductivity on temperature of the vitrified solution appears to follow the same trend from the liquid phase, which is to gradually decrease in thermal conductivity with the decreasing temperature. These opposing trends between the crystallized and vitrified material reach a tenfold difference at -180°C.

The thermal conductivity of DP6 in combination with SIMs and EC has been shown to vary by three fold between the amorphous and crystalline phases of DP6 below the glass transition temperature. However, the current experimental setup does not permit the quantification of the extent of crystallization in terms of volume ratio. Results of this study further demonstrate the ability of SIMs to decrease the extent of crystallization in DP6, even at subcritical cooling and rewarming rates. Finally, results of this study demonstrate an additional ice suppression capability of EC, which may be disproportionate to its volume ratio in the cocktail.

When SIMs are successfully applied, the thermal conductivity of the CPA+SIM cocktail is essentially the same as that of the vitrified CPA. The benefit for large-size cryopreservation is that the addition of SIMs lowers the critical cooling rates required for successful vitrification. Unfortunately, given the kinetics of ice crystallization and also the path-dependent nature of the cryopreservation process, it is difficult to predict a priori when significant crystallization will occur for a particular combination of CPA, SIMs, vehicle solution, and specific thermal history. Hence, characterization of thermal conductivity is most applicable if performed by mimicking the specific thermal history expected within a large specimen with the specific set compounds.

A study was done to verify that the transient hot wire technique is effective for non-isothermal conditions. A finite element heat transfer analysis was performed in ANSYS to simulate the conditions under which thermal conductivity measurements of cryoprotective agents (CPAs) are made with the transient hot wire technique in conjunction with the scanning cryomacroscope during rewarming. The 3-D modification to the shape of the wire probe and the non-uniform temperature distribution in the CPA domain during the rewarming of the CPA prompted this analysis, as these conditions can potentially skew the temperature response curve of the wire probe from which thermal conductivity is extracted.

The temperature profile along the wire probe is found to span a larger range than the $\Delta T_{\tau,\,avg}$ signal itself, but retains a consistent shape during the measurement, indicating that the temperature

distribution along the wire is found to be changing at a uniform rate, and $\Delta T_{\tau,\,avg}$, is representative of relative changes in T at most points along the wire during heating. The resulting thermal conductivity measurements were found to be accurate within experimental uncertainty under the conditions of the experiment. More work will follow to probe the limitations of the technique with regard to rewarming rate and thermal conductivity of the measured medium (see chapter 6.2.1: Finite Elements Evaluation of Error in Transient Hot-Wire: Probing the Limitations of the Technique).

The implications of the observed thermal conductivity differences between the amorphous and crystalline phases of the same CPA cocktail on cryopreservation simulations is significant. In broad terms, the lower thermal conductivity in the amorphous state creates less favorable conditions to maintain the high cooling and rewarming rates at the center of large specimens that are required to ensure vitrification. In turn, when partial crystallization occurs within the specimen, the structural integrity of the material may be compromised due to differential thermal expansion between the crystallized and the amorphous regions. Hence, thermal conductivity data is not only critical for the prediction of the likelihood of vitrification, but also for the prediction of structural damage in cryopreservation protocols. Measurements of thermal conductivity of CPA are used in the former case in this study, where likelihood of vitrification is evaluated.

Thermal analyses of a rabbit kidney and a human kidney are presented in this study, subject to conditions that have led to successful outcomes in vitrification experiments on a rabbit kidney. This study is based on computer simulations using the FEA commercial code ANSYS. An adult human male kidney model is used in this study, analyzed in a generic cylindrical container. The rabbit kidney model is essentially a 21 fold scaled-down version of the human kidney, to meet previous experimental parameters [27]. Two general cases are investigated in this study, representing a fully vitrified system and a fully crystallized system. While complete vitrification is conceivable in the system under some conditions, complete crystallization is an unrealistic scenario with the CPA selected. Nonetheless, the latter extreme case bounds the range of possible outcomes for partial vitrification. Detailed analysis of partial vitrification requires a case-by-case study using specialized thermal properties, which is beyond the scope of the current study.

Results of this study demonstrate that the temperature distribution within the kidney becomes significantly less uniform when the system is scaled up from a rabbit size to a human size. Consistently, the cooling rate distribution increases with the increasing size of the kidney, and yet

even in the case of the human kidney, cooling rates remain high enough in all parts of the kidney to prevent ice formation at temperatures above -100^{o}C. This was observed despite the fact that the volume modelled in the case of human kidney was 21 fold larger than that modelled in the case of the rabbit kidney. Nevertheless, it would still be desirable to reduce the overall volume of the kidney container, particularly by tailoring it to the shape of the kidney. The thermal design of optimal kidney packaging is left for future studies.

In conclusion, this study demonstrates the value of thermal design and analysis of cryopreservation protocols using computer simulations. This study further highlights the unmet need for measuring the thermophysical properties of the CPA solutions in the relevant thermal histories. In particular, several strategically placed sensors may be required to determine the thermal outcome in kidney experiments due to variations in thermal history across the organ, to be informed by numerical simulations.

6.2 Future Work

6.2.1 Finite Elements Evaluation of Error in Transient Hot-Wire: Probing the Limitations of the Technique

The thermal model of the transient hot wire thermal conductivity measurement presented in chapter 4 has been used to duplicate a single set of practical experimental conditions in order to investigate whether or not these conditions would cause distortion in a thermal conductivity measurement by shifting the slope of the ΔT vs. ln t curve from which thermal conductivity is extracted. Although useful results have come from this study, they only verify the accuracy of the technique under said conditions. To create a unique contribution, it would be prudent to use the thermal model to investigate possible limitations of the measurement technique in the realistic lab scenario. Practical limitations to investigate would be (1) the fastest rewarming rate that could be imposed, (2) the highest thermal conductivity material that could be measured without distorting thermal conductivity by more than 10%, and (3) The highest $\frac{dk}{dT}$ material that could be measured without distorting thermal conductivity by more than 10%. Regarding the first limitation, the greater the rewarming rate imposed on the cuvette in the cooling chamber the larger the temperature distribution in the CPA domain, and the larger the resulting temperature distribution would be along the length of the wire. The second limitation, the highest thermal conductivity

material that could be measured with the technique, is of interest due to the systematically low thermal conductivity measured due to the low thermal conductivity of the ABS peg with which the thermal conductivity sensor is in thermal contact with. The already established upper bound of the thermal conductivity of this material must result in a smaller penetration depth than half the distance between the two branches of the "U" of the sensor over the course of the measurement. Finally, the third limitation explores the combination of a large temperature distribution along the wire with a very highly temperature-dependent thermal conductivity material.

6.2.2 Thermal Conductivity of Vitrifying Kidney Tissue in CPA

Following the justifications used in chapter 5 regarding the use of thermal properties of vitrified CPA as a substitute for vitrified kidney tissue perfused with CPA, it would be valuable to check the validity of this substitution with the temperature-dependent thermal conductivity measurement protocol described in chapter 2. The current experimental setup would be adequate with little to no adjustment if the kidney tissue were soaked in a CPA solution and ground or cut into small pieces which could easily envelope the hot wire sensor and ABS mount. Based on thermal conductivity measurements of lean beef versus ground beef, which each have a thermal conductivity of 0.410 W/m-K and 0.406 W/m-K at 6°C with 76% and 67% water content, respectively [84], it would appear as though changing the macroscopic structure of the tissue (i.e.-grinding it or cutting it) would not detectably alter thermal conductivity.

6.2.3 Thermal Analyses of a Human Kidney and a Rabbit Kidney during Cryopreservation with Possibility of Phase Change

To add refinement to the discussion and analysis of chapter 5, a computational framework and accompanying differential scanning calorimetry (DSC) measurements are being developed by the current research team to include the possibility of partial crystallization in the kidney model presented in chapter 5. The utility of this refinement would be that the extent of crystallization and thus survival outcome, could be estimated. Some systems can tolerate a small amount of ice crystallization, so the extent of crystallization in the kidney is an important consideration. In the work presented in chapter 5, all cooling rates in the human medulla are found to be sub-critical at some point in the cooling phase of the simulation. However, in a practical situation, the unfrozen region of CPA and tissue would experience an increase in solute concentration as the first few

small ice crystal lattices formed and rejected solutes. This increase in concentration would also suppress the critical cooling rate to a lower value in the unfrozen region, possibly preventing any further crystallization. Thus, although it is found in the model presented in chapter 5 that the entire human medulla faces risk of crystallization, the risk may be mild.

List of Publications

Journal Publications	Chapter
L.E. Ehrlich, J.S.G. Feig, S.N. Schiffres, J.A. Malen, Y. Rabin, Large Thermal Conductivity Differences between the Crystalline and Vitrified States of DMSO with Applications to Cryopreservation, PLoS ONE. 10 (2015) e0125862.	2
L.E. Ehrlich, J.A. Malen, Y. Rabin, Thermal conductivity of the cryoprotective cocktail DP6 in cryogenic temperatures, in the presence and absence of synthetic ice modulators, Cryobiology. 73 (2016) 196–202.	3
L.E. Ehrlich, J.A. Malen, Y. Rabin, Finite Elements Evaluation of Error in Thermal Conductivity Measurements by the Transient Hot Wire Technique due to Non-Uniform Temperature Field in Sample, *In Preparation*	4
L.E. Ehrlich, G. M. Fahy, B. G. Wowk, J.A. Malen, Y. Rabin, Thermal Analyses of a Human Kidney and a Rabbit Kidney During Cryopreservation by Vitrification, *In Preparation*	5

Conferences

LE Ehrlich, J.S.G. Feig, S.N. Schiffres, J.A. Malen, Y. Rabin. "A New Device and Technique for Thermal Conductivity Measurements of Glass-Forming Materials With Application to Cryopreservation." *ASME 2013 Heat Transfer Summer Conference*, Minneapolis, MN. 14-19 July 2013. Conference Presentation.	2

LE Ehrlich, J.S.G. Feig, S.N. Schiffres, J.A. Malen, Y. Rabin. “Integration of transient hot-wire method into scanning cryomacroscopy in the study of thermal conductivity of dimethyl sulfoxide.” *CRYO2013,* Bethesda, MD. 28-31 July 2013. Conference Presentation. 2

LE Ehrlich. “Significant Contrasts in Thermal Conductivity of Crystalline and Vitrified Cryoprotectants” *MRS Spring Meeting and Exhibit*, San Francisco, CA. 6-10 April 2015. Poster. 2,3

LE Ehrlich. “Thermal Conductivity Measurements of Cryoprotectants at Low Temperatures” *IMECE,* Houston, TX. 13-19 November 2015. Conference Presentation. 3

References

[1] T.M. Aminabhavi, B. Gopalakrishna, Density, Viscosity, Refractive Index, and Speed of Sound in Aqueous Mixtures of N,N-Dimethylformamide, Dimethyl Sulfoxide, N,N-Dimethylacetamide, Acetonitrile, Ethylene Glycol, Diethylene Glycol, 1,4-Dioxane, Tetrahydrofuran, 2-Methoxyethanol, and 2-Ethoxyethanol at 298.15 K, J. Chem. Eng. Data. 40 (1995) 856–861.

[2] S. Baicu, M.J. Taylor, Z. Chen, Y. Rabin, Cryopreservation of carotid artery segments via vitrification subject to marginal thermal conditions: Correlation of freezing visualization with functional recovery, Cryobiology. 57 (2008) 1–8.

[3] A. Baudot, L. Alger, P. Boutron, Glass-forming tendency in the system water-dimethyl sulfoxide, Cryobiology. 40 (2000) 151–158.

[4] N.O. Birge, Phys. Rev. B 34, 1631 (1986) - Specific-heat spectroscopy of glycerol and propylene glycol near the glass transition, (n.d.).

[5] P. Boutron, Glass-Forming Tendency and Stability of the Amorphous State in Solutions of a 2,3-Butanediol Containing Mainly the Levo and Dextro Isomers in Water, Buffer, and Euro-Collins, Cryobiology. 30 (1993) 86–97.

[6] D.G. Cahill, R.O. Pohl, Thermal conductivity of amorphous solids above the plateau, Phys. Rev. B. 35 (1987) 4067–4073.

[7] D.G. Cahill, R.O. Pohl, Lattice Vibrations and Heat Transport in Crystals and Glasses, Annu. Rev. Phys. Chem. 39 (1988) 93–121.

[8] D.G. Cahill, R.O. Pohl, Heat flow and lattice vibrations in glasses, Solid State Commun. 70 (1989) 927–930.

[9] B. Cheong, R. Muthupillai, M.F. Rubin, S.D. Flamm, Normal Values for Renal Length and Volume as Measured by Magnetic Resonance Imaging, Clin. J. Am. Soc. Nephrol. 2 (2007) 38–45.

[10] J. Choi, J.C. Bischof, Review of biomaterial thermal property measurements in the cryogenic regime and their use for prediction of equilibrium and non-equilibrium freezing applications in cryobiology, Cryobiology. 60 (2010) 52–70.

[11] R.V. Devireddy, D.J. Smith, J.C. Bischof, Effect of Microscale Mass Transport and Phase Change on Numerical Prediction of Freezing in Biological Tissues, J. Heat Transf. 124 (2001) 365–374.

[12] F.A. Duck, Physical Properties of Tissues: A Comprehensive Reference Book, Academic Press, 2013.

[13] EDQM, International Figures on Donation and Transplantation - 2015, 2016.

[14] L.E. Ehrlich, J.S.G. Feig, S.N. Schiffres, J.A. Malen, Y. Rabin, Large Thermal Conductivity Differences between the Crystalline and Vitrified States of DMSO with Applications to Cryopreservation, PLoS ONE. 10 (2015) e0125862.

[15] L.E. Ehrlich, J.A. Malen, Y. Rabin, Unpublished Data: Thermal Conductivity of M22, (2016).

[16] L.E. Ehrlich, J.A. Malen, Y. Rabin, Thermal conductivity of the cryoprotective cocktail DP6 in cryogenic temperatures, in the presence and absence of synthetic ice modulators, Cryobiology. 73 (2016) 196–202.

[17] D.P. Eisenberg, P.S. Steif, Y. Rabin, On the effects of thermal history on the development and relaxation of thermo-mechanical stress in cryopreservation, Cryogenics. 64 (2014) 86–94.

[18] D.P. Eisenberg, M.J. Taylor, Y. Rabin, Thermal expansion of the cryoprotectant cocktail DP6 combined with synthetic ice modulators in presence and absence of biological tissues, Cryobiology. 65 (2012) 117–125.

[19] S. Evans, Electromagnetic Rewarming: The Effect of CPA Concentration and Radio Source Frequency on Uniformity and Efficiency of Heating, Cryobiology. 40 (2000) 126–138.

[20] G. Fahy, 041 Consequences and control of ice formation in the renal inner medulla, Cryobiology. 67 (2013) 409–410.

[21] G.M. Fahy, The relevance of cryoprotectant "toxicity" to cryobiology, Cryobiology. 23 (1986) 1–13.

[22] G.M. Fahy, Methods of using ice-controlling molecules, 2003.

[23] G.M. Fahy, Elimination of most damage after perfusing rabbit kidneys with M22 solutions, Cryobiology. 73 (2016) (in press).

[24] G.M. Fahy, D.I. Levy, S.E. Ali, Some emerging principles underlying the physical properties, biological actions, and utility of vitrification solutions, Cryobiology. 24 (1987) 196–213.

[25] G.M. Fahy, D.R. MacFarlane, C.A. Angell, H.T. Meryman, Vitrification as an approach to cryopreservation, Cryobiology. 21 (1984) 407–426.

[26] G.M. Fahy, B. Wowk, R. Pagotan, A. Chang, J. Phan, B. Thomson, L. Phan, Physical and biological aspects of renal vitrification, Organogenesis. 5 (2009) 167–175.

[27] G.M. Fahy, B. Wowk, R. Pagotan, A. Chang, J. Phan, B. Thomson, L. Phan, Physical and biological aspects of renal vitrification, Organogenesis. 5 (2009) 167–175.

[28] G.M. Fahy, B. Wowk, J. Wu, Cryopreservation of complex systems: the missing link in the regenerative medicine supply chain, Rejuvenation Res. 9 (2006) 279–291.

[29] G.M. Fahy, B. Wowk, J. Wu, J. Phan, C. Rasch, A. Chang, E. Zendejas, Cryopreservation of organs by vitrification: perspectives and recent advances, Cryobiology. 48 (2004) 157–178.

[30] J.S.G. Feig, D.P. Eisenberg, Y. Rabin, Polarized light scanning cryomacroscopy, part I: Experimental apparatus and observations of vitrification, crystallization, and photoelasticity effects, Cryobiology. 73 (2016) 261–271.

[31] J.S.G. Feig, Y. Rabin, The scanning cryomacroscope – A device prototype for the study of cryopreservation, Cryogenics. 62 (2014) 118–128.

[32] J.S.G. Feig, P.K. Solanki, D.P. Eisenberg, Y. Rabin, Polarized Light in Scanning Cryomacroscopy, Part II: Thermal Modeling and Analysis of Experimental Observations, Cryobiology. 73 (2016) 272–281.

[33] W.E. Forsythe, Table 281. Density of the Elements, Liquid or Solid, in: Smithson. Phys. Tables 9th Revis. Ed., Smithsonian Institution, Washington, D.C., 1954: p. 291.

[34] S. Fukusako, Thermophysical properties of ice, snow, and sea ice, Int. J. Thermophys. 11 (1990) 353–372.

[35] G.T. Furukawa, M.L. Reilly, J.S. Gallagher, Critical Analysis of Heat—Capacity Data and Evaluation of Thermodynamic Properties of Ruthenium, Rhodium, Palladium, Iridium, and Platinum from 0 to 300K. A Survey of the Literature Data on Osmium., J. Phys. Chem. Ref. Data. 3 (1974) 163–209.

[36] U. Gaur, B. Wunderlich, Heat Capacity and Other Thermodynamic Properties of Linear Macromolecules. V. Polystyrene, J. Phys. Chem. Ref. Data. 11 (1982) 313–325.

[37] U. Hammerschmidt, W. Sabuga, Transient Hot Wire (THW) Method: Uncertainty Assessment, Int. J. Thermophys. 21 (2000) 1255–1278.

[38] U. Hartmann, B. Nunner, C. Körber, G. Rau, Where should the cooling rate be determined in an extended freezing sample?, Cryobiology. 28 (1991) 115–130.

[39] J.J. Healy, J.J. de Groot, J. Kestin, The theory of the transient hot-wire method for measuring thermal conductivity, Phys. BC. 82 (1976) 392–408.

[40] J.M. Hey, D.R. MacFarlane, Crystallization of Ice in Aqueous Solutions of Glycerol and Dimethyl Sulfoxide. 1. A Comparison of Mechanisms, Cryobiology. 33 (1996) 205–216.

[41] J. Holman, Heat Transfer, 10 edition, McGraw-Hill Education, Boston, 2009.

[42] J.P. Holman, Heat Transfer, ninth, McGraw Hill, New York, 2002.

[43] K.R. Holmes, W. Ryan, M.M. Chen, Thermal conductivity and H2O content in rabbit kidney cortex and medulla, J. Therm. Biol. 8 (1983) 311–313.

[44] J.B. Hopkins, R. Badeau, M. Warkentin, R.E. Thorne, Effect of Common Cryoprotectants on Critical Warming Rates and Ice Formation in Aqueous Solutions, Cryobiology. 65 (2012) 169–178.

[45] F.P. Incropera, D.P. DeWitt, T.L. Bergman, A.S. Lavine, Transient Conduction, in: Fundam. Heat Mass Transf., 6th edition, John Wiley & Sons, Hoboken, NJ, 2006.

[46] J.L. Jimenez Rios, Y. Rabin, Thermal expansion of blood vessels in low cryogenic temperatures Part I: A new experimental device, Cryobiology. 52 (2006) 269–283.

[47] W.N. Kim, C.M. Burn, Thermal behavior, morphology, and some melt properties of blends of polycarbonate with poly(styrene-co-acrylonitrile) and poly(acrylonitrile-butadiene-styrene), Polym. Eng. Sci. 28 (1988) 1115–1125.

[48] R.P. Lanza, H.Y. Chung, J.J. Yoo, P.J. Wettstein, C. Blackwell, N. Borson, E. Hofmeister, G. Schuch, S. Soker, C.T. Moraes, M.D. West, A. Atala, Generation of histocompatible tissues using nuclear transplantation, Nat. Biotechnol. 20 (2002) 689–696.

[49] J.K. Lewis, J.C. Bischof, I. Braslavsky, K.G.M. Brockbank, G.M. Fahy, B.J. Fuller, Y. Rabin, A. Tocchio, E.J. Woods, B.G. Wowk, J.P. Acker, S. Giwa, The Grand Challenges of Organ Banking: Proceedings from the first global summit on complex tissue cryopreservation, Cryobiology. 72 (2016) 169–182.

[50] W.S. MacGregor, The Chemical and Physical Properties of Dmso, Ann. N. Y. Acad. Sci. 141 (1967) 3–12.

[51] P. Mazur, Principles of Cryobiology, in: Life Frozen State, CRC Press, New York, 2004: pp. 3–65.

[52] Y. Nagasaka, A. Nagashima, Absolute measurement of the thermal conductivity of electrically conducting liquids by the transient hot-wire method, J. Phys. [E]. 14 (1981) 1435.

[53] D.A. Noday, P.S. Steif, Y. Rabin, Viscosity of cryoprotective agents near glass transition: a new device, technique, and data on DMSO, DP6, and VS55, Exp. Mech. 49 (2009) 663–672.

[54] T.A. Osswald, J.P. Hernández-Ortiz, Processing Properties, in: Polym. Process., Hanser, 2006: pp. 37–110.

[55] W. Patnode, W.J. Scheiber, The Density, Thermal Expansion, Vapor Pressure, and Refractive Index of Styrene, and the Density and Thermal Expansion of Polystyrene, J. Am. Chem. Soc. 61 (1939) 3449–3451.

[56] J. Plitz, Y. Rabin, J.R. Walsh, The Effect of Thermal Expansion of Ingredients on the Cocktails VS55 and DP6, Cell Preserv. Technol. 2 (2004) 215–226.

[57] Y. Rabin, The effect of temperature-dependent thermal conductivity in heat transfer simulations of frozen biomaterials, Cryo Letters. 21 (2000) 163–170.

[58] Y. Rabin, J. Plitz, Thermal expansion of blood vessels and muscle specimens permeated with DMSO, DP6, and VS55 at cryogenic temperatures, Ann. Biomed. Eng. 33 (2005) 1213–1228.

[59] Y. Rabin, M.J. Taylor, J.S.G. Feig, S. Baicu, Z. Chen, A new cryomacroscope device (Type III) for visualization of physical events in cryopreservation with applications to vitrification and synthetic ice modulators, Cryobiology. 67 (2013) 264–273.

[60] Y. Rabin, M.J. Taylor, J.R. Walsh, S. Baicu, P.S. Steif, Cryomacroscopy of vitrification, Part I: A prototype and experimental observations on the cocktails VS55 and DP6, Cell Preserv. Technol. 3 (2005) 169–183.

[61] D.H. Rasmussen, A.P. Mackenzie, Phase Diagram for the System Water–Dimethylsulphoxide, Nature. 220 (1968) 1315–1317.

[62] J.L.J. Rios, Y. Rabin, Thermal expansion of blood vessels in low cryogenic temperatures, Part II: Vitrification with VS55, DP6, and 7.05 M DMSO, Cryobiology. 52 (2006) 284–294.

[63] B. Rubinsky, E.G. Cravalho, An analytical method to evaluate cooling rates during cryopreservation protocols for organs, Cryobiology. 21 (1984) 303–320.

[64] K. Sack, Transplant Experts Blame Allocation System for Discarding Kidneys, N. Y. Times. (2012).

[65] S. Sakazume, N. Seki, Bull JSME. 44 (1978) 2059.

[66] J. Scandling, 5. Transplantation tolerance, Cryobiology. 71 (2015) 166.

[67] G.A. Slack, Platinum as a Thermal Conductivity Standard, J. Appl. Phys. 35 (1964) 339–344.

[68] P.S. Steif, M. Palastro, C. Wan, S. Baicu, M.J. Taylor, Y. Rabin, Cryomacroscopy of vitrification, Part II: Experimental observations and analysis of fracture formation in vitrified VS55 and DP6, Cell Preserv. Technol. 3 (2005) 184–200.

[69] P.S. Steif, M.C. Palastro, Y. Rabin, The Effect of Temperature Gradients on Stress Development during Cryopreservation via Vitrification, Cell Preserv. Technol. 5 (2007) 104–115.

[70] M.J. Taylor, S. Baicu, Review of vitreous islet cryopreservation, Organogenesis. 5 (2009) 155–166.

[71] M.J. Taylor, L.H. Campbell, R.N. Rutledge, K.G.M. Brockbank, Comparison of Unisol with Euro-Collins solution as a vehicle solution for cryoprotectants, Transplant. Proc. 33 (2001) 677–679.

[72] M.J. Taylor, Y.C. Song, K.G.M. Brockbank, Vitrification in Tissue Preservation: New Developments, in: Life Frozen State, CRC Press, New York, 2004: pp. 603–641.

[73] E. Totsuka, J.J. Fung, M.-C. Lee, T. Ishii, M. Umehara, Y. Makino, T.-H. Chang, Y. Toyoki, S. Narumi, K. Hakamada, M. Sasaki, Influence of Cold Ischemia Time and Graft Transport Distance on Postoperative Outcome in Human Liver Transplantation, Surg. Today. 32 (2002) 792–799.

[74] W.M. Underwood, J.R. Taylor, The thermal conductivity of several plastics determined by an improved line-source apparatus, Polym. Eng. Sci. 18 (1978) 556–563.

[75] J.W. Valvano, J.R. Cochran, K.R. Diller, Thermal conductivity and diffusivity of biomaterials measured with self-heated thermistors, Int. J. Thermophys. 6 (1985) 301–311.

[76] J. Wang, J.K. Carson, M.F. North, D.J. Cleland, A new approach to modelling the effective thermal conductivity of heterogeneous materials, Int. J. Heat Mass Transf. 49 (2006) 3075–3083.

[77] B. Wowk, Ice nucleation and growth in concentrated vitrification solutions, Cryobiology. 55 (2007) 330.

[78] B. Wowk, Thermodynamic aspects of vitrification, Cryobiology. 60 (2010) 11–22.

[79] B. Wowk, G.M. Fahy, Toward large organ vitrification: extremely low critical cooling and warming rates of M22 vitrification solution, Cryobiology. 51 (2005) 362.

[80] B. Wowk, E. Leitl, C.M. Rasch, N. Mesbah-Karimi, S.B. Harris, G.M. Fahy, Vitrification enhancement by synthetic ice blocking agents, Cryobiology. 40 (2000) 228–236.

[81] H. Yinnon, D.R. Uhlmann, A kinetic treatment of glass formation V: Surface and bulk heterogeneous nucleation, J. Non-Cryst. Solids. 44 (1981) 37–55.

[82] A. Zhang, S. Cheng, L. He, D. Luo, D. Gao, Determination of Thermal Conductivity of Cryoprotectant Solutions and Cell Suspensions, Cell Preserv. Technol. 2 (2004) 157–162.

[83] X. Zhang, W. Hendro, M. Fujii, T. Tomimura, N. Imaishi, Measurements of the Thermal Conductivity and Thermal Diffusivity of Polymer Melts with the Short-Hot-Wire Method, Int. J. Thermophys. 23 (2002) 1077–1090.

[84] 9.2 Thermal Properties of Foods, in: 2006 ASHRAE Handb. - Refrig. -P Ed., American Society of Heating, Refrigerating and Air-Conditioning Engineers, Inc., 2006.

[85] Critical cooling rates to avoid ice crystallization in solutions of cryoprotective agents - Journal of the Chemical Society, Faraday Transactions (RSC Publishing) DOI:10.1039/FT9918700101, (n.d.).

[86] Heart, Aorta and Kidney CAD Model | NIH 3D Print Exchange, (n.d.).